MASTERARBEIT | MASTER'S THESIS

Titel | Title

Modelling of light pollution via night sky photometry

verfasst von | submitted by

Linda Costantini BSc

angestrebter akademischer Grad | in partial fulfilment of the requirements for the degree of

Master of Science (MSc)

Wien | Vienna, 2026

Studienkennzahl lt. Studienblatt | Degree programme code as it appears on the student record sheet:	UA 066 861
Studienrichtung lt. Studienblatt | Degree programme as it appears on the student record sheet:	Masterstudium Astronomy
Betreut von | Supervisor:	Dr. Stefan Wallner BSc MSc

Acknowledgements

I'm extremely grateful to my supervisor, Stefan Wallner, for his invaluable patience and feedback in this endeavor. This would not have been possible without his support.

Next, I would like to thank Raphael Selber, my best friend and boyfriend, who encouraged me throughout my studies, kept me motivated and was always there to support me. Without his unwavering presence by my side, I would not be where I am today.

I would also like to express my appreciation for my friends, who accompanied me throughout my studies, providing valuable insights, support and feedback. They enriched my life greatly. I would especially like to thank Olivier Baddé, Fabian Haberhauer, Carina Heinreichsberger, Michael Janosik, Lukas Kuess, Anna Schrenk, Johannes Seelig and Arijane Sommeregger.

I also want to thank the professors, guest lecturers and tutors I had the pleasure to learn from over the years, for sharing their knowledge and inspiring me to get to this point in my studies.

Sincere thanks also goes to Michaela Deventer-Compes, who supported me throughout the more difficult times over the years. Without her, the completion of this thesis would not have been possible.

Finally, special thanks goes to my cat, Kamui. While he did not help me in writing this thesis, rather hindered me on several occasions, he provided invaluable emotional support and love, without which I could not have completed this thesis. I am forever grateful for having him in my life.

Abstract

Modelling light pollution is highly complex, partly due to the complexity of the City Emission Function (CEF), one of its fundamental components.
Over the years, existing models of the CEF have been improved to advance studies in this area. Still, there is no final definition of this concept.
To further advance these studies, this thesis focuses on simplifying the concept and obtaining CEFs with minimal ground-based measurements.
Data was obtained at nine locations in Vienna using an SQM and from a stationary SQM, during the same night. Additionally, data was used from four stationary TESS-W photometers located in Eisenstadt over several nights.
The data was interpolated using Python's griddata function and cubic method.
The resulting CEFs show, that accurate depictions of a cities Night Sky Brightness can be obtained even with few data points, if they are evenly spread across a city and provide decent coverage. Moreover, the results show the complexity of the CEF that stem from constant changes over space, time and through different seasons.
This highlights the need to obtain more CEFs and build databases to improve the understanding of this concept and advance studies in this field. To achieve that, this thesis provides a simple and fast way of retrieving CEFs using either minimal measurements or publicly available data, making it ideal for amateur and professional astronomers alike.

Kurzfassung

Die Modellierung von Lichtverschmutzung ist äußerst komplex, was zum Teil auf die Komplexität der City Emission Function (CEF) zurückzuführen ist, eine ihrer grundlegenden Komponenten. Im Laufe der Jahre wurden die bestehenden Modelle der CEF verbessert, um die Forschung in diesem Bereich voranzutreiben. Dennoch gibt es noch keine endgültige Definition dieses Konzepts.

Um diese Forschungen weiter voranzutreiben, konzentriert sich diese Arbeit darauf, das Konzept zu vereinfachen und CEFs mit minimalen bodengestützten Messungen zu erhalten.

Die Daten wurden von neun Standorten in Wien mit einem SQM und von einem stationären SQM während derselben Nacht erhoben. Zusätzlich wurden Daten von vier stationären TESS-W Photometern in Eisenstadt über mehrere Nächte hinweg verwendet. Die Daten wurden mit der Griddata-Funktion von Python und der kubischen Methode interpoliert.

Die resultierenden CEFs zeigen, dass genaue Darstellungen der Nachthimmelshelligkeit einer Stadt auch mit wenigen Datenpunkten erzielt werden können, wenn diese gleichmäßig über eine Stadt verteilt sind und eine angemessene Abdeckung bieten. Darüber hinaus zeigen die Ergebnisse die Komplexität der CEF, die sich aus ständigen Veränderungen über Raum, Zeit und verschiedene Jahreszeiten hinweg ergibt.

Dies hebt die Notwendigkeit hervor, mehr CEFs zu erfassen und Datenbanken aufzubauen, um das Verständnis dieses Konzept zu verbessern und die Forschung auf diesem Gebiet voranzutreiben. Um dies zu erreichen, bietet diese Arbeit eine einfache und schnelle Methode zur Ermittlung von CEFs entweder anhand minimaler Messungen oder öffentlich zugänglicher Daten, wodurch sie sich ideal für Amateur- und professionelle Astronomen gleichermaßen eignet.

Contents

List of Tables

List of Figures

Listings

1. Introduction

1.1. Light Pollution

Light pollution refers to the excessive use and misdirection of Artificial Light At Night (ALAN), which obscures the natural dark sky. It stems from various sources, including glare, skyglow and light trespass. The consequences for astronomical observations, such as reduced visibility of celestial bodies, are widely recognized, its ecological and health-related impacts are deserving of equal attention.
Raising global awareness about the severity of light pollution is essential to insure public understanding but also promote the development of policies and regulations aimed at mitigating its effects. The following sections explore the impacts of light pollution on wildlife, plants and ecosystems, continuing with human health, energy and waste and lastly astronomical observations.

1.1.1. Impacts on Wildlife, Plants and Ecosystems

Longcore and Rich (2004) distinguish between *astronomical* and *ecological* light pollution. While the former refers to the obscuring of the natural night sky, which is what light pollution is most commonly known for, the latter refers to artificial light that changes the cycles of light and dark in ecosystems. Ecological light pollution includes direct glare, increased illumination and unexpected fluctuations in lighting. Common sources mentioned by Longcore and Rich (2004) include skyglow, streetlamps, illuminated buildings, vehicles, boats and oil platforms.
Fig. 1.1 shows why distinguishing between these two forms of light pollution is important, especially when it comes to strategies of mitigating light pollution. One strategy that is often talked about and more commonly implemented than others, is the proper shielding of streetlamps to avoid light being directed into the night sky as well as avoid unnecessary scattering. While this may reduce *astronomical* light pollution, the light from streetlamps still causes *ecological* light pollution as wildlife and plants are still affected.

Excessive light can disrupt many behaviors of animals, such as foraging, reproduction, migration and communication. Sea turtles that lay eggs on shore may choose suboptimal nesting sites due to excessive light and human disturbance. This can reduce overall hatchling numbers and survivability (Witherington and Martin, 2003).
Furthermore, many animals rely on natural light for navigation. Artificial light sources can lead to disorientation, attracting or repelling animals. For example, Witherington and Martin (2003) cite several studies showing sea turtles use visual cues to find the

Figure 1.1.: Diagram showing the difference and importance of distinguishing between astronomical and ecological light pollution. From (Longcore and Rich, 2004). Reprint with permission.

sea, typically moving toward the brightest horizon. Artificial lighting from streetlamps and urban areas can mislead hatchlings and adults alike, increasing their vulnerability to predators by prolonging the time they need to return to the ocean. This risk is especially pronounced around midnight, when hatchling emergence peaks, making them highly susceptible to disorientation caused by artificial light.

Light pollution also disrupts circadian rhythms and the natural sleep-wake cycles (Raap et al., 2015), impacting growth and breeding habits (Russart and Nelson, 2018). Emmer et al. (2018) and Melika et al. (2025) furthermore discuss effects such as melatonin suppression, altered metabolism, immune system dysfunction, increased cancer risk and changes in foraging and reproductive behavior.
Plants are also indirectly affected. Melika et al. (2025) highlight how nocturnal pollinators such as moths, bats and beetles are disturbed by artificial light, which in turn affects plant reproduction and broader ecosystem dynamics.

1.1.2. Impacts on Human Health

In addition to ecological impacts, ALAN has been increasingly recognized as a significant factor affecting human health. It disrupts circadian rhythms and suppresses melatonin production, leading to poor sleep quality and reduced overall sleep, fatigue, stress and heightened anxiety. Especially stress is a factor that contributes to the development of more serious chronic conditions such as depression, obesity and many others (Hassan, 2024).
Jiménez et al. (2025) reviewed 32 studies investigating the relationship between excessive ALAN exposure and various chronic diseases. Their review consistently found associations between ALAN and metabolic disorders, hypertension, type 2 diabetes, and mental

health disorders. These findings suggest that chronodisruption[1] plays a central role in the deterioration of both metabolic and psychological health.
Similarly, Wojciechowska et al. (2025) highlighted several studies that provide further evidence linking ALAN exposure to an increased risk of cardiovascular diseases, including hypertension, obesity, diabetes and atherosclerosis. Yang et al. (2025) further identify associations between ALAN exposure and poorer control of low-density lipoprotein cholesterol (LDL-C), a main factor in cerebrovascular and metabolic diseases.
In the context of neuro-degenerative diseases, particularly dementia, ALAN has been found to exacerbate psychiatric symptoms. Tondelli et al. (2025) report strong associations with delusions, hallucinations and sleep disturbances, even after adjusting for age, sex, cognitive status, disease duration and dementia subtype. However, their study was limited by a small sample size and they focus on only outdoor ALAN, neglecting indoor lighting and environmental factors altogether. Since Tondelli et al. (2025) report striking initial findings beside these shortcomings, further research is warranted.
Beyond chronic conditions, light pollution has also been linked to increased cancer risks, particularly prostate and breast cancer (Kloog et al., 2009), (Hansen and Lassen, 2012), (Kamdar et al., 2013), (Hurley et al., 2014), (Pukkala et al., 2006), (Schernhammer et al., 2006). Constant exposure to glare and blue light can also lead to eye strain (Park, 2018), headaches and long-term impacts on vision.

These findings underline the urgent need to study and mitigate light pollution to increase overall public health.

1.1.3. Impacts on Energy and Waste

Outdoor lighting is vital to modern infrastructure, ensuring safety and visibility, though, when poorly or inefficiently implemented, it becomes a major contributor to energy waste.

According to Dark Sky International (DarkSky), outdoor lighting in the United States uses around 120 terawatt-hours of energy annually. It is estimated that at least 30% of this energy is wasted, primarily due to unshielded light fixtures. This inefficiency costs billions each year, while also resulting in the release of around 21 million tons of CO_2, thereby contributing directly to greenhouse gas emissions and climate change (DarkSky International, 2023a), (DarkSky International, 2021).
A case study by Manteigas et al. (2012) in Vialonga, Portugal reinforces the concerns raised by DarkSky. The study found that lighting fixtures exceed the recommended illuminance values set by European standards (EN 13201), with approximately 40% of luminance being wasted. This waste was attributed to excessive mounting heights, improper spacing of fixtures and lack of shielding. Such inefficiencies increase energy consumption as well as intensify light pollution (Hänel et al., 2016).
Reports by the European Commission (Commission, a), (Commission, b) and DarkSky

[1]Chronodisruption refers to the disturbance or alteration of the body's natural biological rhythms.

International (2021) emphasize that excess light contributes to climate change and environmental degradation.
To address these issues, both DarkSky International (2023a) and Manteigas et al. (2012) advocate for environmentally responsible lighting practices, such as installing fully shielded fixtures, using warm-white LEDs, dimmers, motion sensors, timers and turning off unnecessary indoor lighting.
DarkSky International (2023a) suggests that such measures could significantly reduce energy consumption and carbon emissions.

1.1.4. Impacts on Astronomy

In addition to light pollutions impact on human health, wildlife behavior and energy consumption, it impacts the ability of both professional and amateur astronomers in conducting observations. The increasing prevalence of artificial light sources in urban and suburban environments has led to a measurable degradation of the quality of the night sky, reducing the visibility of celestial objects significantly.

Ground-based telescopes rely on large apertures and long exposure times to collect photons from faint astronomical objects. These photons are recorded by sensitive detectors, such as Charge-Coupled Devices (CCDs) or Complementary Metal-Oxide-Semiconductor (CMOS) sensors, which convert light into electronic signals for image processing.
Unfortunately, these detectors also capture unwanted light from artificial sources. This additional light increases the background brightness of the sky, reducing the contrast between celestial objects and their surroundings, leading to overexposed images and a loss of scientific data.

Perez (2023) reports that approximately two-thirds of professional observatories experience sky brightness levels exceeding International Astronomical Union (IAU) recommended threshold. Even observatories in remote regions are increasingly affected by urban light. A longitudinal study conducted in Rzeszow, Poland illustrates this trend. The study aimed to discuss the influence that light pollution has on the natural night sky and emphasized the impact on astronomical observations for both professional and amateur astronomers.
The study showed a significant deterioration in sky brightness between 2015 and 2021. In 2015, 19.20–18.67 mag/arcsec^2 were measured using a Sky Quality Meter (SQM) compared to 17.13–15.11 mag/arcsec^2 measured in 2021. Neighboring towns also experienced a significant decline in night sky quality. Wesołowski (2023) predicted that by 2025 the visibility would further decrease, expecting measurements of $\sim$14.05 mag/arcsec^2 in Rzeszow and $\sim$17.30 mag/arcsec^2 in neighboring towns. These predictions, including upper and lower value bounds of the confidence level of 95% are included in Fig. 1.2. Through this deterioration of the natural dark sky many stars and deep-sky objects become invisible to the naked-eye and small telescopes.
Faint celestial objects, such as comets, are among the first that become undetectable

under light polluted skies, even during periods of increased activity (Wesołowski, 2019), (Wesołowski, 2023).

Recent studies suggest that the global sky brightness is increasing at an average rate of 9.6% per year (Kyba et al., 2023). If current trends continue, even suburban cities may reach critically high sky brightness levels, further threatening astronomical research by both professional and amateur astronomers.

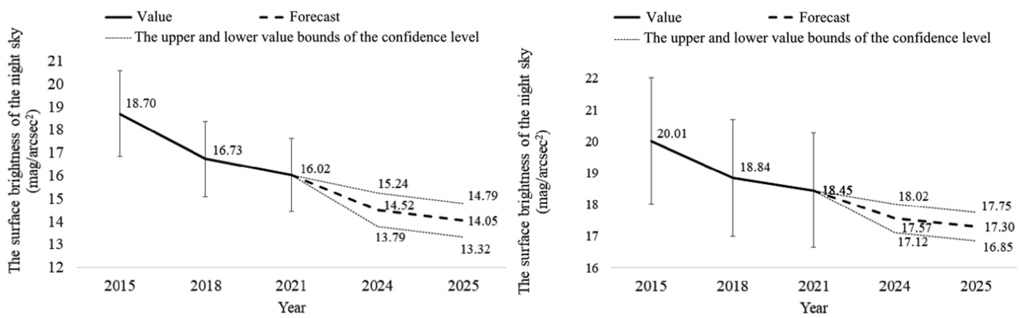

(a) Prediction for Rzeszow. (b) Prediction for Biala.

Figure 1.2.: Predicted surface brightness of the night sky for the year 2025, based on measurements from 2015, 2018 and 2021. From (Wesołowski, 2023). Reprint with permission.
license by: `https://creativecommons.org/licenses/by/4.0/`

Some proposed solutions are already being implemented in parts of Austria and several municipalities are pursuing certification as Dark Sky Communities to preserve the natural night sky. In Austria, the Attersee-Traunsee Nature Park has already achieved recognition as a Dark Sky Place, meeting all criteria established by DarkSky International (2023b). Despite these efforts, urbanization continues to expand and urban areas remain the primary contributors to light pollution due to the high density of lighting sources. Raising public awareness and implementing even stricter lighting policies in all states is therefore essential.

1.2. The Complexity of Light Pollution

As urbanization spreads and lighting technologies advance, the intensity and spatial reach of ALAN have increased dramatically. High population densities, infrastructure, development of residential areas and many more contribute to the increase of artificial light sources and therefore light pollution.
Overall, satellite observations as well as ground-based measurements over the years show a consistent global increase in sky brightness (Kyba et al., 2023). Light pollution extends far beyond city centers and even city borders, creating diffuse halos that obscure the natural night sky even in remote areas. This is amplified by the transition from High

Pressure Sodium (HPS) lamps to LEDs. While LEDs are more energy efficient, they emit a portion of their light in the 400-500nm range, blue light. These emissions have stronger effects on animals and are scattered strongly by the atmosphere. Additionally, most satellites and photometers are not sensitive in that spectral range, resulting in the illusion of a darker night sky (Linares Arroyo et al., 2024).

With the growing complexity of light pollution comes the need for modelling and predicting its further development. A main factor in doing so is the City Emission Function (CEF). It describes the spatial and spectral distribution of light emitted from urban areas and is influenced by a wide range of variables. These include, to name a few, population density, lighting fixtures, architecture and topography (Kocifaj and Solano Lamphar, 2016). Furthermore, Aerosol Optical Depth (AOD) significantly affects scattering and absorption of light in the atmosphere and therefore the NSB and CEF.

Defining such a function is challenging, as it is not a fixed quantity. It constantly changes, over time as well as over space. Different modelling approaches attempt to approximate it using satellite data, ground-based measurements and a variety of parameters. Still, due to its variability and the high dependence on local conditions, there is no universal or final definition (Kocifaj, 2018), (Kocifaj, 2017).
Despite these challenges, the CEF is important for understanding, modelling and predicting the spread of light pollution, which is why there is a need for further studies and why it is the main focus of this thesis. It will be discussed in more detail in the next chapter, giving an overview over existing models, limitations and improvements over the past years.
Additionally, different modelling and measurement tools will be discussed and compared to show the availability and accessibility for light pollution studies and establishing use cases, thereby determining an appropriate way to obtain and analyze data for the purpose of this thesis and potential further studies.

2. Modelling and Measuring Light Pollution

To better understand the importance of the CEF in light pollution studies, this Section discusses the concept, existing models, limitations and improvements of the CEF over the years.
After this discussion, several modelling and measurement tools for light pollution are discussed. Different available and widely used tools are compared to establish their use cases, limitations and advantages, to illustrate the choices that were made for this thesis and to provide an overview of available tools for further studies.

2.1. The City Emission Function (CEF)

As previously discussed, light pollution from urban environments has serious effects on the visibility of the night sky, on ecosystems and on human health. The concept of the CEF is crucial to the study of light pollution, modelling skyglow and to understanding and reducing these effects. It describes the angular distribution of light emissions, typically from cities. The CEF is usually expressed as a function of the zenith angle and includes both direct upward emissions from various ground-based light sources, as well as diffuse reflections from surfaces such as roads, buildings, and vegetation (Li et al., 2025).
Field experiments have demonstrated that the CEF can be retrieved from ground-based night sky radiometry, offering a practical method for characterizing urban light emissions globally. This approach enables systematic monitoring of CEFs across cities and provides critical data for modelling skyglow (Kocifaj et al., 2019).

2.1.1. Limitations of Empirical Models

The Garstang Emission Function (GEF) has been widely used to model the CEF despite its shortcomings.
The GEF implements ground reflectance (G) and uplight fraction (F) in a simplified manner, not taking the complexity of light at different distances and angles, as well as urban environments, blocking and topography, into account.
It overestimates emissions near the horizon, leading to unrealistic predictions of skyglow from distant sources, as demonstrated by Kocifaj and Solano Lamphar (2016). The radiance of a finite-sized flat surface must approach zero at low elevation angles, which is a requirement the GEF does not satisfy. Therefore the GEF is not a suitable tool for

modelling skyglow from distant sources.

Furthermore, empirical models usually do not account for spectral variations in urban lighting, such as emissions from HPS lamps or the increasing presence of LED lighting. These spectral differences significantly affect scattering behavior and skyglow intensity (Solano Lamphar, 2018).
These shortcomings are the reason more accurate and flexible models were developed.

2.1.2. Improved Analytical Models

Kocifaj and Solano Lamphar (2016) proposed two improved formulations of the CEF. One is a modified version of the GEF with exponential correction, through introducing an additional exponential factor, that reduces horizon emissions and ensures energy conservation across the hemisphere. The other is an inverse cosine-based function, which allows for analytical normalization and offers greater flexibility and computational efficiency. Both models satisfy essential physical requirements and are suitable for standard and inverse radiative transfer problems.
These models also enable the analysis of how different wavelengths contribute to skyglow. This is particularly relevant for cities undergoing LED conversions, where blue light emissions are more prominent and have greater ecological and astronomical impacts (Luginbuhl et al., 2014), (Kinzey et al., 2017).
Another improvement is the inversion method developed by Kocifaj (2017), which enables retrieval of CEFs from night sky radiance measurements taken along a local meridian. This approach is particularly effective when observations are made at intermediate distances from the city, ensuring high information content and minimizing angular distortion.

The Comprehensive City Emission Function (CCEF)

Building on these improvements, Kocifaj (2018) then introduced a more robust analytical framework. The Comprehensive City Emission Function (CCEF) is designed to simulate heterogeneous urban environments, where light sources and obstacles are randomly distributed. Unlike purely empirical models, the CCEF uses closed-form analytical equations for fast computation. It introduces probability functions to estimate the likelihood that light escapes the urban environment without being blocked, and includes zenith normalized and total lumen output normalized versions for cross city comparisons. The CCEF incorporates:

- Statistical distributions of building sizes, heights, and separations
- Light fixture properties (height, density, emission patterns)
- Ground reflectance and uplight fraction
- Blocking effects from buildings and urban structures

- City size and shape

Garstang's model lacks dependence on important urban parameters and assumes a Lambertian distribution that contradicts real world observations. It also ignores direct horizontal emissions from buildings, which the CCEF explicitly includes, therefore significantly improving upon Garstang's GEF.

2.1.3. Radiative Transfer Modelling

The distinction between radiant intensity and radiance in regards to the CEF is crucial, when using it in boundary conditions. Radiance should be used in boundary conditions for the Radiative Transfer Equation (RTE), yet the CEF is usually expressed in terms of radiant intensity. This could lead to systematic errors in luminance predictions, cosine distortion and errors up to 10-1000× in luminance (Kocifaj and Solano Lamphar, 2016). Numerical experiments using the SkyGlow simulator show that such errors affect the amplitude of luminance, not its spatial pattern. This makes it difficult to detect them without accurate light output data.
Atmospheric aerosols significantly contribute to the observed skyglow. Parameters such as AOD, Single Scattering Albedo (SSA), and Asymmetry Parameter (ASY) must be considered when modeling the CEF, as they influence both forward and backward scattering of light (Kocifaj and Solano Lamphar, 2016).

2.1.4. Conclusion

The CEF is a foundational concept for understanding and modelling light pollution. Its accurate representation is essential for predicting skyglow, interpreting satellite imagery, and guiding responsible urban planning and lighting design. It is also important for astronomical site selection, environmental monitoring, remote sensing and radiative transfer modelling. While traditional models like Garstang's provided a foundation for skyglow modelling, they fall short in accurately representing urban light emissions, especially near the horizon and for more complex models.
Advancements such as physically consistent analytical formulations and the CCEF, provide more realistic, scalable, and computationally efficient alternatives to previous models. These recent models integrate urban geometry, fixture properties and blocking effects resulting in more precise simulations.
The retrieval of CEFs from night sky radiance data represents a major advancement in light pollution research. It enables the creation of a global database of CEFs (Kocifaj, 2017), which can be used to improve predictive models, guide lighting policy, and assess environmental impacts with greater accuracy.
Future studies should focus on integrating topographic effects, validating models with observational data, and refining parameters to better capture the anisotropic nature of urban light emissions and further improve the concept of the CEF. Improvements to the CEF modelling should also include dynamic aerosol profiles and pollution data, as these

significantly affect the propagation of light in urban atmospheres (Wallner and Kocifaj, 2023).
The improved CEF and CCEF frameworks are vital for astronomical site protection and environmental impact assessments, as well as for advancing urban planning, satellite data calibration, and the development of sustainable lighting policies. Considering the importance of the CEF in light pollution studies, there should be appropriate focus on this concept in current and future research.
Due to the dynamic nature and dependence on numerous local factors of the CEF, accurately characterizing and predicting light pollution requires robust modelling tools and precise measurement instruments. In the following sections, several tools and instruments are presented.

2.2. SkyGlow Simulator or formerly MSNsRAu

The SkyGlow Simulator is a numerical model that is computationally efficient in simulating light pollution. It was developed by Kocifaj (2007) and focuses on single scattering in an optically thin atmosphere, under clear or overcast sky and low turbidity conditions.
Since it does not account for second order scattering or reflections from the ground, which are more significant in complex environments, it doesn't require as much computational power as other more complex models like ILLUMINA. SkyGlow is therefore best used for quick simulations, when computational resources are limited and for nearby light sources, where second order scattering is negligible. Hence, it is especially useful for localized studies, as it is mostly effective when studying light pollution from nearby towns and small cities. It is not suitable for distant light sources as it underestimates the contributions from faraway light sources (Linares Arroyo et al., 2018).
Due to the simulations barely taking minutes the model is easily adjustable, which makes it ideal for larger territories and mass modeling. Its efficiency for repeated simulations and the good agreement with ILLUMINA clearly show how advantageous it is to use this modelling tool.
On the other hand the limited accuracy near the horizon, due to the focus on single order scattering instead of second order scattering, the simplified aerosol scattering possibly missing backscattering effects and the suitability mainly for optically thin atmospheres and low turbidity instead of high-turbidity conditions and long optical paths, are some disadvantages of using the SkyGlow Simulator instead of other more complex simulators (Aubé and Kocifaj, 2012).

Fig. 2.1(a) shows the interface of the SkyGlow Simulator upon starting the program. The interface is relatively simple to navigate, using the toolbar at the top. It is possible to zoom in and out, toggle city names, grid and scale, and set different parameters before launching the simulation and viewing the results. Fig. 2.1(b) shows the interface zoomed in on Zilina, Slovakia with an observer outside the city ∼10-15 km away. When one or more cities are marked as shown in this figure, the city parameters can be set.

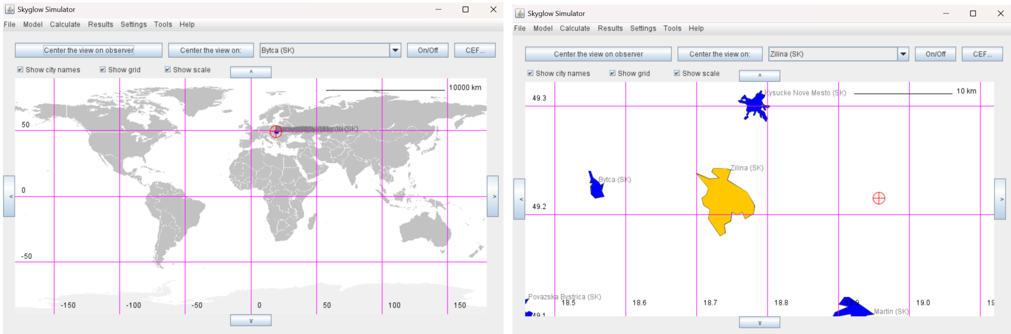

(a) Interface upon starting the program.

(b) Zoomed in on Zilina. The city was marked and an observer set outside.

Figure 2.1.: Interface of the SkyGlow Simulator.

The different options are shown in Fig. 2.2. Fig. 2.2(a) shows the emission settings. Here the total emission of the selected city can be set to Watts or Lumen, or based on the city population. The next tab in Fig. 2.2(b) gives the user the option of changing Garstang's GEF parameters, ground reflectance (G) and uplight fraction (F).
In the last tab in Fig. 2.2(c) and Fig. 2.2(d) different data files of typical spectra can be selected.

In addition to the city parameters, different parameters regarding the observer and sky can be set.
The observer can be placed anywhere on the map.
The different windows showing the settings concerning clouds, aerosols, blocking near the horizon and output characteristics are shown in Fig. 2.3.
Fig. 2.3(a) shows the possible settings regarding clouds. The simulation can be run for cloudless and cloudy conditions. The altitude of the cloud base can be specified and the spectral albedo can be selected from a set of data files.
In the latest version of the Simulator, Version 6.1., there is an option to also set the *cloud fraction*. Expanding the options for simulations from solely cloudless or overcast conditions to partly cloudy conditions as well. Additionally, a random seed generator was implemented to randomly generate the cloud positions and their sizes.
Fig. 2.3(b) shows the possible aerosol settings. The aerosol optical thickness and its spectral dependence, aerosol concentration and spectral dependence of the SSA and of the ASY can be set. For the spectral dependence of the SSA and ASY there is a prepared set of data files to choose from.
The next tab in Fig. 2.3(c) gives the option of defining the horizon and blocking objects. And the last tab in Fig. 2.3(d) gives the option of specifying the output. The options are between *visual*, for a calculation in cd/m^2, and *energetic*, for a calculation in W/m^2/sr and the option of selecting the wavelength range. The program calculates in intervals of 5 nm.

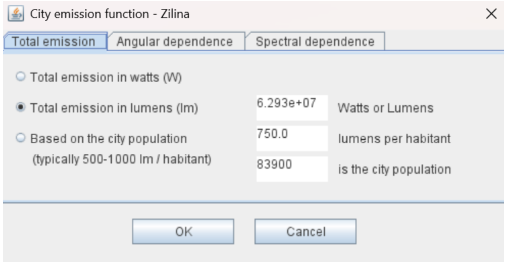

(a) Panel for setting total emission.

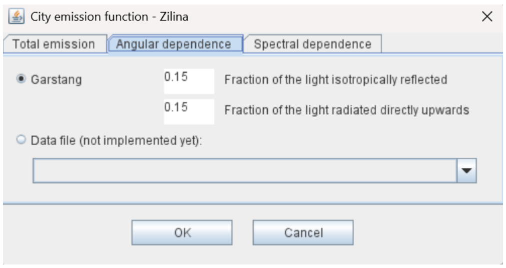

(b) Panel for setting angular dependence.

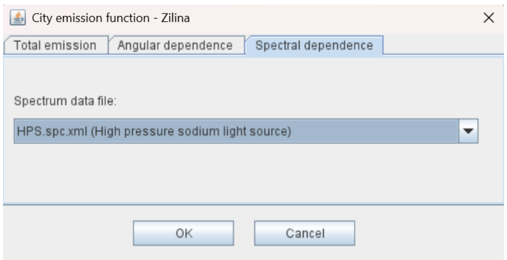

(c) Panel for setting spectral dependence.

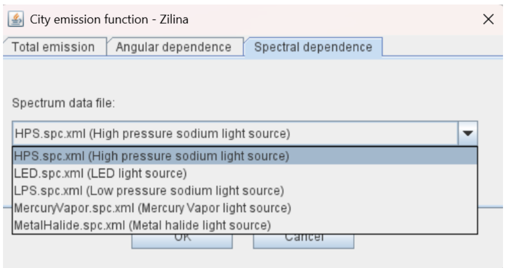

(d) Panel for setting spectral dependence showing the different options.

Figure 2.2.: Different interfaces showing the possible city parameters that can be set in the SkyGlow Simulator.

Once all desired parameters regarding the observer, city and sky are set, the simulation can be started. Once the simulation is done, the results can be viewed in Gnuplot. Fig. 2.4 shows how the output from SkyGlow Simulator can look. For these images, the observer was set outside Zilina, ~10-15 km away. Settings were left at the default. The only changes were made regarding the output. It was generated in cd/m^2 and then again in W/m^2/sr with a range from 350-800 nm.

When downloading the software[1] it comes with a manual, explaining in more detail the different possible settings and how to use the program. It also explains how more cities can be included, be split or enlarged temporarily and changes be made to the output plots.

2.3. ILLUMINA

ILLUMINA is a radiative transfer model that simulates light pollution by computing first and second order scattering, extinction due to aerosols and molecules and ray-tracing-like photon paths from luminaires to observers. Second order scattering is important for remote sites where it can contribute up to 66% of zenith radiance. Reflections from the

[1]available at: https://skyglow.sav.sk/ - last access: 05.11.2025 - 21:58

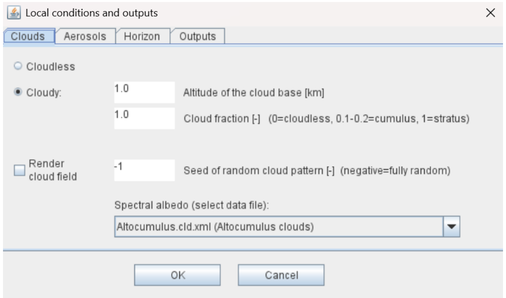

(a) Panel for cloud settings.

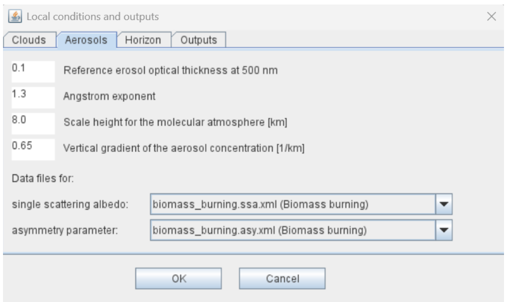

(b) Panel for aerosol settings.

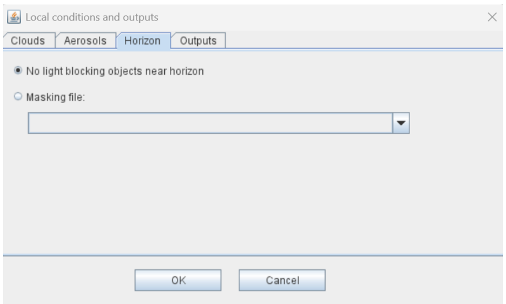

(c) Panel for horizon settings.

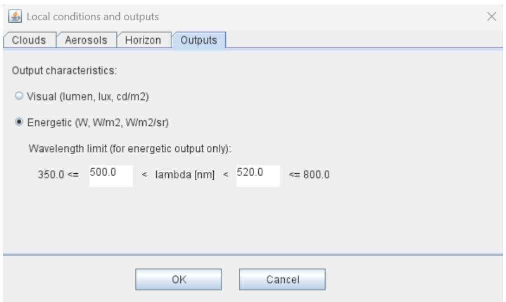

(d) Panel for output settings.

Figure 2.3.: Different interfaces showing the possible sky parameters that can be set in the SkyGlow Simulator.

ground are modeled as well and shadowing effects from terrain are also included.
Not only does the model account for geographical features and atmospheric conditions, but also light source characteristics like lamp spectra and angular distribution. Unlike SkyGlow, ILLUMINA has the need for high computational power with simulations taking significantly longer, up to several days. While it gives a detailed model of second order scattering and lamp distributions, it also requires much more input data, like lamp inventories, aerosol properties and terrain models to be able to account for them.
ILLUMINA provides two maps. One shows the contribution of each ground pixel to the sky radiance at specific viewing angles. The other indicates the sensitivity of sky radiance to changes in lighting installations per lumen installed. These maps make the tool especially valuable for astronomical site protection (Aubé and Kocifaj, 2012).

A disadvantage of using ILLUMINA is that it assumes spherical aerosol particles, which is not always accurate. Furthermore, while previously believed to be highly accurate under high turbidity conditions and for long optical paths, Kocifaj et al. (2024) found that ILLUMINA is mostly accurate in cases of low-turbidity and short distances. For ranges of less than 10 km and low AOD the model can yield accurate results, but ILLUMINA significantly overestimates the contribution of double-scattering for farther distances from the light source.

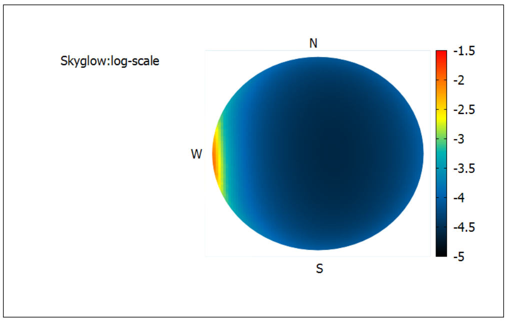

(a) Polar plot (god's view) for Zilina. Output in units of cd/m^2.

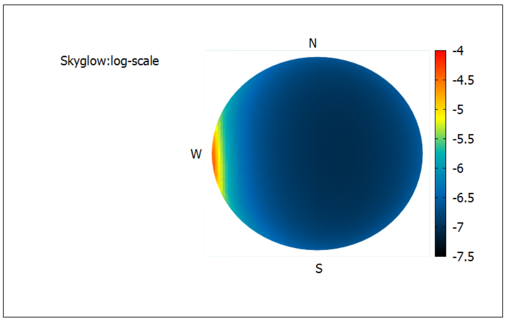

(b) Polar plot (god's view) for Zilina. Output was set to $W/m^2/sr$ with a range of 350-800 nm.

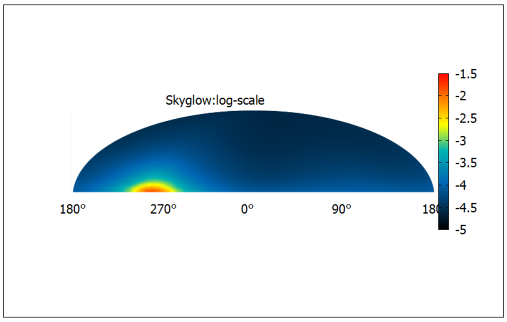

(c) Hammer plot (observer's view) for Zilina. Output in units of cd/m^2.

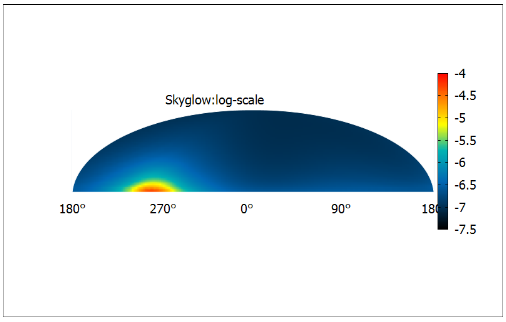

(d) Hammer plot (observer's view) for Zilina. Output was set to $W/m^2/sr$ with a range of 350-800 nm.

Figure 2.4.: Different possible outputs of the SkyGlow Simulator, showing the skyglow around Zilina from different perspectives.

It was found that higher order scattering is necessary to achieve significant accuracy for NSB predictions, depending on distance, AOD, ASY and spectra.

ILLUMINA, unlike other tools, has a high computational cost, is limited to only clear sky conditions, requires detailed input and is not suitable for rapid assessments without any prior optimization (Linares Arroyo et al., 2018). Furthermore, it is not as accurate as previously believed since higher order scattering is required to achieve results within acceptable error limits (Kocifaj et al., 2024).

2.4. Day-Night Band Of Visible Infrared Imaging Radiometer Suite (VIIRS DNB)

Day-Night Band Of Visible Infrared Imaging Radiometer Suite (VIIRS DNB) is the largest of the five instruments aboard the Suomi National Polar-orbiting Partnership (Suomi

NPP) weather satellite operated by the United States National Oceanic and Atmospheric Administration (NOAA). The satellite was launched in 2011, intended to replace the Earth Observing System (EOS) satellites and designed to study climate change and weather conditions.
VIIRS DNB has a broad spectral range of ~500-900 nm, extending into the red, which is wider than those of most ground-based photometers. It is highly advantageous that VIIRS DNB provides global coverage as well as daily measurements, which are corrected for clouds, terrain, vegetation and lunar light (Fernandez-Ruiz et al., 2023). Due to the consistent and long-term data provided it is very useful for monitoring trends.
Some disadvantages of VIIRS DNB are that it only captures intensity instead of color information. It lacks the spectral resolution in the visible bands that are needed to analyze the color composition of artificial lighting. VIIRS DNB also has a lower spatial resolution in comparison to the Digital Single-Lens Reflex (DSLR) images from the ISS. Additionally, it only has a limited ability to detect spectral changes in lighting technologies, like the transition from sodium to LED lighting (Sánchez de Miguel et al., 2021).
VIIRS DNB also shows poor sensitivity in very dark areas and cannot measure over large bodies of water (Fernandez-Ruiz et al., 2023). These constraints should be considered in light pollution studies, when using VIIRS DNB data.

2.5. Sky-Glow Wireless Autonomous Sensor (SG-WAS)

The Sky-Glow Wireless Autonomous Sensor (SG-WAS) is a low cost, fully autonomous, wireless photometer that was designed to measure the NSB and is ideal for remote sites. An example image is shown in Fig. 2.5, where the device can be seen from different angles and where its main elements are numbered.

There are several advantages to using SG-WAS. It is highly accurate, weatherproof, ideal for networks and usage in remote areas and the data is accessible in real time through the IoT-EELab platform (EELabs Project, n.d.). It is a great tool for monitoring light pollution, for astronomical observatories and conducting environmental research.
There are some limitations to the sensor. The spectral range is limited, 400-800 nm, it is slightly less red-sensitive than the Telescope Encoder and Sky Sensor WIFI (TESS-W). There is no heater, which may limit the use of the SG-WAS in cold environments. It also depends on the exposure to sunlight, since it uses solar-powered rechargeable batteries. It recharges in just about four hours of direct sunlight and only needs recharging after about 20 days of operating (Alarcon et al., 2021).
The sensor also takes just one measurement every five minutes, an average of 10 readings, so generally fewer measurements than other sensors like the TESS-W (Fernandez-Ruiz et al., 2023).

Despite its limitations it is a good sensor to choose depending on the use case and it achieves a better calibration error than both the TESS-W and the Sky Quality Meter

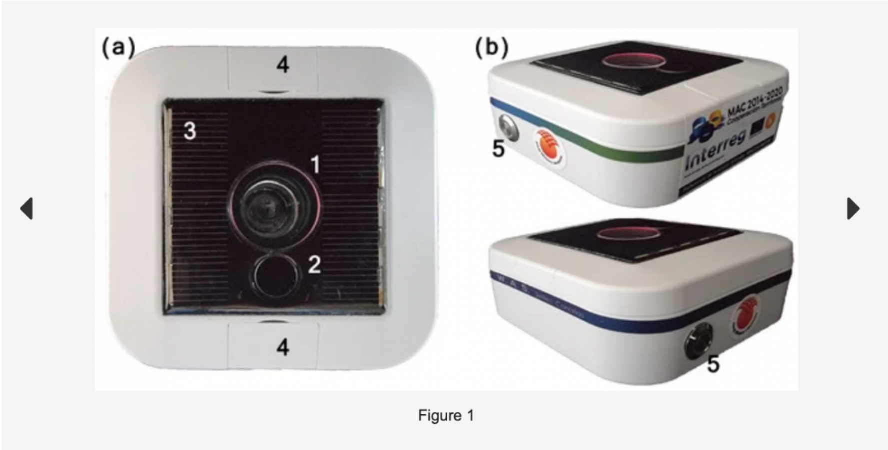

Figure 2.5.: An example image of the SG-WAS shown from different angles with numbers marking the main elements, which are sky brightness optics (1), infrared thermometer (2), solar panel (3), fixing screws (4), and power button (5). From (Alarcon et al., 2021). Reprint with permission.
license by: `https://creativecommons.org/licenses/by/4.0/`

(SQM) (Alarcon et al., 2021).

2.6. Sky Quality Camera (SQC)

The Sky Quality Camera (SQC) is an image processing software developed by Euromix d.o.o. based in Ljubljana, Slovenia. It is designed to process long exposure, all-sky images captured using calibrated DSLR cameras equipped with fisheye lenses. The software enables researchers to assess the brightness and spatial distribution of light across the entire sky, including near the horizon, identify light emitting sources and quantify the impact of ALAN on the environment (Wallner, 2019), (Guk and Levin, 2020), (Simons et al., 2020), (Carias et al., 2021).

The software is calibrated using known star positions used for image alignment. SQC can analyze various aspects of the night sky, including sky brightness, Correlated Color Temperature (CCT), luminance and the location and intensity of light pollution sources (Guk and Levin, 2020), (Simons et al., 2020), (Carias et al., 2021). For the analysis two scales are available, the Normal Scale, with a sky brightness range of 14-24 V mag/arcsec^2 and luminance of up to ∼200 mcd/m^2, and the Las Vegas Scale, with ranges of 11-21 V mag/arcsec^2 and up to ∼4000 mcd/m^2. The different scales with their respective outputs are depicted in the Azimuthal images in Fig. 2.6.
There are several output images available aside from Azimuthal images, such as Cylindrical, Hammer-Aitoff and Info images, examples of which are presented in Fig.s 2.7, 2.8 and 2.9.

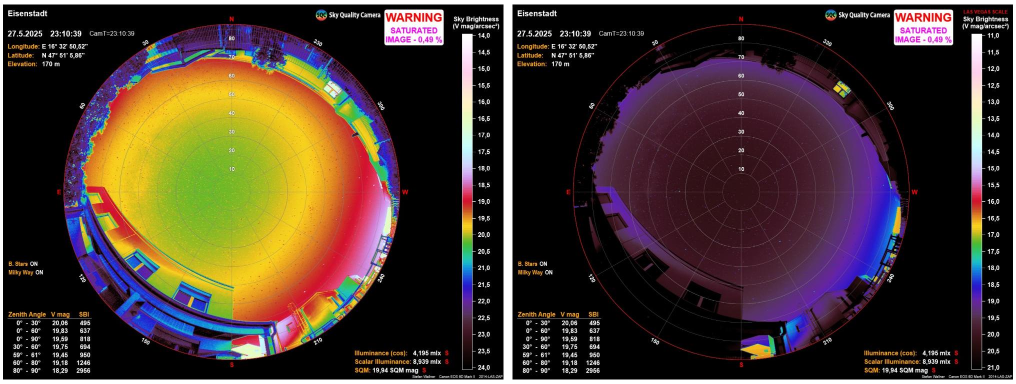

(a) Normal Scale displaying the sky brightness range in mag/arcsec^2.

(b) Las Vegas Scale displaying the sky brightness range in mag/arcsec^2.

Figure 2.6.: SQC output images depicting the two available scales and their respective sky brightness ranges. All images are Azimuthal images. Raw image provided by Stefan Wallner and processed by Raphael Selber. Printed with permission.

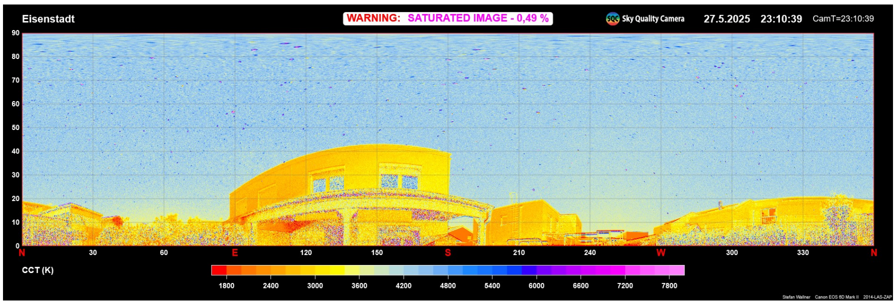

Figure 2.7.: Cylindrical output image with the Normal Scale showing the CCT.Raw image provided by Stefan Wallner and processed by Raphael Selber. Printed with permission.

Field deployment involves mounting the camera on a tripod, leveling it and orienting it to the north. Multiple images should be taken at each location to ensure quality and adjust exposure times as necessary. Optimal exposure times usually range from 30 to 120 seconds, with minimal saturation (Carias et al., 2021). In their study, Simons et al. (2020) selected images with the longest possible exposure and less than 0.1% saturated pixels to compare ground-based measurements with satellite data, finding significant variations in scalar illuminance, luminance and CCT across different spatial scales.
While SQC is a great tool for ground-based light pollution monitoring, it has several limitations.
Similar to other instruments, acquiring images is sensitive to moonlight, weather conditions and is limited to fitting locations. The need for on-site operation further restricts spatial coverage compared to satellites. Calibration and leveling are required each time and exposure times need adjusting to avoid saturation. Additionally, atmospheric scattering

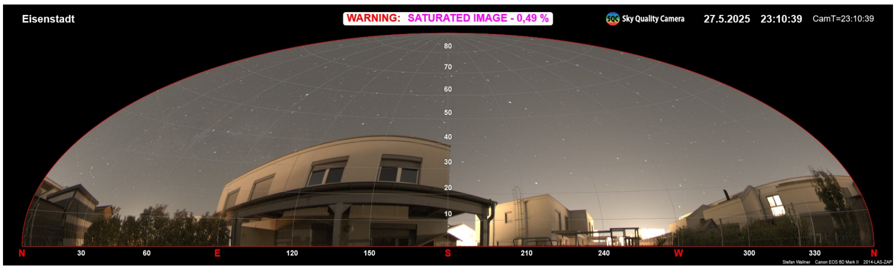

Figure 2.8.: Hammer-Aitoff output image in RGB. Raw image provided by Stefan Wallner and processed by Raphael Selber. Printed with permission.

can affect image quality (Guk and Levin, 2020), (Simons et al., 2020), (Carias et al., 2021).
Overall, SQC proves to be a great tool for researchers for quantifying and visualizing ALAN. It is particularly valuable for validating satellite data and assessing local light pollution impacts. Like any other tool, it has some limitations, especially in spatial coverage. It still remains a useful software for advancing light pollution research.

2.7. Telescope Encoder and Sky Sensor WIFI (TESS-W)

The TESS-W is a low-cost and reliable photometer that was developed under the European-funded STARS4ALL project to measure the NSB and monitor light pollution. It can be used as a fixed installation or in mobile setups, such as on cars or drones. An example image of the TESS-W is shown in Fig. 2.10.

TESS-W uses the same sensor as the SQM and incorporates a dichroic filter which improves its sensitivity to HPS lamps. The spectral range of 400-800 nm, similar to the SG-WAS, is extended into the red to better capture HPS emissions. This range also aligns well with the VIIRS DNB sensor, improving accuracy in urban environments (Fernandez-Ruiz et al., 2023), (Zamorano et al., 2017).
It also includes an infrared sensor to measure the temperature of the sky and estimate cloud coverage, so that data affected by cloud-reflected light can be filtered out. Similarly to the SG-WAS, it transmits data automatically via IoT protocols to the STARS4ALL website[2] (Fernandez-Ruiz et al., 2023). All collected data are stored in open-access repositories, ensuring transparency and accessibility for both researchers and the public. TESS-W is also part of the European Photometer Network initiative, which aims to standardize and coordinate light pollution monitoring across Europe. One of its goals is to promote citizen science by enabling their participation in light pollution monitoring (Zamorano et al., 2017).
The TESS-W can also be connected to a computer or alternatively an Android device to collect data locally. It usually records one measurement per minute, although there are

[2] https://tess.dashboards.stars4all.eu - last access: 24.10.2025, 01:20

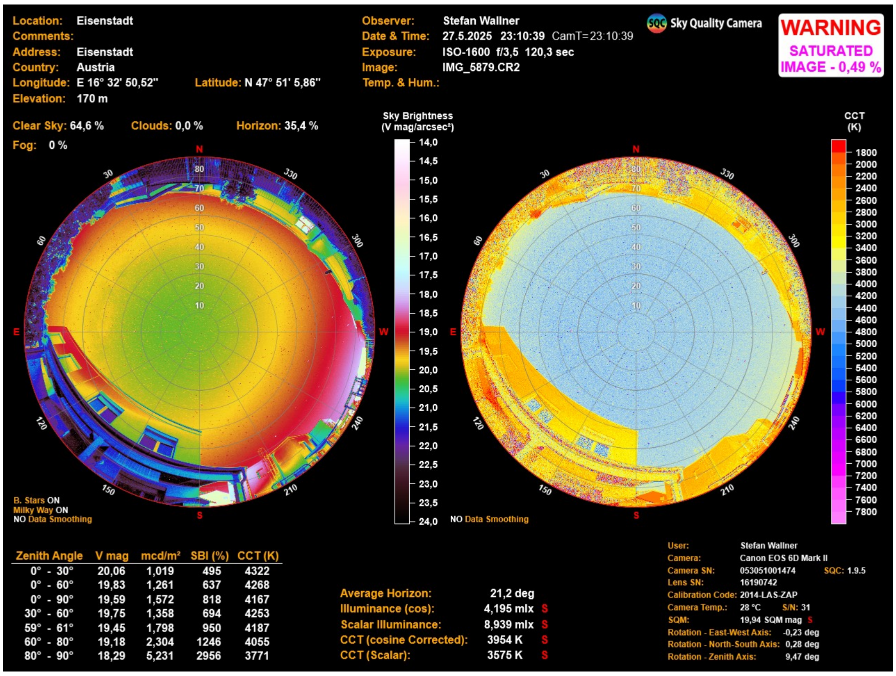

Figure 2.9.: Info image depicting the Sky Brightness and CCT. Raw image provided by Stefan Wallner and processed by Raphael Selber. Printed with permission.

some exceptions of measurements every 10 or 30 seconds (Fernandez-Ruiz et al., 2023). Since its was built for fixed use as well as mobile use, the device is compact and waterproof.

Like every other tool the TESS-W has some limitations and disadvantages. Since it requires WiFi communication and is therefore not autonomous, it is less suitable for remote locations (Fernandez-Ruiz et al., 2023). Due to the extended spectral range it shows a difference of about 0.5 magnitudes in light polluted skies compared to the SQM. Despite this difference, the TESS-W shows consistent results and demonstrates higher sensitivity in light-polluted environments, making it particularly effective for urban monitoring. It also needs calibration to ensure accurate measurements and the spatial resolution is limited unless the photometer is used in mobile mode (Zamorano et al., 2017).

Due to its global deployment, enhanced sensitivity to HPS emissions, and great spectral overlap with VIIRS DNB, the TESS-W is overall a great photometer for measuring the NSB and monitoring light pollution.

2.8. Sky Quality Meter (SQM)

The Unihedron (n.d.b) SQM is a low-cost, compact, ground-based photometer that measures the NSB in units of mag/arcsec^2. With its sensitivity, users are able to quantify

Figure 2.10.: Example image of the TESS-W. Raw image provided by Paul Pacher. Printed with permission.

the quality of the night sky at any time and location (Cinzano, 2005), (Cavazzani et al., 2025), (Bobkowska et al., 2024). The device is globally used in light pollution studies and integrated into observation networks, such as the SQM database (Unihedron, n.d.a).

The SQM operates in the spectral range of 350-700 nm, peaking at 500-550 nm. Several versions are available: The SQM-L, which includes a lens with a 20° FWHM field of view; the SQM-LE, which supports data logging via Ethernet; The SQM-LU, which is a USB connected model; and the standard SQM, which has a wider field of view (Cavazzani et al., 2025). One of the available models is shown in Fig. 2.11.
All versions of the SQM can be handheld, mounted on a tripod, permanently installed or mounted on vehicles, such as cars, boats, balloons or drones. For consistent measurements, it is best to point the device toward the zenith. When mounted on vehicles, however, the orientation may vary, which should be considered (Cavazzani et al., 2025).

The standard SQM includes all stellar objects in its measurements due to its wide field of view, which is broader than that of many other photometers, like the TESS-W and SG-WAS. It measures the night sky brightness as seen from the ground, below the atmosphere, providing a realistic representation of sky conditions for ground-based observers (Cinzano, 2005).
Measurements at zenith using standard SQMs are found to overestimate average brightness as much as 0.3 mag/arcsec^2 (Cinzano, 2005), while the narrow-field versions show a negligible overestimation of average brightness in comparison. Cinzano (2007) thoroughly tested both versions and found the narrow-field versions difference is well under 0.1 mag/arcsec^2 compared to the standard versions 0.3 mag/arcsec^2.
Cinzano (2005) thoroughly tested the device's acceptance angle, linearity and spectral responsivity and analyzed the conversion between its photometric system and standard

Figure 2.11.: Image of an SQM-L. Raw image provided by Raphael Selber. Printed with permission.

systems such as Johnson's B and V bands and CIE photopic and scotopic responses. He found that by adding filters, reasonably accurate multiband data can be obtained. He also determined conversion factors for typical spectra and spectral mismatch correction factors, which are essential when comparing SQM data to standard photometric systems or extending its capabilities with filters.

The SQM is usable during all lunar phases, although some corrections may be necessary. Like any other photometer, it has limitations. It exhibits low sensitivity at longer wavelengths, which might limit the precise assessment of changes in outdoor lighting, such as the replacement of HPS lamps with LEDs. Additionally, it requires empirical calibration for each site, is affected by moonlight and has limited spatial resolution when compared to satellite data (Cavazzani et al., 2025). Its spectral response differs significantly from standard photometric bands, requiring corrections for spectral inconsistencies when comparing data. Its limited accuracy for wavelengths below 400 nm also creates challenges for calibration (Cinzano, 2005).
The SQM is widely used in citizen science projects, environmental impact assessments, astronomy outreach and dark-sky advocacy due to its portability and simplicity. It is particularly valuable in remote or light-polluted areas, where more complex instruments may not be the most suitable. For best results, users should aim the SQM at the zenith,

avoid measurements below 45° elevation unless contamination from ground-based sources is controlled and calibrate the device using known light sources. In comparison with other systems, conversion factors need to be applied and filters can be added for specific photometric bands (Cinzano, 2005).

Due to its ease of use, low maintenance and portability it is suitable for both professional and amateur astronomers, educators and environmentalists.
Overall, the SQM is a practical and accessible tool in the global initiative to monitor and reduce light pollution, bridging the gap between professional research and public engagement.

3. Measurement Campaign

As established, the CEF is a foundational concept in light pollution studies that is exceptionally complex due to the high dependence on several local conditions. To further advance light pollution studies it is necessary to put increased focus on the CEF.
While it would be worth considering improving existing models and building a database of CEFs, it may additionally be useful to simplify the concept.

For this thesis, a limited amount of locations were therefore selected for measurements. The locations are evenly distributed across the city in the directions of the cardinal directions. The aim with this limited dataset was to analyze the resulting CEF of Vienna and determine, if the results accurately represent Vienna‘s NSB and therefore have value in light pollution studies, and proving beyond that, that acquiring CEFs in a simple manner is worth considering to rapidly build global CEF databases.

3.1. A Brief Overview of the Measurement Campaign

The measurements were taken with an SQM at various locations throughout Vienna during the night from the 26th to the 27th of June 2022. Measurements were initially planned to be taken at 13 locations, which unfortunately was not feasible at the time, since the astronomical night was relatively short due to the season. It was planned to take these measurements at three, six and nine kilometers distance from a central measurement location in each cardinal direction. A visualization of what was planned can be seen in Fig. 3.1.

Since it was not possible to take measurements at all 13 locations, the ones at six kilometers distance were neglected, leaving nine measurement locations for this campaign. At each of the nine locations, four measurements were taken, from which the mean was calculated. The coordinates at each location were also noted, in Degree, Minute and Second (DMS). All collected data can be seen in Tab. 3.1.

3.2. Data Preparation and Coordinate System Construction

To plot and analyze the data, the distances between the locations are necessary. With the coordinates from Tab. 3.1 and an online distance calculator [1] the North-South (NS)

[1] https://rechneronline.de/geo-koordinaten/ - last access: 01.10.2025 23:51

Table 3.1.: Measurements at each location from the 26th to the 27th of June 2022, their averages and coordinates (DMS) and the times at which the measurements were taken.

	measurements mag/arcsec^2	average mag/arcsec^2	coordinates (DMS)	time
center	17.78 17.71 17.80 17.90	17.80	N: 48°12'25" E: 16°21'41"	22:46
3km south	18.35 18.28 18.34 18.37	18.34	N: 48°10'47" E: 16°21'55"	23:11
3km west	18.89 18.86 18.62 18.67	18.76	N: 48°12'48" E: 16°20'06"	00:45
3km north	18.76 18.81 18.75 18.73	18.76	N: 48°13'54" E: 16°22'12"	01:04
3km east	18.88 18.85 18.71 18.84	18.82	N: 48°12'10" E:16°24'21"	02:30
9km south	18.85 18.75 18.88 19.04	18.88	N: 48°07'41" E: 16°17'25"	23:31
9km west	19.65 19.65 19.47 19.58	19.59	N: 48°12'09" E: 16°14'56"	00:09
9km north	19.75 19.68 19.81 19.90	19.79	N: 48°18'07" E: 16°19'26"	01:33
9km east	19.30 19.23 19.32 19.30	19.29	N: 48°12'37" E: 16°29'26"	02:08

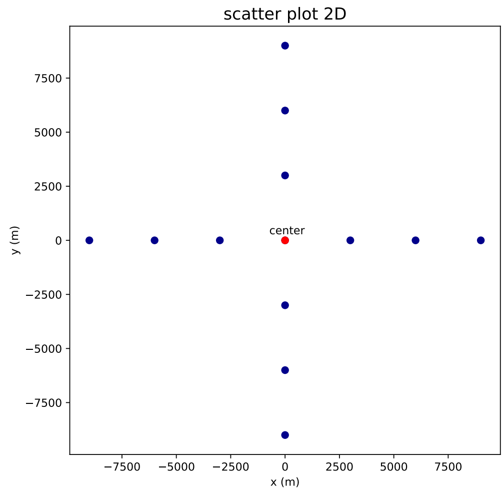

Figure 3.1.: Coordinate system with 13 measurement locations as initially planned. One central measurement location surrounded by 12 more, at three, six and nine kilometer distances in each cardinal direction.

distances and East-West (EW) distances or alternatively the air-line distances between the *central* location at which measurements were taken and every other location can be obtained.
These distances are noted in Tab. 3.2 and 3.3.

Table 3.2.: East-West and North-South distances to central measurement location, where the pluses and minuses denote the shift of the exact location in the coordinate system.

measurement location	East-West distance [m]	North-South distance [m]
3km south	289 (+)	3030 (-)
9km south	5280 (-)	8782 (-)
3km west	1958 (-)	711 (+)
9km west	8347 (-)	495 (-)
3km east	3297 (-)	464 (+)
9km east	9582 (+)	371 (+)
3km north	659 (+)	2752 (+)
9km north	2779 (-)	10575 (+)

With these distances, the theoretical position of these locations in a coordinate system can be calculated.
For this, the first measurement point was placed in the center of the coordinate system, at (0|0), and the farthest point at (x|1).

Table 3.3.: Air-line distances to central measurement location.

point of measurement	[m]
3km south	3044
9km south	10247
3km west	2083
9km west	8361
3km east	3330
9km east	9590
3km north	2830
9km north	10935

The furthest point, *9 km* to the north, has an East-West distance from the central location of 2779 m and a North-South distance of 10575 m. The North-South distance was already normalized to 1, leaving just the x-coordinate, determined by the East-West distance, to be calculated. The following equation was used:

$$x(ew), y(ns) = \frac{1}{10575} \cdot ew, ns \tag{3.1}$$

Both the x- and y-coordinate can be calculated with this equation. The East-West distance determines the x-coordinate and the North-South distance determines the y-coordinate. The calculation for *9 km* to the north looked as follows:

$$\begin{aligned} x(ew) &= \frac{1}{10575} \cdot ew \\ x(ew) &= \frac{1}{10575} \cdot 2779 \\ x(ew) &= \frac{2779}{10575} \\ x(ew) &= 0.263 \end{aligned} \tag{3.2}$$

The coordinate for this location would therefore be (0.263|1).

At this point it is important to consider that not all measurement locations fall into the positive quadrant of the coordinate system. So the correct quadrant for this location needs to be determined. This can be achieved by looking at the map of Vienna, shown in Fig. 3.3(b)[2], where the positions of all locations are marked with pins, revealing the correct signs to use for the coordinates.

To refer back to the example, looking at the map of Vienna, it is evident that the exact location was shifted to the west of the central measurement location. Knowing this, the coordinate can now be placed in the correct quadrant of the coordinate system, meaning

[2]maps created with Google.com/Maps - last access: 01.10.2025 15:28

the x coordinate receives a negative sign. The resulting coordinate is (-0.263|1).
The coordinates for all measurement locations were calculated in the same manner. The results are shown in Tab. 3.4.

Table 3.4.: Coordinates in coordinate system for all measurement locations, calculated using the North-South and East-West distances to the central location.

measurement location	coordinate
central	(0 | 0 | 17.80)
3 km south	(0.027 | -0.287 | 18.34)
9 km south	(-0.499 | -0.830 | 18.88)
3 km west	(-0.185 | 0.067 | 18.76)
9 km west	(-0.789 | -0.047 | 19.59)
3 km east	(0.312 | -0.044 | 18.82)
9 km east	(0.906 | 0.035 | 19.29)
3 km north	(0.062 | 0.260 | 18.76)
9 km north	(-0.263 | 1 | 19.79)

The coordinates using the air-line distances were also calculated using the same Equ. 3.1 and are shown in Tab. 3.5.

The z coordinates in Tab. 3.4 and Tab. 3.5 are determined by the mean of the measured magnitudes at the respective measurement locations and are therefore the same for both coordinate systems.

Table 3.5.: Coordinates in coordinate system for all measurement locations, calculated using the air-line distances and placing all points exactly on the axes.

measurement location	coordinate
central	(0 | 0 | 17.80)
3 km south	(0 | -0.28 | 18.34)
9 km sout	(0 | -0.94 | 18.88)
3 km west	(-0.19 | 0 | 18.76)
9 km west	(-0.76 | 0 | 19.59)
3 km east	(0.30 | 0 | 18.82)
9 km east	(0.88 | 0 | 19.29)
3 km north	(0 | 0.260 | 18.76)
9 km north	(0 | 1 | 19.79)

The coordinate system where all measurement locations were placed along the axes can be seen in Fig. 3.2 and in comparison where the locations are placed in relation to each other in Fig. 3.3(a).
Comparing these two with Fig. 3.3(b), it is clear that Fig. 3.3(a) best represents Vienna

with its measurement locations, which suggests that it would yield better results than the coordinate system shown in Fig. 3.2. Fig. 3.2 will probably result in a good CEF as well, since most locations are placed close to the accurate distribution. But as can be seen by comparing, there are two measurement locations that differ significantly between the two coordinate systems. Therefore it is likely that there will be at least a few areas where the results between these two coordinate systems differ significantly as well.

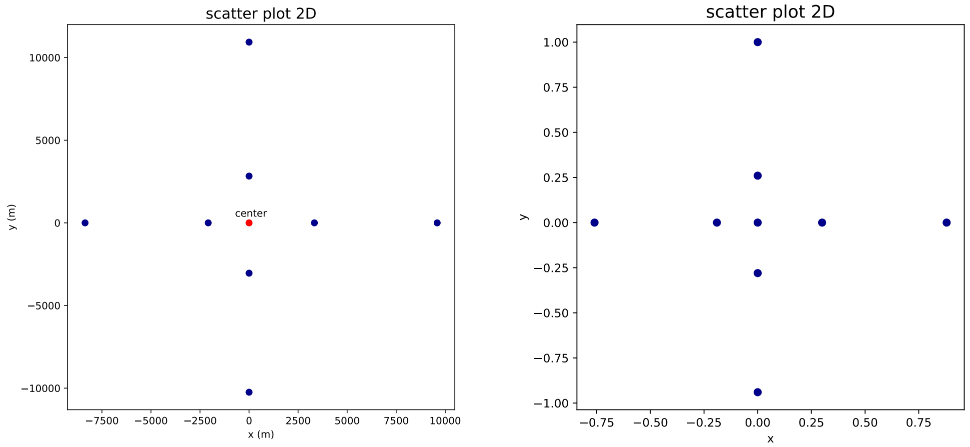

(a) Highlighted central measurement location and axes in (m).

(b) Scatter plot constructed using the calculated coordinates.

Figure 3.2.: Scatter plot of the nine measurement locations, where all of the points are placed directly on the x- and y-axis.

In addition, the coordinates of the stationary SQM at the Department Of Astrophysics, Univ. Vienna (DOA), which took measurements throughout the night, were determined in the same manner as before, using Equ. 3.1. For this, only the North-South and East-West distances were used.
The coordinates, North-South and East-West distances, as well as the resulting coordinate for the coordinate system are displayed in Tab. 3.6.
Tab. 3.7 shows the best and worst measurements that were taken throughout the night, as well as the mean of all measurements in both mag/arcsec^2 and cd/m^2.

Table 3.6.: Coordinates (DMS and calculated) of the SQM at the Department Of Astrophysics, Univ. Vienna.

coordinates (DMS)	NS & EW distance [m]	coordinates in coordinate system
N: 48°13’54" E: 16°20’3"	NS: 2752 (+) EW: 2019 (-)	(-0.191 | 0.260 | 19.55)

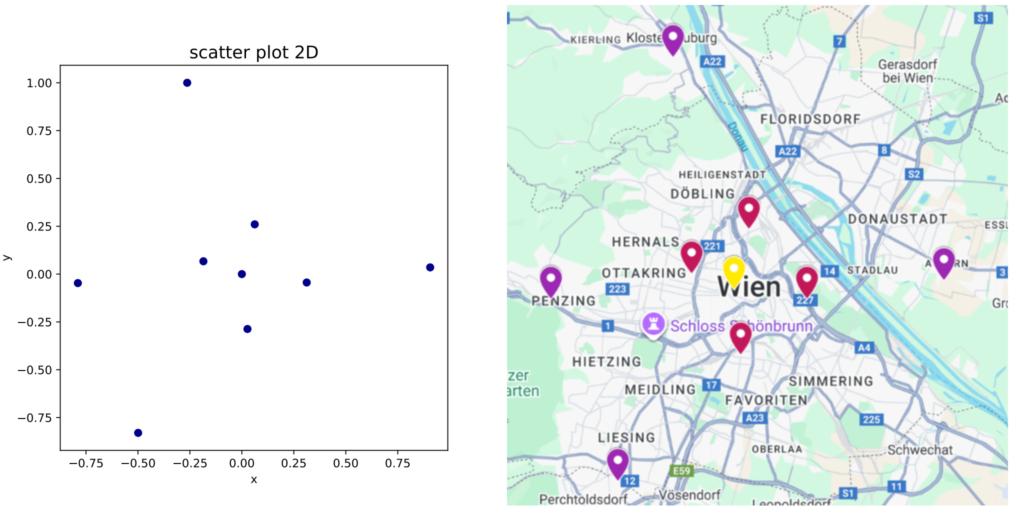

(a) Scatter plot of the nine measurement locations where all of the points are placed more accurately in relation to each other.

(b) Map of Vienna showing the measurement locations in accordance with the coordinates that were noted.

Figure 3.3.: Different visualizations of the measurement locations in Vienna.

Table 3.7.: Best and worst measurement of the SQM at DOA and mean throughout the night in both mag/arcsec^2 and cd/m^2.

	[mag/arcsec^2]	[cd/m^2]	time
best	19.67	0.0015	01:10:15
worst	19.05	0.0026	
mean	19.55	0.0016	

Table 3.8.: Measured magnitude and their respective calculated candela values.

[mag/arcsec^2]	[cd/m^2]
17.80	$8.193 \cdot 10^{-3}$
19.79	$1.310 \cdot 10^{-3}$
18.76	$3.384 \cdot 10^{-3}$
19.29	$2.077 \cdot 10^{-3}$
18.82	$3.202 \cdot 10^{-3}$
18.88	$3.030 \cdot 10^{-3}$
18.34	$4.982 \cdot 10^{-3}$
19.59	$1.576 \cdot 10^{-3}$
18.76	$3.384 \cdot 10^{-3}$

Lastly, the corresponding cd/m^2 values to the measured magnitudes were calculated using Equ. 3.3, which can be found on the Unihedron website[3], which also included an online

[3] http://unihedron.com/projects/darksky/magconv.php - last access: 01.02.2026 20:05

converter.

$$\left[\text{value in cd/m}^2\right] = 10.8 \cdot 10^4 \cdot 10^{-0.4 \cdot \left[\text{value in mag/arcsec}^2\right]} \tag{3.3}$$

Since both cd/m^2 and $mag/arcsec^2$ are main units for measuring light pollution, the analysis of the collected data was done in both units of measurements for comparison. Using Equ. 3.3 or the online tool provided by Unihedron results in the values shown in Tab. 3.8. This equation was implemented into the code shown in Sec. 4 so that a conversion could be done automatically and the plots be produced in both units.

With all of this information, the data can now be processed using Python and the code displayed in Sec. 4.

4. Python Code

```
import numpy as np
import matplotlib.pyplot as plt
from scipy.interpolate import griddata
# from mpl_toolkits import mplot3d

def find_nearest_zvalue(x_arr, y_arr, z_arr, x_search, y_search):
    dx = np.abs(x_arr - x_search)
    dy = np.abs(y_arr - y_search)
    mask = dx==dx.min()
    return z_arr[mask][dy[mask].argmin()]

x_data, y_data, magnitudes = np.genfromtxt('measurements.txt',
                                           unpack=True, skip_header=1)

cmap = 'viridis_r' #cividis_r

# %% Candela
candela = 10.8e4 * 10**(-.4 * magnitudes) * 1000 # millicandela!
z_data = magnitudes

# %% scatter plot 2D
fig = plt.figure(figsize=(6, 6))
plt.scatter(x_data, y_data, color='darkblue')
plt.xlabel('x')
plt.ylabel('y')
plt.title('scatter plot 2D', fontsize=15)
fig.show()
fig.savefig('scatter_plot_2D.pdf')

# %% scatter plot 3D
fig = plt.figure(figsize=(8, 8))
ax = plt.axes(projection='3d')
ax.scatter(x_data, y_data, z_data, color='darkblue')
ax.invert_zaxis()
title = ax.set_title('scatter plot 3D', fontsize=15)
title.set_position([.5, 1.02])
ax.set_xlabel('x')
ax.set_ylabel('y')
ax.set_zlabel(r'$z\;\left[\mathrm{mag/arcsec^2}\right]$', labelpad = 10)
fig.show()
fig.savefig('scatter_plot_3D.pdf')

# %% Interpolation
n_points = 50
x_min, x_max = x_data.min(), x_data.max()
```

```
y_min, y_max = y_data.min(), y_data.max()
x_new = np.linspace(x_min, x_max, n_points + 1)
y_new = np.linspace(y_min, y_max, n_points + 1)

X, Y = np.meshgrid(x_new, y_new)
Z = griddata((x_data, y_data), z_data, (X, Y),
             method='cubic', fill_value=np.nan)

z_inter = Z.flatten()
x_inter = X.flatten()[z_inter > 0.]
y_inter = Y.flatten()[z_inter > 0.]
z_inter = z_inter[z_inter > 0.]

inter = np.column_stack((x_inter, y_inter, z_inter))
np.savetxt('interpolated_data.txt', inter, fmt='%.3f')

# %% 2D plot, colormap
fig, ax = plt.subplots(figsize=(8, 8))
art = ax.pcolormesh(X, Y, Z, cmap=cmap)
cbar = plt.colorbar(art, ax=ax, shrink=0.6)
ax.set_title(f'2D plot, colormap, {n_points+1} interpolation points \n',
    fontsize=15)
ax.set_xlabel('x')
ax.set_ylabel('y')
cbar.set_label(r'$z\;\left[\mathrm{mag/arcsec^2}\right]$', labelpad = 10)
ax.scatter(x_data, y_data, c=z_data, cmap=cmap, s=100, edgecolors='w')
ax.set_aspect('equal')
fig.show()
fig.savefig('2D_plot_colormap_magnitudes.pdf')

# %% surface plot
fig = plt.figure(figsize=(8, 8))
ax = plt.axes(projection='3d')
surface = ax.plot_surface(X, Y, Z, cmap=cmap,
                          rstride=1, cstride=1,
                          vmin=18.00, vmax=19.75,
                          linewidth=0, antialiased=True)
ax.invert_zaxis()
cbar = plt.colorbar(surface, shrink=.5, anchor=(0.5, 0.5))
title = ax.set_title('surface plot', fontsize=15)
title.set_position([.5, 1.02])
ax.set_xlabel('x')
ax.set_ylabel('y')
ax.set_zlabel('z')
cbar.set_label(r'$z\;\left[\mathrm{mag/arcsec^2}\right]$', labelpad = 10)
fig.show()
fig.savefig('surface_plot.pdf')

# %% load interpolated data
x_int, y_int, z_int = np.genfromtxt('interpolated_data.txt', unpack=True)

# %% scatter plot 2D (interpolated data)
fig = plt.figure(figsize=(8, 8))
```

```
plt.scatter(x_int, y_int, color='darkblue')
plt.xlabel('x')
plt.ylabel('y')
plt.title('scatter plot 2D (interpolated data)', fontsize=15)
fig.show()
fig.savefig('scatter_plot_2D_(interpolated_data).pdf')

# %% scatter plot 3D (interpolated data)
fig = plt.figure(figsize=(8, 8))
ax = plt.axes(projection='3d')
ax.scatter(x_int, y_int, z_int, color='darkblue')
ax.invert_zaxis()
title = ax.set_title('scatter plot 3D (interpolated data)',
                     fontsize=15)
title.set_position([.5, 1.02])
ax.set_xlabel('x')
ax.set_ylabel('y')
ax.set_zlabel(r'$z\;\left[\mathrm{mag/arcsec^2}\right]$', labelpad = 10)
fig.show()
fig.savefig('scatter_plot_3D_(interpolated_data).pdf')

# %% scatter plot 3D: interpolated data and measurements
fig = plt.figure(figsize=(8, 8))
ax = plt.axes(projection='3d')
measurements = ax.scatter(x_data, y_data, z_data, marker='^',
                          color='r', label='measurements')
interpolated_data = ax.scatter(x_int, y_int, z_int, marker='.',
                               color='b', label='interpolated data')
ax.invert_zaxis()
title = ax.set_title('scatter plot 3D',
                     fontsize=15)
title.set_position([.5, 1.02])
ax.set_xlabel('x')
ax.set_ylabel('y')
ax.set_zlabel(r'$z\;\left[\mathrm{mag/arcsec^2}\right]$', labelpad = 10)
ax.legend([measurements, interpolated_data],
          ['measurements', 'interpolated data'])
fig.show()
fig.savefig('scatter_plot_3D_measurements_and_interpolation.pdf')
```

Listing 4.1: Data interpolation in Python (in units of magnitudes).

```
import numpy as np
import matplotlib.pyplot as plt
from scipy.interpolate import griddata
# from mpl_toolkits import mplot3d

def find_nearest_zvalue(x_arr, y_arr, z_arr, x_search, y_search):
    dx = np.abs(x_arr - x_search)
    dy = np.abs(y_arr - y_search)
    mask = dx==dx.min()
    return z_arr[mask][dy[mask].argmin()]

x_data, y_data, magnitudes = np.genfromtxt('measurements.txt',
```

```
                                                   unpack=True, skip_header=1)

cmap = 'viridis' #cividis

# %% Candela
candela = 10.8e4 * 10**(-.4 * magnitudes) * 1000 # millicandela!
z_data = candela

# %% scatter plot 3D
fig = plt.figure(figsize=(8, 8))
ax = plt.axes(projection='3d')
ax.scatter(x_data, y_data, z_data, color='darkblue')
title = ax.set_title('scatter plot 3D', fontsize=15)
title.set_position([.5, 1.02])
ax.set_xlabel('x')
ax.set_ylabel('y')
ax.set_zlabel(r'$z\;\left[\mathrm{mcd/m^2}\right]$')
fig.show()
fig.savefig('scatter_plot_3D_candela.pdf')

# %% Interpolation
n_points = 50
x_min, x_max = x_data.min(), x_data.max()
y_min, y_max = y_data.min(), y_data.max()
x_new = np.linspace(x_min, x_max, n_points + 1)
y_new = np.linspace(y_min, y_max, n_points + 1)

X, Y = np.meshgrid(x_new, y_new)
Z = griddata((x_data, y_data), z_data, (X, Y),
             method='cubic', fill_value=np.nan)

z_inter = Z.flatten()
x_inter = X.flatten()[z_inter > 0.]
y_inter = Y.flatten()[z_inter > 0.]
z_inter = z_inter[z_inter > 0.]

inter = np.column_stack((x_inter, y_inter, z_inter))
np.savetxt('interpolated_data_candela.txt', inter, fmt='%.3f')

# %% 2D plot, colormap
fig, ax = plt.subplots()
art = ax.pcolormesh(X, Y, Z, cmap=cmap)
cbar = plt.colorbar(art, ax=ax)
ax.set_title(f'2D plot, colormap, {n_points+1} interpolation points',
    fontsize=15)
ax.set_xlabel('x')
ax.set_ylabel('y')
cbar.set_label(r'$\left[\mathrm{mcd/m^2}\right]$')
ax.scatter(x_data, y_data, c=z_data, cmap=cmap, s=100, edgecolors='w')
ax.set_aspect('equal')
fig.show()
fig.savefig('2D_plot_colormap_candela.pdf')
```

```python
# %% surface plot
fig = plt.figure(figsize=(8, 8))
ax = plt.axes(projection='3d')
surface = ax.plot_surface(X, Y, Z, cmap=cmap,
                          rstride=1, cstride=1,
                          vmin=1.0, vmax=8.0,
                          linewidth=0, antialiased=True,)
cbar = plt.colorbar(surface, shrink=.6)
title = ax.set_title('surface plot', fontsize=15)
title.set_position([.5, 1.02])
ax.set_xlabel('x')
ax.set_ylabel('y')
ax.set_zlabel('z')
cbar.set_label(r'$\left[\mathrm{mcd/m^2}\right]$')
fig.show()
fig.savefig('surface_plot_candela.pdf')

# %% load interpolated data
x_int, y_int, z_int = np.genfromtxt('interpolated_data_candela.txt',
    unpack=True)

# %% scatter plot 2D (interpolated data)
plt.scatter(x_int, y_int, color='darkblue')
plt.xlabel('x')
plt.ylabel('y')
plt.title('scatter plot 2D (interpolated data)', fontsize=15)
fig.show()
fig.savefig('scatter_plot_2D_(interpolated_data)_candela.pdf')

# %% scatter plot 3D (interpolated data)
fig = plt.figure(figsize=(8, 8))
ax = plt.axes(projection='3d')
ax.scatter(x_int, y_int, z_int, color='darkblue')
title = ax.set_title('scatter plot 3D (interpolated data)',
                     fontsize=15)
title.set_position([.5, 1.02])
ax.set_xlabel('x')
ax.set_ylabel('y')
ax.set_zlabel(r'$z\;\left[\mathrm{mcd/m^2}\right]$')
fig.show()
fig.savefig('scatter_plot_3D_(interpolated_data)_candela.pdf')

# %% scatter plot 3D: interpolated data and measurements
fig = plt.figure(figsize=(8, 8))
ax = plt.axes(projection='3d')
measurements = ax.scatter(x_data, y_data, z_data, marker='^',
                          color='r', label='measurements')
interpolated_data = ax.scatter(x_int, y_int, z_int, marker='.',
                               color='b', label='interpolated data')
title = ax.set_title('scatter plot 3D',
                     fontsize=15)
title.set_position([.5, 1.02])
ax.set_xlabel('x')
```

```
ax.set_ylabel('y')
ax.set_zlabel(r'$z\;\left[\mathrm{mcd/m^2}\right]$')
ax.legend([measurements, interpolated_data],
          ['measurements', 'interpolated data'])
fig.show()
fig.savefig('scatter_plot_3D_measurements_and_interpolation_candela.pdf')
```

Listing 4.2: Data interpolation in Python (in units of candela).

The code shown in this Section reads the input file that contains the coordinates that were calculated using the locations and measurements from the measurement campaign. Since there aren't many data points available and the data is scattered, Python's *griddata* can be used for the interpolation. There are three different interpolation methods available: *nearest*, *linear* and *cubic*, which deliver similar results to a certain degree, since they all rely on triangulation of the initial data.
The *nearest* method returns the closest value to the point of interpolation, therefore the interpolated data would equal the initial data.
With the *linear* method a piecewise linear interpolation is performed, where data between two given data points is being calculated. This method produces a continuous, but not smooth, surface.
The *cubic* method similarly calculates data between given data points, but instead returns values determined using a cubic spline, which instead results in a continuous and smooth surface.
For this code, the *cubic* method was used.

The code estimates unknown data values by using the limited amount of known data values from the input file. It takes the data values and estimates the magnitude values in between the given data. It then produces an output file containing the calculated coordinates and magnitudes in between the measured values. There are also various code sections for different plots using either the given or the estimated data or both. The code reads the previously saved data file, produces and then saves the various plots as PDF.

There is also an adapted version that converts the magnitude values into millicandela using the following equation:

$$\left[\text{value in mcd/m}^2\right] = 10.8 \cdot 10^4 \cdot 10^{-0.4 \cdot \left[\text{value in mag/arcsec}^2\right]} \cdot 1000 \tag{4.1}$$

The graph legends and labels were changed accordingly for that version of the code.

4.1. Code Sections and Output Images

With the code several different plots can be produced. The code sections and examples of their corresponding outputs are shown in Figs. 4.1. 4.2. 4.3. 4.4. 4.5. 4.6 and 4.7.

Fig. 4.1(a) shows the section of the code that produces a simple 2D scatter plot of all measurement locations by taking the given x- and y-data from the input file and placing them in a coordinate system. Fig. 4.1(b) shows the output file this produces for our nine measurement locations in Vienna.

```
# %% scatter plot 2D
fig = plt.figure(figsize=(6, 6))
plt.scatter(x_data, y_data, color='darkblue')
plt.xlabel('x')
plt.ylabel('y')
plt.title('scatter plot 2D', fontsize=15)
fig.show()
#fig.savefig('scatter_plot_2D.pdf')
```

(a)

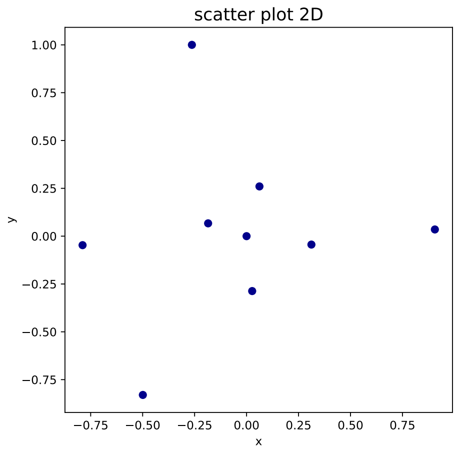

(b)

Figure 4.1.: Code section that produces a 2D scatter plot with resulting image for Vienna using the coordinates from our measurement campaign.

Fig. 4.2(a) produces a similar 2D scatter plot, that shows the interpolated data points instead of the initial data. This is shown in Fig. 4.2(b). This plot is not particularly useful to analyze the NSB of any given city, since it doesn't include the initial or interpolated magnitude values at all and therefore doesn't give any information about the night sky brightness whatsoever. It still might be useful in a joint evaluation with other plots.

The code in Fig. 4.3(a) gives one of the first plots that includes all given data from the input file as it not only plots the measurement locations in a 3D coordinate system, but also shows the corresponding magnitude (or alternatively candela) values, as is shown in Fig. 4.3(b). The 3D plot gives more information about the measurements, but is not as easy to read, unless the plot is rotated and looked at from different angles, which can be done in Python immediately after the output image is produced. Other than that the 3D plot is not too useful in the analysis of the NSB. Since this plot only uses the initial data and none of the interpolated values, it also only gives a better view of the initial data, showing the relation between the different values, without giving any additional information about a city's overall NSB, that is ultimately wanted from the analysis.

The next part of the code in Fig. 4.4(a) produces a 3D scatter plot of the interpolated data values shown in Fig. 4.4(b). This is similar to the 2D scatter plot in Fig. 4.2(b), but

```
# %% scatter plot 2D (interpolated data)
fig = plt.figure(figsize=(8, 8))
plt.scatter(x_int, y_int, color='darkblue')
plt.xlabel('x')
plt.ylabel('y')
plt.title('scatter plot 2D (interpolated data)', fontsize=15)
fig.show()
fig.savefig('scatter_plot_2D_(interpolated_data).pdf')
```

(a)

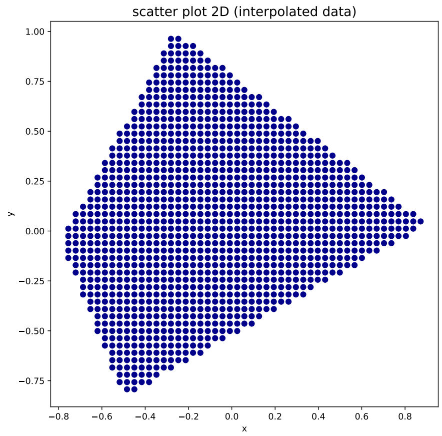

(b)

Figure 4.2.: Code section that produces a 2D scatter plot using the interpolated data and resulting image for Vienna.

```
# %% scatter plot 3D
fig = plt.figure(figsize=(8, 8))
ax = plt.axes(projection='3d')
ax.scatter(x_data, y_data, z_data, color='darkblue')
ax.invert_zaxis()
title = ax.set_title('scatter plot 3D', fontsize=15)
title.set_position([.5, 1.02])
ax.set_xlabel('x')
ax.set_ylabel('y')
ax.set_zlabel(r'$z\;\left[\mathrm{mag/arcsec^2}\right]$', labelpad = 10)
fig.show()
#fig.savefig('scatter_plot_3D.pdf')
```

(a)

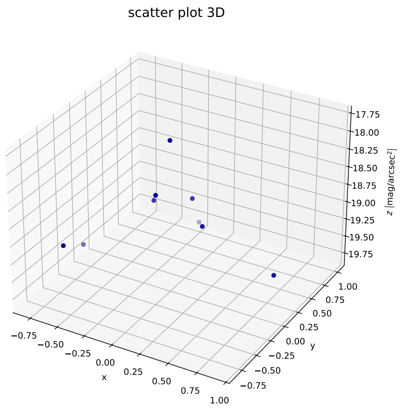

(b)

Figure 4.3.: Code section that produces a 3D scatter plot of the initial data and resulting image.

slightly more useful, because it shows the difference in the interpolated data values and therefore shows the brightness of Vienna's night sky. The 2D plots on the other hand only show the locations where data was interpolated, without giving any information on the interpolated values themselves. It is also similar to the previous plot shown in Fig. 4.3(b), just that it shows the interpolated data values instead of the initial ones. With this first proper view of the interpolated data and Vienna's night sky brightness, it is possible to draw first conclusions, although this is not the best possible plot that can be produced. Like previously mentioned, with 3D plots it is not possible to see all the data, unless the plot can be rotated and evaluated from all angles. Since this is not easily done, there are other plots that are significantly more useful and will be used to analyze the data instead.

The code section shown in the next Fig. 4.5(a) combines the two previous ones and produces a 3D scatter plot showing the measurement locations as well as the interpolated data values. This is shown in Fig. 4.5(b), where the legend shows that the measurement locations are marked with red triangles and the interpolated data values with blue circles. It is quite useful to see the initial data from which the other values have been determined, although this is still not the most useful output.

```
# %% scatter plot 3D (interpolated data)
fig = plt.figure(figsize=(8, 8))
ax = plt.axes(projection='3d')
ax.scatter(x_int, y_int, z_int, color='darkblue')
ax.invert_zaxis()
title = ax.set_title('scatter plot 3D (interpolated data)',
                     fontsize=15)
title.set_position([.5, 1.02])
ax.set_xlabel('x')
ax.set_ylabel('y')
ax.set_zlabel(r'$z\;\left[\mathrm{mag/arcsec^2}\right]$', labelpad = 10)
fig.show()
#fig.savefig('scatter_plot_3D_(interpolated_data).pdf')
```

(a)

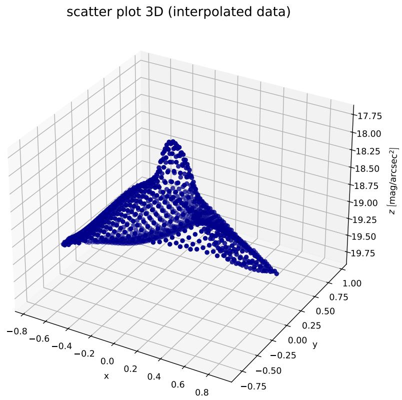

(b)

Figure 4.4.: Code section that produces a 3D scatter plot of the interpolated data and resulting image.

In Fig. 4.6(a) the code section for a similar plot to the previous ones is shown. Now the data is not just scattered throughout the coordinate system, but a surface plot with a colormap is created. The data that is seen in the output Fig. 4.6(b) is much easier to interpret as the colors directly correspond to the magnitude values. Without rotating the output plot it is still impossible to see all the interpolated data values and while it is a better plot for interpreting the data it is still not the best output to use, as it is slightly impractical.

The next code section in Fig. 4.7(a) produces another colormap with the interpolated data, but now in 2D rather than 3D, similar to the first few plots that are produced.

```python
# %% scatter plot 3D: interpolated data and measurements
fig = plt.figure(figsize=(8, 8))
ax = plt.axes(projection='3d')
measurements = ax.scatter(x_data, y_data, z_data, marker='^',
                          color='r', label='measurements')
interpolated_data = ax.scatter(x_int, y_int, z_int, marker='.',
                               color='b', label='interpolated data')
ax.invert_zaxis()
title = ax.set_title('scatter plot 3D',
                     fontsize=15)
title.set_position([.5, 1.02])
ax.set_xlabel('x')
ax.set_ylabel('y')
ax.set_zlabel(r'$z\;\left[\mathrm{mag/arcsec^2}\right]$', labelpad = 10)
ax.legend([measurements, interpolated_data],
          ['measurements', 'interpolated data'])
fig.show()
#fig.savefig('scatter_plot_3D_measurements_and_interpolation.pdf')
```

(a)

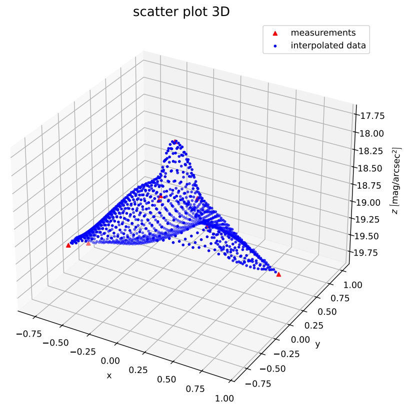

(b)

Figure 4.5.: Code section that produces a 3D scatter plot of the interpolated data, including the initial data, and resulting image.

```python
# %% surface plot
fig = plt.figure(figsize=(8, 8))
ax = plt.axes(projection='3d')
surface = ax.plot_surface(X, Y, Z, cmap=cmap,
                          rstride=1, cstride=1,
                          vmin=18.00, vmax=19.75,
                          linewidth=0, antialiased=True)
ax.invert_zaxis()
cbar = plt.colorbar(surface, shrink=.5, anchor=(0.5, 0.5))
title = ax.set_title('surface plot', fontsize=15)
title.set_position([.5, 1.02])
ax.set_xlabel('x')
ax.set_ylabel('y')
ax.set_zlabel('z')
cbar.set_label(r'$z\;\left[\mathrm{mag/arcsec^2}\right]$', labelpad = 10)
fig.show()
#fig.savefig('surface_plot.pdf')
```

(a)

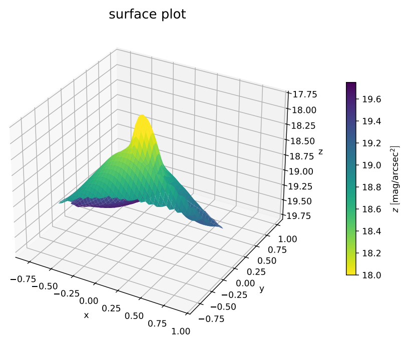

(b)

Figure 4.6.: Code section that produces a 3D surface plot and resulting image.

The result can be seen in Fig. 4.7(b). The same colorbar is used for the 2D colormap as for the 3D surface plot. This plot includes the initial data as well, which is marked for better visualization. When comparing this plot to the previous one, it is clear that all the interpolated data values are visible now and the data can be best interpreted. For the analysis, the focus will therefore mostly be on the colormaps instead of other plots.

```
# %% 2D plot, colormap
fig, ax = plt.subplots(figsize=(8, 8))
art = ax.pcolormesh(X, Y, Z, cmap=cmap)
cbar = plt.colorbar(art, ax=ax, shrink=0.6)
ax.set_title(f'2D plot, colormap, {n_points+1} interpolation points \n',
             fontsize=15)
ax.set_xlabel('x')
ax.set_ylabel('y')
cbar.set_label(r'$z\;\left[\mathrm{mag/arcsec^2}\right]$', labelpad = 10)
ax.scatter(x_data, y_data, c=z_data, cmap=cmap, s=100, edgecolors='w')
ax.set_aspect('equal')
fig.show()
fig.savefig('2D_plot_colormap_magnitudes.pdf')
```

(a)

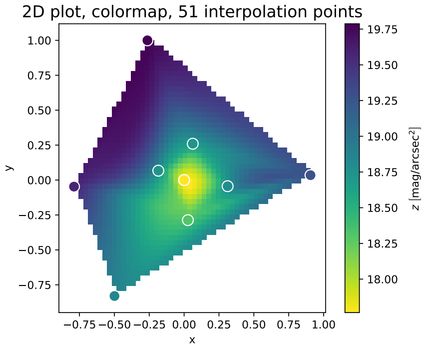

(b)

Figure 4.7.: Code section that produces a colored 2D plot and resulting image.

4.2. Night Sky Brightness and Magnitude Scale

Before taking a closer look at the interpolated data and resulting images, it is important to note, that when measuring NSB in mag/arcsec^2, the scale works inversely. Higher values denote a darker night sky, while lower values denote a brighter night sky. This is generally in correspondence with the color scale that can be seen in the various colormaps throughout Sec. 5.
22.0 mag/arcsec^2 would be an ideal dark sky. A difference of 1 magnitude below that already corresponds to an increase of about 2.512 in NSB, as is evident by looking at equation 4.2, where m_1 and m_2 are the different magnitude values and $\frac{I_2}{I_1}$ is the brightness ratio.

$$\frac{I_2}{I_1} = 10^{0.4(m_1 - m_2)} \tag{4.2}$$

While a difference of ∼2.5 might not seem like much, a decrease in magnitudes corresponds to an *exponential* increase in brightness and therefore noteworthy reduction of visibility. A difference of 5 magnitudes corresponds to a brightness change of 100, as can be calculated using equation 4.2 and is shown in equation 4.3. It is needless to say, that this is a considerable difference. 17.0 magnitudes are typically associated with twilight, moonlit skies and city centers, where barely any stars are visible in comparison to an ideal dark sky at 22.0 magnitudes.

$$
\begin{aligned}
\frac{I_2}{I_1} &= 10^{0.4(m_1-m_2)} \\
\frac{I_2}{I_1} &= 10^{0.4(22-17)} \\
\frac{I_2}{I_1} &= 10^{0.4(5)} \\
\frac{I_2}{I_1} &= 10^{2} \\
\frac{I_2}{I_1} &= 100
\end{aligned} \tag{4.3}
$$

The measured values shown in Sec. 3.2 in Tab. 3.1 range from 17.71 mag/arcsec^2 to 19.90 mag/arcsec^2. So when talking about *dark* and *bright* in the context of the measured and interpolated values, these are the values that are meant. They are *dark* and *bright* for what was measured, but none of the measured values are truly representative of a dark sky and none are even close to a perfect dark sky. The highest measured value of 19.90 mag/arcsec^2 is already ∼6.918 times brighter than a perfect dark sky.
A perfect dark sky at 22.0 mag/arcsec^2 allows visibility of ∼6000 stars with the naked eye. At 19.0 mag/arcsec^2 only ∼500 stars are visible, reinforcing the statement that even small changes have significant impacts.

5. Results and Analysis

The following sections discuss the differently constructed coordinate systems and the difficulties of unit conversion and compare output data for nine and ten initial data points and the different units.
Following that, data from stationary TESS-W photometers in Eisenstadt is prepared in the same manner as was done for Vienna and is then analyzed and compared to that data.

5.1. Vienna Data Analysis

As mentioned in Sec. 4, the main focus of the following analysis will be on the resulting colormaps that were obtained using the SQM data from the measurement campaign that was outlined in Sec. 3.

5.1.1. Comparison of Coordinate Systems

Fig. 5.1(a), 5.2(a) and 5.3(a) show interpolated data points in mag/arcsec^2 using different coordinate systems, with a uniform distribution, an accurate distribution and an accurate distribution using an additional data point, respectively.
The same results are shown in units of mcd/m^2 in Figs. 5.1(b), 5.2(b) and 5.3(b).
The most notable differences show between the uniform distribution and the accurate distribution, as seen in Fig. 5.1(a) compared to Fig. 5.2(a) and Fig. 5.1(b) compared to Fig. 5.2(b). These differences show the importance of using precise spatial data for interpolation, as the scatter plots and therefore the colormaps, shown in Figs. 5.4, 5.5 and 5.6, vary notably depending on the coordinate system. The uniform distribution still provides a reasonable representation of Vienna's NSB that is visualized in the colormaps, but the accurate distribution yields the better results.

5.1.2. Conversion of Units and its Difficulties

During the conversion of units, that was optionally implemented into the code, some interpolated data values close to zero are rounded to exactly zero and thereafter excluded by the code. This leads to data-free zones in the visual output as seen in Fig. 5.2(b). To mitigate this, rounding could be minimized or avoided altogether. Optionally, additional data points could be included in the interpolation.

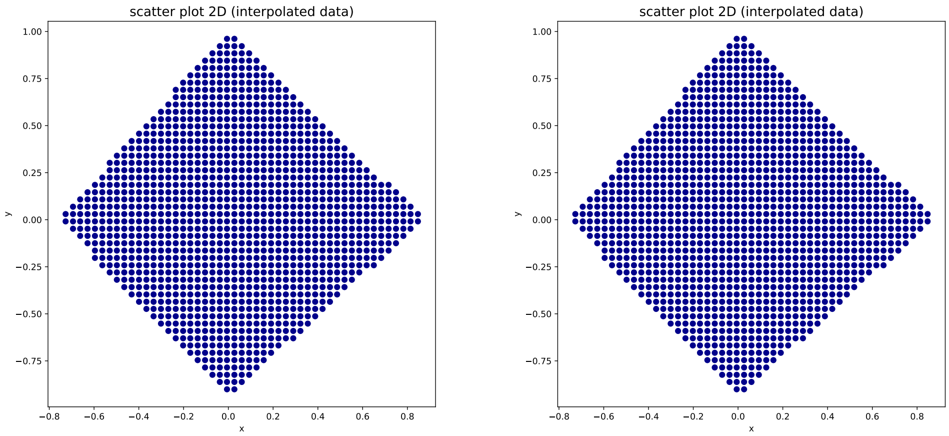

(a) In units of magnitude. (b) In units of candela.

Figure 5.1.: Scatter plot 2D showing interpolated data in different units using a uniform distribution of the initial data.

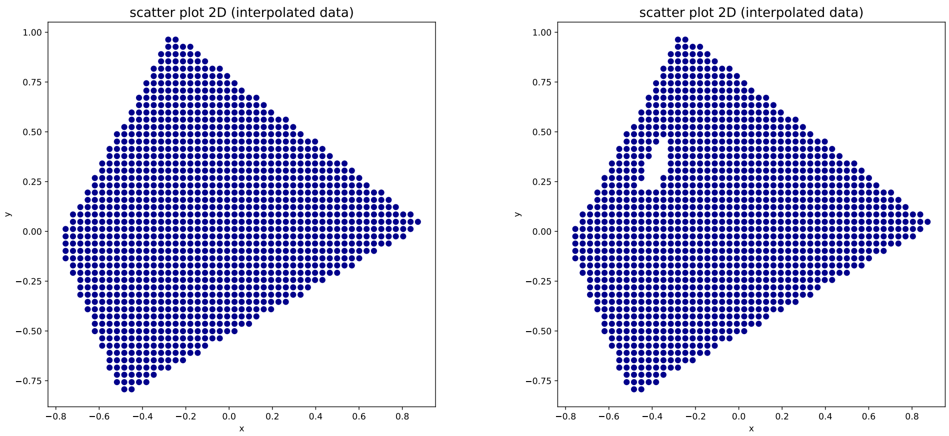

(a) In units of magnitude. (b) In units of candela.

Figure 5.2.: Scatter plot 2D showing interpolated data in different units using an accurate distribution of the initial data.

In the present case, the stationary SQM measured continuously throughout the night of June 26th-27th 2022. Including the average of these measurements in the input file eliminated the data-free area in the resulting 2D scatter plot and colormap shown in Fig. 5.3(b) and 5.6(b).

The scatter plot in Fig. 5.3(a), where no conversion of units was performed, shows

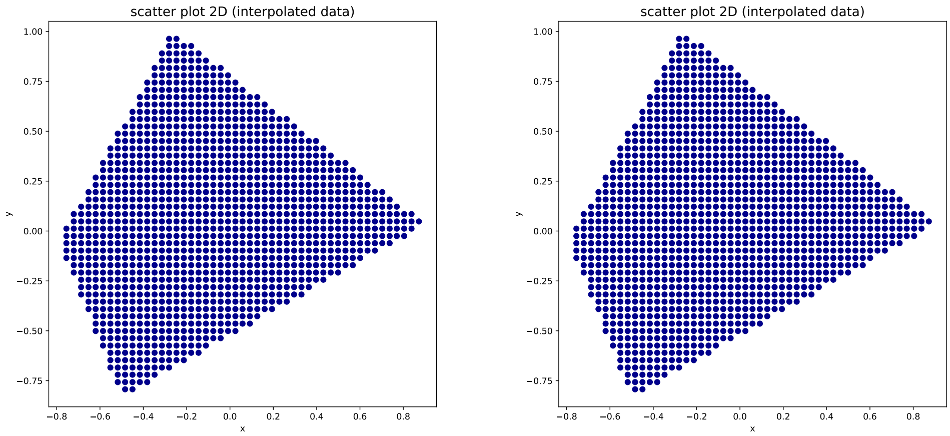

(a) In units of magnitude. (b) In units of candela.

Figure 5.3.: Scatter plot 2D showing interpolated data in different units using an accurate distribution of the initial data and using an additional data point.

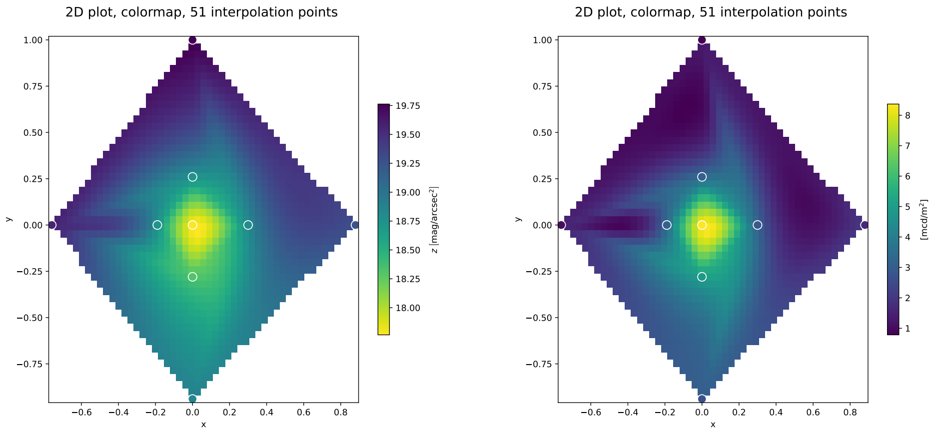

(a) In units of magnitude. (b) In units of candela.

Figure 5.4.: 2D plot colormap of Vienna in different units using nine measurement points and a uniform distribution of the initial data.

no significant change from adding additional data. The colormap in Fig. 5.5(b) on the other hand shows a slight increase in brightness between the DOA SQM and the central measurement location. This increase in brightness underlines the impact that even a single additional data point can have on the results, especially with a small data set.

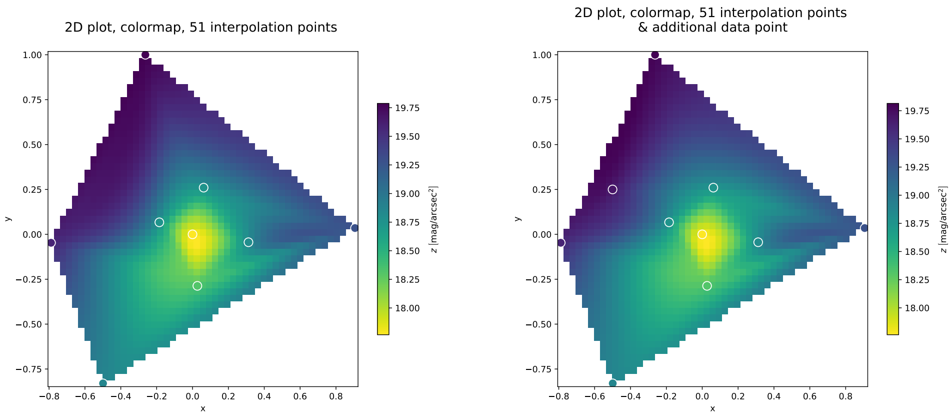

(a) Nine measurement points.

(b) Nine measurement points and additional data point from DOA SQM.

Figure 5.5.: 2D plot colormap of Vienna in units of magnitudes using a more accurate distribution of the initial data.

5.1.3. Comparing Output Data for Nine vs Ten Initial Data Points

As the inclusion of the data from the stationary SQM not only eliminated the data-free zone, but also had an impact on the brightness of Vienna's night sky as represented in the colormap, data from the respective output files was compared.

Tab. 5.1 compares output values of interpolations with and without the additional data point. Changes in magnitude for the selected coordinates range from just 0.008 mag/arcsec^2 to 0.146 mag/arcsec^2, corresponding to percentage differences of 0.04246% and 0.7544%, respectively. While these differences are minor, they corroborate the fact that, especially for limited data sets, every additional data point affects the output.

The results confirm that Vienna's night sky is bright, with the inner districts being considerably brighter than the outskirts. Star visibility with the naked eye ranges from ∼150 in the city center at a measured magnitude of 17.71 to ∼1000 in the outskirts at the highest measured magnitude of 19.90. Even with just nine data points, the analysis results in a useful and meaningful representation of the NSB and CEF of Vienna.

5.1.4. Comparison of Units

Fig. 5.4(b), 5.6(a) and 5.6(b) show 2D colormaps in units of mcd/m^2, which, when compared to their mag/arcsec^2 counterparts shown in Figs. 5.4(a), 5.5(a) and 5.5(b), appear darker due to the use of the same color scale. Due to this, caution is necessary

Table 5.1.: Output data for accurate distribution in coordinate system, both with & without an additional data point, in mag/arcsec^2 and mcd/m^2, were taken at four coordinates. The magnitude values in the second column were used to calculate and therefore verify the output data in candela. The candela values from the output data file are shown in column 3, while the calculated candela values are shown in column 4. The differences between the values in the respective units and as percentages are included.

interpolated coordinate (-0.450 | -0.684)	mag/arcsec^2 (from output file)	mcd/m^2 (from output file)	mcd/m^2 (calculated from magnitude output)	difference mcd/m^2 %
nine data points	18.847	3.150	3.123	0.027 mcd/m^2 0.8608%
10 data points	18.839	3.135	3.146	0.011 mcd/m^2 0.35026%
difference %	0.008 mag/arcsec^2 0.04246%	0.015 mcd/m^2 0.4773%	0.023 mcd/m^2 0.7338%	

interpolated coordinate (-0.518 | 0.122)	mag/arcsec^2 (from output file)	mcd/m^2 (from output file)	mcd/m^2 (calculated from magnitude output)	difference mcd/m^2 %
nine data points	19.599	0.330	1.563	1.233 mcd/m^2 130.27%
10 data points	19.575	1.229	1.597	0.368 mcd/m^2 26.044%
difference %	0.024 mag/arcsec^2 0.12253%	0.899 mcd/m^2 115.33%	0.034 mcd/m^2 2.152%	

interpolated coordinate (-0.314 | 0.195)	mag/arcsec^2 (from output file)	mcd/m^2 (from output file)	mcd/m^2 (calculated from magnitude output)	difference mcd/m^2 %
nine data points	19.425	0.470	1.834	1.364 mcd/m^2 118.4%
10 data points	19.279	1.898	2.098	0.2 mcd/m^2 10.01%
difference %	0.146 mag/arcsec^2 0.7544%	1.428 mcd/m^2 120.6%	0.264 mcd/m^2 13.428%	

when comparing colormaps across different units.

The data-free zone identified earlier in Fig. 5.2(b) appears in Fig. 5.6(a) and was marked for better visibility in Fig. 5.6(c).
While such zones with values at or below zero suggest a dark sky, precise evaluation requires the comparison with magnitude values. In the case at hand, the added SQM data point helped resolve this issue.
For larger cities, more measurements may be necessary to maintain accuracy, though the relatively few data points in this study yielded good results for Vienna's ∼400 km^2 area.

Tabs. 5.2 and 5.1 show that most converted values closely match the output data in units of mag/arcsec^2, showing mostly minor discrepancies due to rounding. For example, a value of 18.839 mag/arcsec^2 equates to 3.146 mcd/m^2, which differs by only 0.011 mcd/m^2, a percentage difference of 0.35026%, from the 3.135 mcd/m^2 of the output file. Nonetheless, larger discrepancies, such as a 12.356%, a 118.4% and a 130.27% difference as seen in Tabs. 5.1 and 5.2, exist. These larger discrepancies highlight the importance of minimizing rounding to avoid errors. Alternatively, the interpolation could be performed solely in units of mag/arcsec^2 and the conversion of units be moved to a later point in the code, such as before transcribing the data into a text file.

While the conversion to candela can provide similarly accurate representations of NSB and therefore the CEF of a city, it introduces complications. If a comparison of units is unnecessary, it is advisable to analyze the results solely in the preferred unit to avoid misinterpretation.
While both units have their advantages, using candela might be beneficial in most cases, since it is an SI-unit.

5.2. Eisenstadt TESS Data

Eisenstadt approximately covers ∼40 km^2 and hosts four permanent measurement locations. Considering Vienna's area coverage of ∼400 km^2, that equates to ∼40 measurement locations for Vienna. Comparing to the nine, or ten, if including the stationary SQM, locations, that amounts to a difference of 75% to 77.5%. Since analyzing Vienna's night sky using nine and ten data points showed promising results, the question arises if a CEF with fewer data points could yield similarly reliable results and if a denser coverage is necessary and should be considered in similar studies.
Eisenstadt seems to be an ideal location to determine this due to the permanent measurement locations and their denser coverage of the city.

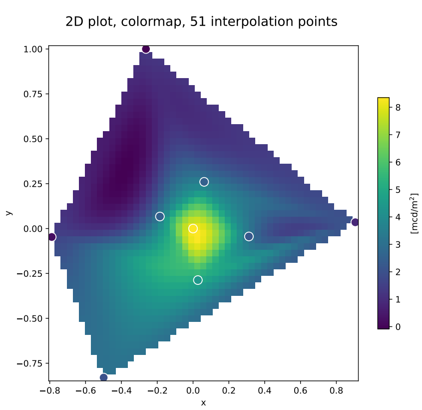

(a) Nine measurement points were used for the interpolation.

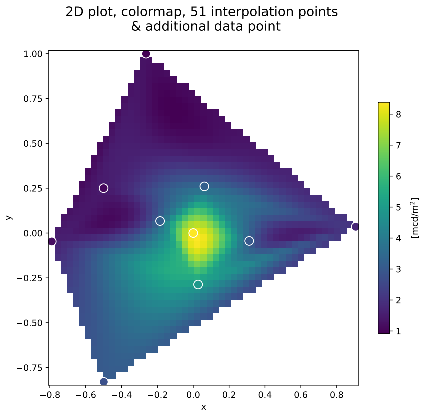

(b) Nine measurement points and additional data point from doa SQM were used for the interpolation.

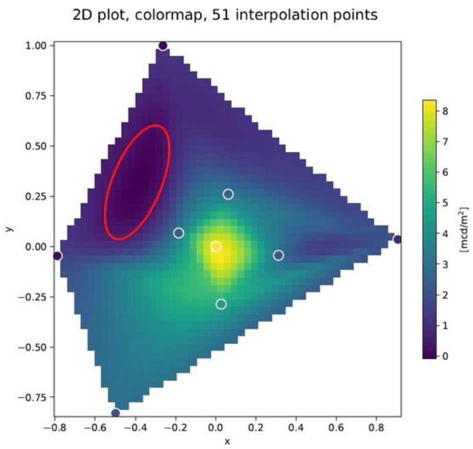

(c) Nine measurement points were used for the interpolation. The data-free area was circled for better visibility.

Figure 5.6.: 2D plot colormaps of Vienna in units of candela using a more accurate distribution of the initial data.

Table 5.2.: Output data for uniform distribution of initial data points in mag/arcsec^2 and mcd/m^2.

<table>
<tr><td colspan="4">(-0.563 | 0.108)</td></tr>
<tr><td>mag/arcsec^2</td><td>mcd/m^2
(from output file)</td><td>mcd/m^2
(calculated from magnitude output)</td><td>difference
mcd/m^2
%</td></tr>
<tr><td>19.422</td><td>1.625</td><td>1.838</td><td>0.214
12.356</td></tr>
<tr><td colspan="4">(0.322 | -0.086)</td></tr>
<tr><td>mag/arcsec^2</td><td>mcd/m^2
(from output file)</td><td>mcd/m^2
(calculated from magnitude output)</td><td>difference
mcd/m^2
%</td></tr>
<tr><td>18.856</td><td>2.971</td><td>3.098</td><td>0.127
4.185</td></tr>
<tr><td colspan="4">(-0.432 | 0.108)</td></tr>
<tr><td>mag/arcsec^2</td><td>mcd/m^2
(from output file)</td><td>mcd/m^2
(calculated from magnitude output)</td><td>difference
mcd/m^2
%</td></tr>
<tr><td>19.159</td><td>2.368</td><td>2.343</td><td>0.025
1.0613</td></tr>
<tr><td colspan="4">(-0.104 | -0.725)</td></tr>
<tr><td>mag/arcsec^2</td><td>mcd/m^2
(from output file)</td><td>mcd/m^2
(calculated from magnitude output)</td><td>difference
mcd/m^2
%</td></tr>
<tr><td>18.871</td><td>2.980</td><td>3.055</td><td>0.075
2.4855</td></tr>
</table>

5.2.1. Data Preparation

The precise locations of the photometers located in Eisenstadt are shown in Tab. 5.3. The data collected by the photometers is automatically uploaded to the STARS4ALL website[1][2], from which it was retrieved for this analysis.

Using the coordinates (DMS) shown in Tab. 5.3, the NS, EW and air-line distances to the *943 - center* location were calculated, as shown in Tab. 5.4. These distances were then used to set up a coordinate system for Eisenstadt, as previously done for Vienna. The specific coordinates used for the interpolation are shown in Tab. 5.5 and visualized

[1] https://tess.dashboards.stars4all.eu/d/tess_network_map/map?orgId=1 - last access: 24.10.2025 01:20

[2] https://tess.dashboards.stars4all.eu/d/tess_comparison_8/s4a-photometer-network-8x-comparison?orgId=1&var-Tess_1=stars941&var-Tess_2=stars942&var-Tess_3=stars943&var-Tess_4=stars944&var-Tess_5=stars1120&var-Tess_6=none&var-Tess_7=none&var-Tess_8=none&from=1743718902000&to=1743735688000 - last access: 07.11.2025 04:42

Table 5.3.: Coordinates (DMS) of the TESS photometers in Eisenstadt.

location	coordinates
943 - center	N: 47°50'48" E: 16°31'28"
941 - west	N: 47°50'21" E: 16°29'54"
944 - east	N: 47°51'02" E: 16°33'08"
1120 - south	N: 47°49'46" E: 16°32'43"

in Fig. 5.7(a)[3]. A comparative 2D scatter plot is shown in Fig. 5.7(b).
The air-line distances were included in Tab. 5.4, but a coordinate system using these was not set up. Analyzing and comparing the measured data for Vienna already proved that the accurate distribution turns out to be the most useful. Therefore the focus will solely be on the resulting colormaps using the accurate distribution of the TESS locations.

Table 5.4.: Different distances to *943 - center* TESS location. The pluses and minuses denote the shift of the exact location in the coordinate system.

measurement location	east-west distance [m]	north-south distance [m]	air-line distance
941 - west	1951 (-)	835 (-)	2122
944 - east	2075 (+)	433 (+)	2120
1120 south	1557 (+)	1917 (-)	2470

Table 5.5.: Coordinate system for Eisenstadt with accurate distribution of measurement locations.

location	x-coordinate	y-coordinate
943 - center	0	0
941 - west	-0.940	-0.402
944 - east	1	0.209
1120 - south	0.750	-0.924

Light pollution measurements are typically performed around the new moon phase, when the sky is at its darkest. Two suitable windows were identified. From November 28th to December 8th 2024 and from March 26th to April 5th 2025, with dates for the new moon being December 1st 2024 and March 29th 2025. While these are not the only possible periods for data collection, they were selected for this analysis.
Data was collected for six nights during these windows. November 29th & 30th 2024, December 1st & 2nd 2024 and April 2nd & 3rd 2025. For each night, the start and end

[3] maps created with Google.com/Maps - last access: 01.10.2025 15:28

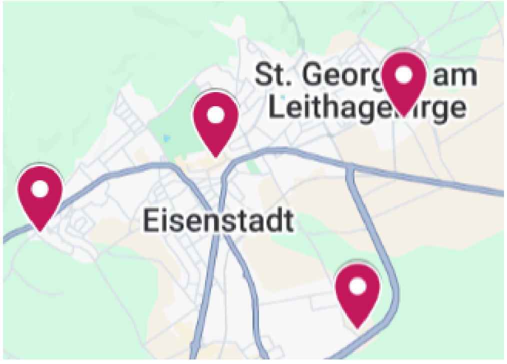

(a)

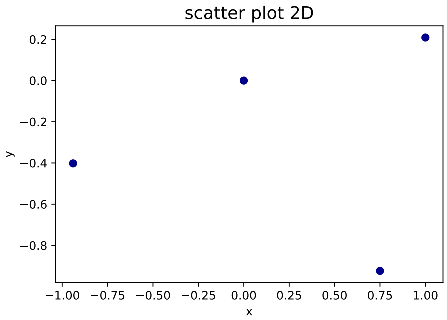

(b)

Figure 5.7.: TESS locations in Eisenstadt in a map and coordinate system.

of astronomical twilight were noted to ensure data was only used from true astronomical night.

Table 5.6.: Start and end of astronomical twilight for the six chosen nights.

date	start	end
28.11.2024		17:55
29.11.2024	05:28	17:55
30.11.2024	05:29	17:55
01.12.2024	05:30	17:54
02.12.2024	05:31	
01.04.2025		21:12
02.04.2025	4:41	21:14
03.04.2025	4:39	

The start and end times for astronomical twilight are shown in Tab. 5.6[4]. It is clear that the nights in November and December offer a longer window for data collection, while the nights in April show shorter windows, due to seasonal changes. For example, on April 3rd 2025 astronomical twilight already began at 4:39 a.m., which is almost an hour earlier compared to December 2024. Even if the data from April 3rd 2025 comes close to astronomical twilight, it still falls within the acceptable time frame.
For each selected night, ten measurements were taken around the targeted time and the average calculated. Due to the frequent measurements, the collected data span a time of approximately 10 minutes. For instance, the average NSB value of 19.39 mag/arcsec^2 at the *943 - center* location during the 29th of November 2024 around 1 a.m. was obtained from 10 measurements taken between 00:54:03 and 01:03:05 a.m. The exact times and measurements for all selected nights and locations are displayed in Tabs. A.1, A.2, A.3,

[4]https://www.timeanddate.de/sonne/oesterreich/eisenstadt?month=12&year=2024 - last access: 24.10.2025 16:53

A.4, A.5 and A.6.
This was done for all days and locations. The time ranges show slight variations due to the irregular intervals in which the TESS photometers collect data. The resulting average values are presented in Tabs. A.7, A.8, A.9, A.10, A.11 and A.12.
Data was collected from both cloudless nights and fully overcast nights.
Using the coordinate system from Tab. 5.5 and the average values from Tabs. A.7, A.8, A.9, A.10, A.11 and A.12, input files were generated for the Python code in Sec. 4. With these, plots in both units of mag/arcsec^2 and mcd/m^2 were produced, equivalent to those created for Vienna. The analysis will focus solely on the 2D colormaps.

5.2.2. Data Analysis

Figs. 5.8(a), 5.8(c), 5.8(e) and 5.8(g) show the NSB between 1 and 4 a.m. on November 29th 2024, a cloudless night. The night sky appears relatively bright early on, but shows a notable decrease in overall brightness at 3 and 4 a.m.
In contrast, the following night depicted in Figs. 5.8(b), 5.8(d), 5.8(f), 5.8(h) appears darker overall despite total cloud cover. This is unexpected, as clouds typically amplify light pollution.

Interpolated values from the two nights in Fig. 5.8 are shown in Tab. 5.7, including brightness ratios between hourly values.
The values show that the NSB fluctuates constantly throughout the nights. The largest difference appears in the night of November 30th, where the NSB changes from 20.172 mag/arcsec^2 around 2 a.m. to 18.554 mag/arcsec^2 around 4 a.m., which is a difference of 1.618 mag/arcsec^2 and a brightness ratio of 4.438 which equates to a brightness change of $\sim$444%.
This data emphasizes the fact, that the CEF changes constantly over time and space. Considering that the night of November 30th appeared darker overall despite total cloud cover, which the data displayed in Tab. 5.7 confirms, it is evident that analyzing data is overly complicated due to the nature of the CEF and the lack of applicable reference data.

The following nights in December were cloudless and show a uniform night sky. No fluctuations in NSB are immediately visible when looking at Fig. 5.9.
The output files for these nights would undoubtedly reveal fluctuating data as well, merely with smaller brightness ratios.

Fig. 5.10 present the data from April 2025. Figs. 5.10(a), 5.10(c), 5.10(e) and 5.10(g) depict data from a cloudless and relatively bright night, with little fluctuations between hours.
Figs. 5.10(b), 5.10(d), 5.10(f) and 5.10(h) show data from April 3rd, where cloud cover transitions from full in Figs. 5.10(b) & 5.10(d) to clear in Figs. 5.10(f) & 5.10(h) between 2 and 3 a.m. The night sky appears brightest at 1 and 2 a.m., gradually darkening by the hour, showing a significant reduction in brightness by 4 a.m.

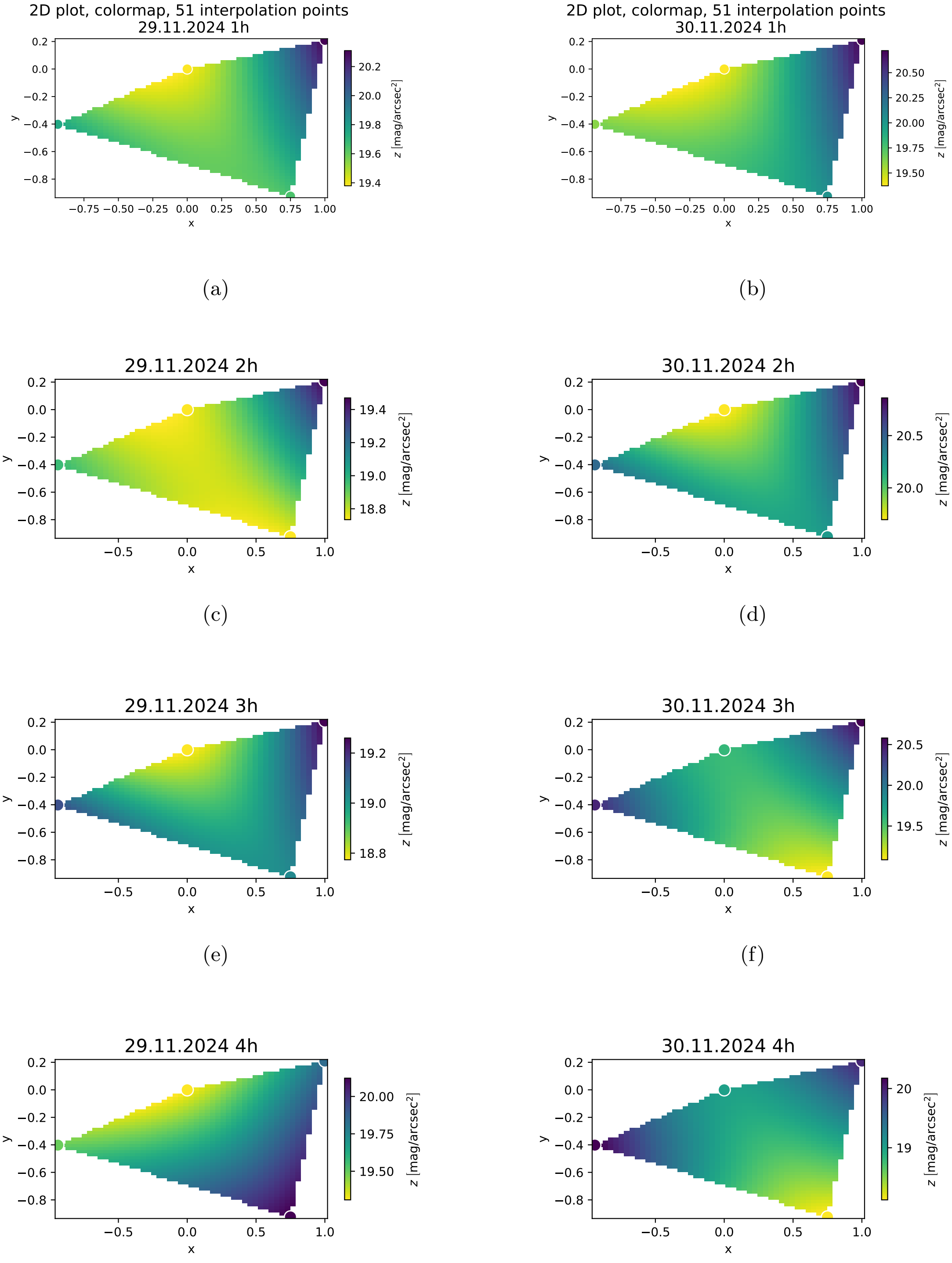

(a) (b) (c) (d) (e) (f) (g) (h)

Figure 5.8.: Two nights between 1 a.m. and 4 a.m. with no cloud cover and full cloud cover, respectively.

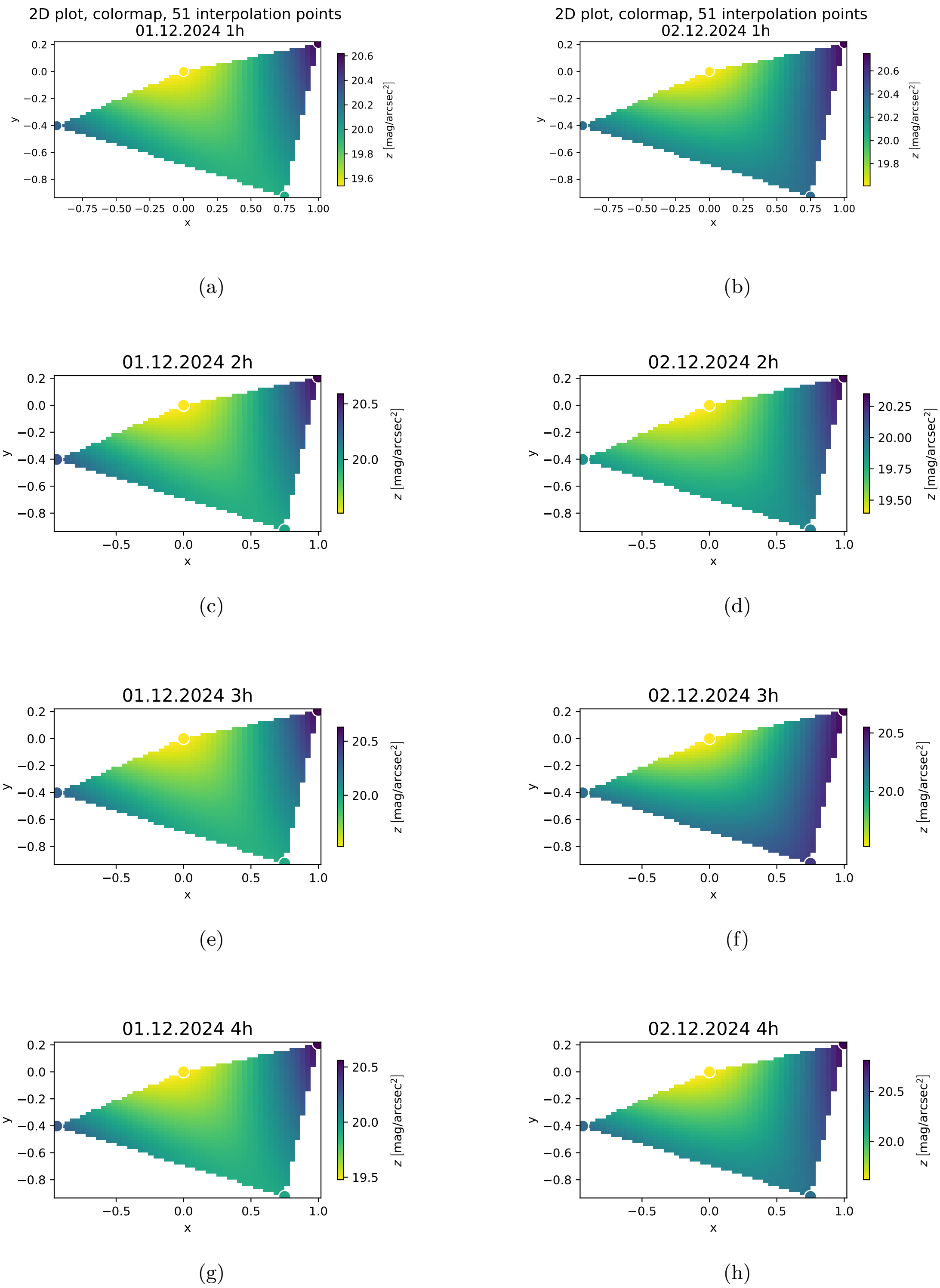

Figure 5.9.: Two nights between 1 a.m. and 4 a.m. with no cloud cover.

Table 5.7.: Interpolated data values from three locations in Eisenstadt. The data was collected for two nights. The brightness ratio between the interpolated values after each hour is shown.

date & time	(0.922 | -0.131)	brightness ratio	(-0.319 | -0.471)	brightness ratio	(0.263 | -0.765)	brightness ratio
29.11.2024 1 a.m.	20.090		19.598		19.599	
		2.194		2.036		2.178
29.11.2024 2 a.m.	19.237		18.826		18.754	
		1.057		0.851		0.792
29.11.2024 3 a.m.	19.177		19.001		19.007	
		0.502		0.572		0.435
29.11.2024 4 a.m.	19.926		19.607		19.912	
30.11.2024 1 a.m.	20.493		19.639		19.838	
		0.874		0.617		0.735
30.11.2024 2 a.m.	20.639		20.163		20.172	
		1.657		1.397		2.176
30.11.2024 3 a.m.	20.091		19.800		19.328	
		1.916		1.559		2.040
30.11.2024 4 a.m.	19.385		19.318		18.554	

The data presented in Tab. 5.8 reveals just how significant this reduction is. The night sky darkens by values of 1.795-2.085 mag/arcsec^2 depending on the interpolated locations from Tab. 5.8. This corresponds to brightness ratios of 5.22-6.82.
The data confirms what is already clearly visible in Figs. 5.10(b), 5.10(d), 5.10(f) and 5.10(h), that throughout the entire city, the night sky darkens after the cloud cover disappears. Around 1 a.m. the interpolated values reach barely 18 mag/arcsec^2, while at the end of the night there are values of just over 20 mag/arcsec^2. Star visibility ranges from ∼200 stars to ∼1500 stars within these margins.

Table 5.8.: Interpolated data from four locations throughout the night of the 3rd of April 2025.

	1 a.m.	2 a.m.	3 a.m.	4 a.m.
(-0.242 | -0.267)	18.013	18.463	18.913	19.850
(0.806 | -0.403)	18.302	18.718	19.532	20.387
(0.302 | -0.516)	18.081	18.527	19.065	20.066
(0.224 | -0.222)	18.073	18.522	18.998	19.868

The values from Tab. A.7 were converted to mcd/m^2 and the colormaps shown in Fig. 5.11 were produced for comparison. These output images, unlike the ones for Vienna, do not exhibit data-free areas. Additionally, they closely match the output images in mag/arcsec^2.

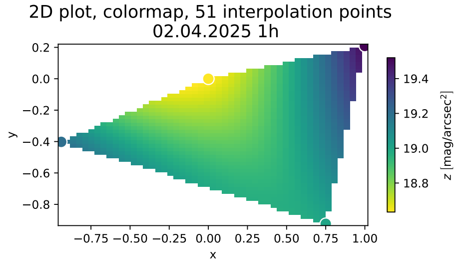

(a)

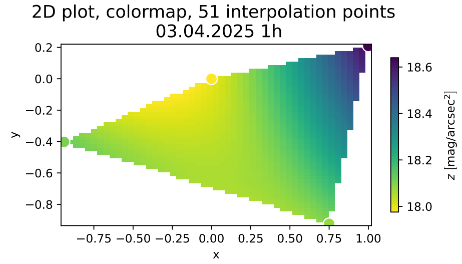

(b)

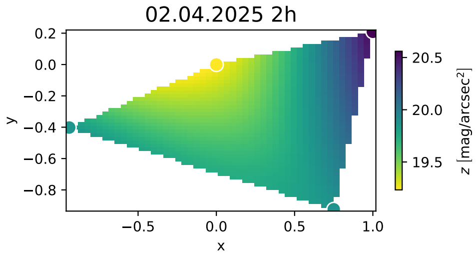

(c)

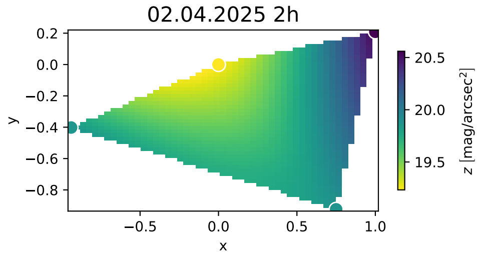

(d)

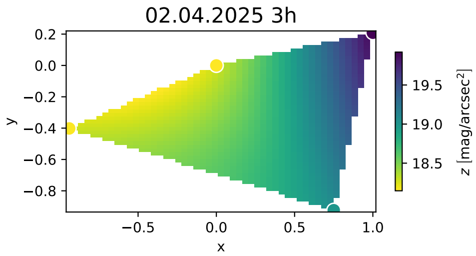

(e)

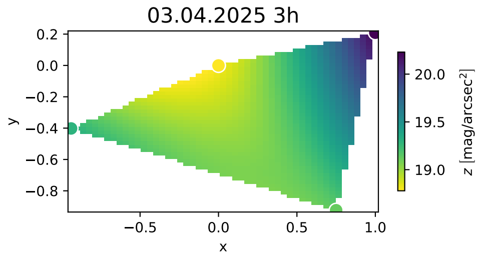

(f)

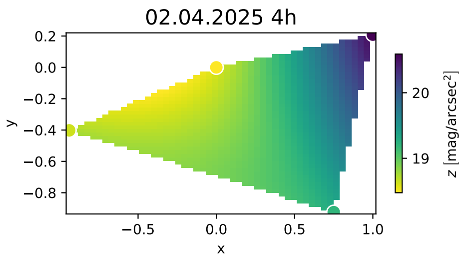

(g)

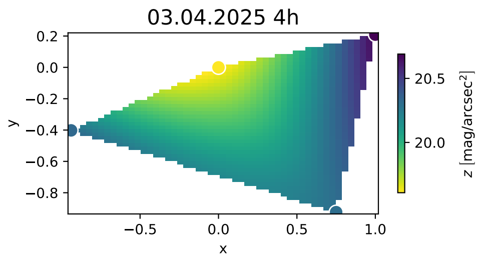

(h)

Figure 5.10.: Two nights between 1 a.m. and 4 a.m. one with full cloud cover, the other with full cloud cover changing to no cloud cover between 2 a.m. and 3 a.m.

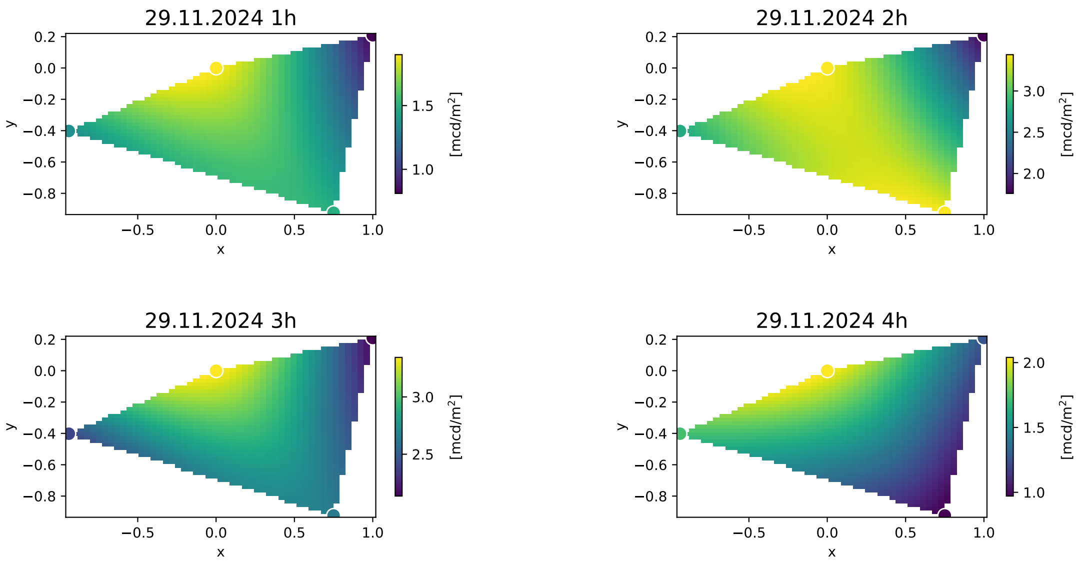

Figure 5.11.: Eisenstadt TESS data from the 29.11.2024 in units of candela.

Table 5.9.: Average mag/arcsec^2 values between 1 and 4 a.m. from November 29th.

location	941 - west	943 - center	944 - east	1120 - south
mag/arcsec^2	19.32	19.06	20.00	19.37

The aforementioned denser coverage in Eisenstadt could be a contributing factor to the absence of data-free areas in the interpolated data files and resulting output images.
Considering that a single additional data point in Vienna, was sufficient to eliminate the data-free area, it is reasonable to assume that 40 measurements are not absolutely necessary for larger cities. Adding four measurement locations at around six kilometers distance from the central location, as was initially planned, would likely suffice to ensure appropriate coverage and an accurate conversion of units.
These findings reinforce the importance of spatial coverage and show that larger cities require proportionally more measurement locations. The results from Eisenstadt and Vienna could serve as a reference for appropriate scaling for cities of varying sizes.

In Fig. 5.11, the first selected night, is shown in mcd/m^2. The results are quite similar to their mag/arcsec^2 counterpart, despite the usage of the same color scale. This could be attributed to the smaller area and denser coverage of measurement locations in Eisenstadt.

Table 5.10.: Average mag/arcsec^2 values between 1 and 4 a.m. from November 30th.

location	941 - west	943 - center	944 - east	1120 - south
mag/arcsec^2	20.01	19.31	20.53	19.40

Table 5.11.: Average mag/arcsec^2 values between 1 and 4 a.m. from December 1st.

location	941 - west	943 - center	944 - east	1120 - south
mag/arcsec^2	20.28	19.50	20.59	19.95

Table 5.12.: Average mag/arcsec^2 values between 1 and 4 a.m. from December 2nd.

location	941 - west	943 - center	944 - east	1120 - south
mag/arcsec^2	20.17	19.53	20.61	20.25

To confirm this, more nights and possibly more differently sized cities with varying coverage of measurement locations should be evaluated. With this, a possible connection could be found, showing why the conversion of units resulted in very similar results for Eisenstadt, but not for Vienna.

Tabs. 5.9, 5.10, 5.11,5.12, 5.13 and 5.14 show the average mag/arcsec^2 values between 1 and 4 a.m. during the selected nights. The data is visualized in Fig. 5.12.
Comparing the results using the average values in Fig. 5.12 with the results throughout the nights in Fig. 5.8, 5.9 and 5.10 show that the averages give a good overview over the NSB. For days with minimal fluctuations, as December 1st, the average accurately represents the NSB throughout the entire night, as expected. For other nights, where brightness fluctuates more, the average portrays a composite representation of the NSB throughout the nights.
Since using the average values throughout the nights results in accurate representations of the NSB and data is available on the STARS4ALL website, it would certainly be possible to analyze the average NSB of a well covered city like Eisenstadt over a broader time span. This could be used to feed global databases of CEFs and simplify light pollution monitoring for such cities through visualization.
Additionally, these colormaps could be used to identify places of high light pollution, where ways for mitigation should be implemented first.
In larger cities, provided that enough data was collected, they could be used to locate the best possible places for observatories within cities.

Table 5.13.: Average mag/arcsec^2 values between 1 and 4 a.m. from April 2nd.

location	941 - west	943 - center	944 - east	1120 - south
mag/arcsec^2	18.89	18.55	19.86	19.12

Table 5.14.: Average mag/arcsec^2 values between 1 and 4 a.m. from April 3rd.

location	941 - west	943 - center	944 - east	1120 - south
mag/arcsec^2	18.73	18.44	19.30	18.73

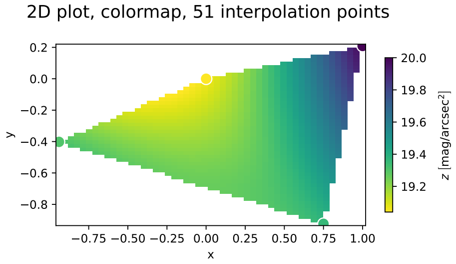

(a) Average NSB of November 29th.

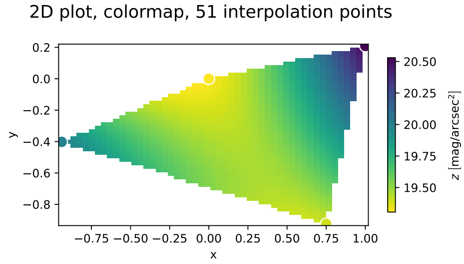

(b) Average NSB of November 30th.

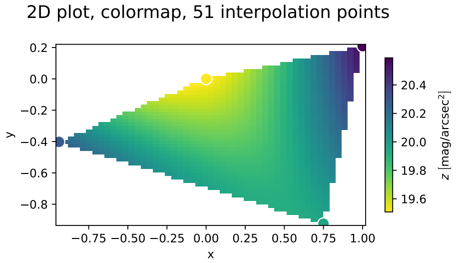

(c) Average NSB of December 1st.

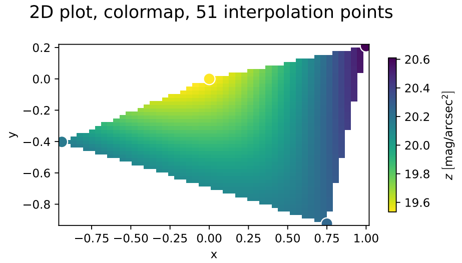

(d) Average NSB of December 2nd.

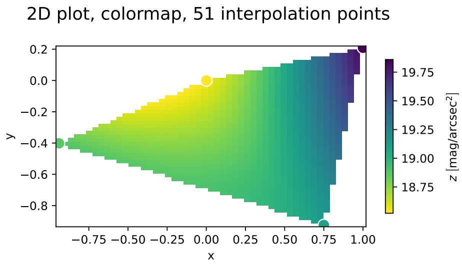

(e) Average NSB of April 2nd.

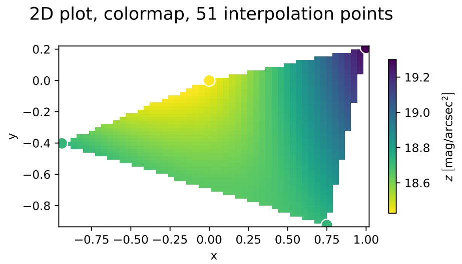

(f) Average NSB of April 3rd.

Figure 5.12.: Visualization of the average NSB of six nights in Eisenstadt between 1 and 4 a.m.

6. Conclusion

This thesis studied one of the fundamental concepts of light pollution modelling, the CEF. To advance light pollution studies and ultimately implement more ways of mitigating its various and severe impacts on humans, wildlife and astronomical research, there should be increased focus on this concept and advancement of its understanding.
Due to the CEFs complexity, there is no all-encompassing, final definition. As an accurate representation is essential for various guiding policies, astronomical site selection and predictive modelling, it could be advantageous to simplify the retrieval of CEFs while maintaining accuracy. This raises the question, if an accurate CEF can be obtained with a limited amount of data which thus was the primary objective of this thesis.

Ground-based NSB measurements were conducted with an SQM at nine locations in Vienna. Additionally, data from a stationary SQM in Vienna and four stationary TESS-W photometers in Eisenstadt were used.
To analyze the collected data, the Python code shown in Sec. 4, which interpolates the given data using Python's *griddata* function and *cubic* method, was written. The code produces various plots using the initial, the interpolated or both data.

The data presented in Sec. 5.1 accurately represents Vienna's night sky, showing a bright city center and darker outskirts within the measured range of 17.71-19.90 mag/arcsec^2, where star visibility ranges from ∼150-1000.
Additionally, the results shown in Sec. 5.2.2, depict significant fluctuations in NSB throughout several nights. The night of April 3rd 2025 displays changes of 1.795-2.085 mag/arcsec^2 depending on location. These correspond to brightness ratios of 5.22-6.82, which denotes a significant change in star visibility and darkening of the night sky.
The results presented in Sec. 5.2.2, which use the average values for the selected nights, show that it is possible to obtain a general overview of the NSB throughout the night without having to perform multiple evaluations. For nights with little fluctuation throughout the night, an accurate representation of the overall NSB is obtained, while for nights with strong fluctuations, a composite image throughout the night is obtained.

The analysis for both Vienna and Eisenstadt, in both units of mag/arcsec^2 and mcd/m^2, reveals that larger cities necessitate more measurement locations to ensure the required coverage for accurate results in either unit.
The results presented in Sec. 5.1 exhibit a data-free area after converting to mcd/m^2. This is due to rounding to the third decimal and could therefore be avoided in several ways: rounding to more decimals, avoiding rounding altogether, ensuring denser data coverage or converting units only after data interpolation is completed.

Overall, the presented results show that a limited dataset, provided there is even and decent coverage over a city, can accurately depict its NSB. Furthermore, the data demonstrates the high variability of the CEF, due to its dependence on local conditions, and highlights the importance for further studies.

It would be beneficial to expand existing and build additional photometer networks, ensuring decent coverage of numerous cities and thereby building a basis for creating more CEFs to develop global databases, without the need for conducting on-site measurements. These databases could be used in further studies and aid in improving existing models, as scientists' understanding of the CEF would be advanced. Moreover, creating a global database could be used for guiding lighting policies and assessing environmental impacts.

Long-term studies of a cities NSB could be used to identify locations of significant and minimal light pollution, for guiding lighting policies and astronomical site selection, and areas with the highest need for implementing mitigation efforts.

As discussed in Sec. 2, there are several instruments for measuring and modelling light pollution. For this thesis solely SQM and TESS-W data was used. As mentioned in Sec. 3, 13 measurement locations were initially planned. Besides the additional measurements, taking images with a DSLR camera at certain measurement locations and analyzing the data using SQC software as described in Sec. 2.6, was planned. Furthermore, the data from this thesis could be used to improve simulations using the SkyGlow Simulator, which was considered as well. Due to time constraints, only the nine measurement locations and measurements using the SQM were possible, which leaves the opportunity for further studies using the aforementioned tools and expanding on this research.
Using these tools, or others mentioned in Sec. 2, offers the opportunity to amass more data for Vienna and Eisenstadt as well as several other cities of differing sizes and subsequently their CEFs.

As the results in Sec. 5.1.2 indicate, a decent coverage of the city is necessary to ensure smooth and accurate results. Therefore further studies into this topic may focus on finding a conversion factor between differently sized cities, to ensure sufficient coverage of a city is provided for the analysis. As was discussed in Sec. 5.1.2, the conversion of units, if decent coverage is not provided, may result in data-free areas, giving misleading results. This emphasizes the importance of providing a conversion factor to mitigate this possibility.
Meanwhile, the presented results for Eisenstadt and Vienna with their respective data points of four and nine/ten can be used as a reference when determining the amount of measurements to be taken in a differently sized city.

While light pollution studies receive increased focus over the years, researchers are still faced with complications and unanswered questions. This highlights the importance of

amateur and professional astronomers advancing research even further as well as research and conducting research becoming more widely accessible.
This thesis provides researchers with a simple, fast and accessible way of retrieving CEFs and subsequently build and expand global databases to advance research.

Bibliography

Miguel R. Alarcon, Marta Puig-Subirà, Miquel Serra-Ricart, Samuel Lemes-Perera, Manuel Mallorquín, and César López. Sg-was: A new wireless autonomous night sky brightness sensor. *Sensors*, 21(16), 2021. ISSN 1424-8220. doi: 10.3390/s21165590. URL https://www.mdpi.com/1424-8220/21/16/5590.

Martin Aubé and Miroslav Kocifaj. Using two light-pollution models to investigate artificial sky radiances at canary islands observatories. *Monthly Notices of the Royal Astronomical Society*, 422:819–830, 05 2012. doi: 10.1111/j.1365-2966.2012.20664.x.

Katarzyna Bobkowska, Pawel Burdziakowski, Pawel Tysiac, and Mariusz Pulas. An innovative new approach to light pollution measurement by drone. *Drones*, 8(9), 2024. ISSN 2504-446X. doi: 10.3390/drones8090504. URL https://www.mdpi.com/2504-446X/8/9/504.

Maria Carias, Shawn Fujioka, Jacob Phaneuf, Megan Potter, Ieva Vaiciunas, Lynn Wilder, Cassidy Wood, and Jacqueline Yu. Preserving the night sky: Monitoring light pollution affecting the central idaho dark sky reserve, 2021. URL https://www.ioes.ucla.edu/wp-content/uploads/2021/04/UCLA-IoES-Practicum-CIDSR-final-report-2021.pdf. last access: 27.10.2025, 19:12.

S. Cavazzani, P. Fiorentin, C. Bertolin, S. Ortolani, A. Bertolo, and R. Binotto. Novel algorithm for using the sky quality meter as a night cloud detector and aerosol concentration meter. *Atmospheric Pollution Research*, 16(10):102636, 2025. ISSN 1309-1042. doi: https://doi.org/10.1016/j.apr.2025.102636. URL https://www.sciencedirect.com/science/article/pii/S1309104225002387.

Pierantonio Cinzano. Night sky photometry with sky quality meter. *Environmental Science, Physics*, 9, 01 2005.

Pierantonio Cinzano. Report on sky quality meter, version l, 01 2007.

European Commission. Light pollution and climate change, a. URL https://ec.europa.eu/programmes/erasmus-plus/project-result-content/0eb54a4b-9b44-47a1-9acb-c56685ce80c5/Light%20Pollution%20%26%20Climate%20Change%20(Turkey).pdf. last access: 31.01.2025, 04:15.

European Commission. The influence of light pollution on climate change, b. URL https://ec.europa.eu/programmes/erasmus-plus/project-result-content/4c6206c4-2ff5-4850-9381-cf7f518c4a6c/light-%20climate%20presentation%20(Poland).pdf. last access: 31.01.2025, 04:15.

DarkSky International. Light pollution wastes energy and money, 2021. URL https://darksky.org/app/uploads/2021/01/Light-Pollution-Wastes-Energy-and-Money-English.pdf. last access: 23.10.2025 18:57.

DarkSky International. Light pollution wastes energy and damages the climate, 2023a. URL https://darksky.org/resources/what-is-light-pollution/effects/energy-climate/. last access: 23.10.2025 18:57.

DarkSky International. International dark sky places, 2023b. URL https://darksky.org/what-we-do/international-dark-sky-places/. last access: 22.10.2025, 16:35.

EELabs Project. Darksky data portal, n.d. URL https://www.data.eelabs.eu/. last access: 25.09.2025, 13:41.

Kathryn M Emmer, Kathryn L G Russart, William H Walker, Randy J Nelson, and A Courtney DeVries. Effects of light at night on laboratory animals and research outcomes. *Behav Neurosci*, 132(4):302–314, June 2018.

Borja Fernandez-Ruiz, Miquel Serra-Ricart, Miguel R. Alarcon, Samuel Lemes-Perera, Idafen Santana-Perez, and Juan Ruiz-Alzola. Calibrating nighttime satellite imagery with red photometer networks. *Remote Sensing*, 15(17), 2023. ISSN 2072-4292. doi: 10.3390/rs15174189. URL https://www.mdpi.com/2072-4292/15/17/4189.

Edna Guk and Noam Levin. Analyzing spatial variability in night-time lights using a high spatial resolution color jilin-1 image – jerusalem as a case study. *ISPRS Journal of Photogrammetry and Remote Sensing*, 163:121–136, 2020. ISSN 0924-2716. doi: https://doi.org/10.1016/j.isprsjprs.2020.02.016. URL https://www.sciencedirect.com/science/article/pii/S0924271620300599.

Andreas Hänel, Lambros Doulos, Sibylle Schroer, Catalin Gălăţanu, and Frangiskos Topalis. Sustainable outdoor lighting for reducing energy and light waste. In *Sustainable outdoor lighting for reducing energy and light waste*, 03 2016.

Johnni Hansen and Christina F Lassen. Nested case–control study of night shift work and breast cancer risk among women in the danish military. *Occupational and Environmental Medicine*, 69(8):551–556, 2012. ISSN 1351-0711. doi: 10.1136/oemed-2011-100240. URL https://oem.bmj.com/content/69/8/551.

Najmaldin Hassan. Light pollution and its effects on human health and the environment: A review. *Asian Journal of Environment & Ecology*, 23:96–108, 10 2024. doi: 10.9734/ajee/2024/v23i10613.

Susan Hurley, Debbie Goldberg, David Nelson, Andrew Hertz, Pamela L Horn-Ross, Leslie Bernstein, and Peggy Reynolds. Light at night and breast cancer risk among california teachers. *Epidemiology*, 25(5):697–706, September 2014.

Daniel Jiménez, Laura Neira Arenas, Erwin Hernando Hernández Rincón, María José García Céspedes, and Claudia Liliana Jaimes Peñuela. Luminous threats: The health impacts of artificial nighttime light on metabolic and mental health: A scoping review. *Wellbeing, Space and Society*, 8:100260, 2025. ISSN 2666-5581. doi: https://doi.org/10.1016/j.wss.2025.100260. URL https://www.sciencedirect.com/science/article/pii/S2666558125000260.

Biren B. Kamdar, Ana I. Tergas, Farrah J. Mateen, Neil H. Bhayani, and Jiwon Oh. Night-shift work and risk of breast cancer: a systematic review and meta-analysis. *Breast Cancer Research and Treatment*, 138(1):291–301, Feb 2013. ISSN 1573-7217. doi: 10.1007/s10549-013-2433-1. URL https://doi.org/10.1007/s10549-013-2433-1.

Bruce R. Kinzey, Tess E. Perrin, Naomi J. Miller, Miroslav Kocifaj, Martin Aube, and Hector A. Lamphar. An investigation of led street lighting's impact on sky glow. Technical report, Pacific Northwest National Laboratory (PNNL), Richland, WA (US), 04 2017. URL https://www.osti.gov/biblio/1418092.

Itai Kloog, Abraham Haim, Richard Stevens, and Boris Portnov. Global co-distribution of light at night (lan) and cancers of prostate, colon, and lung in men. *Chronobiology international*, 26:108–25, 02 2009. doi: 10.1080/07420520802694020.

M. Kocifaj, S. Wallner, and C. A. Gueymard. Detailed assessment of multiple-scattering effects on night-sky brightness modeling in turbid environments: The impact of truncation and convergence errors. *Journal of Geophysical Research: Atmospheres*, 129 (1):e2023JD039804, 2024. doi: https://doi.org/10.1029/2023JD039804. URL https://agupubs.onlinelibrary.wiley.com/doi/abs/10.1029/2023JD039804.

Miroslav Kocifaj. Light-pollution model for cloudy and cloudless night skies with ground-based light sources. *Appl. Opt.*, 46(15):3013–3022, May 2007. doi: 10.1364/AO.46.003013. URL https://opg.optica.org/ao/abstract.cfm?URI=ao-46-15-3013.

Miroslav Kocifaj. Retrieval of angular emission function from whole-city light sources using night-sky brightness measurements. *Optica*, 4:255–262, 02 2017. doi: 10.1364/OPTICA.4.000255.

Miroslav Kocifaj. Towards a comprehensive city emission function (ccef). *Journal of Quantitative Spectroscopy and Radiative Transfer*, 205:253–266, 2018. ISSN 0022-4073. doi: https://doi.org/10.1016/j.jqsrt.2017.10.006. URL https://www.sciencedirect.com/science/article/pii/S0022407317304776.

Miroslav Kocifaj and Héctor Antonio Solano Lamphar. Angular emission function of a city and skyglow modeling: A critical perspective. *Publications of the Astronomical Society of the Pacific*, 128(970):124001, nov 2016. doi: 10.1088/1538-3873/128/970/124001. URL https://doi.org/10.1088/1538-3873/128/970/124001.

Miroslav Kocifaj, Héctor Antonio Solano-Lamphar, and Gorden Videen. Night-sky radiometry can revolutionize the characterization of light-pollution sources globally.

Proceedings of the National Academy of Sciences, 116(16):7712–7717, 2019. doi: 10.1073/pnas.1900153116. URL `https://www.pnas.org/doi/abs/10.1073/pnas.1900153116`.

Christopher C. M. Kyba, Yiğit Öner Altıntaş, Constance E. Walker, and Mark Newhouse. Citizen scientists report global rapid reductions in the visibility of stars from 2011 to 2022. *Science*, 379(6629):265–268, 2023. doi: 10.1126/science.abq7781. URL `https://www.science.org/doi/abs/10.1126/science.abq7781`.

Jinjin Li, Linlin Lu, and Xi Li. Estimating city emission function with viirs/dnb data and vegetation phenology. *IEEE Journal of Selected Topics in Applied Earth Observations and Remote Sensing*, PP:1–11, 01 2025. doi: 10.1109/JSTARS.2025.3610127.

Hector Linares Arroyo, Eduard Masana, Salvador Ribas, Manuel Garcia, Francesca Figueras, and Martin Aubé. Modelling the night sky brightness and light pollution sources of montsec protected area. *Journal of Quantitative Spectroscopy and Radiative Transfer*, 217, 05 2018. doi: 10.1016/j.jqsrt.2018.05.037.

Hector Linares Arroyo, Angela Abascal, Tobias Degen, Martin Aubé, Brian R. Espey, Geza Gyuk, Franz Hölker, Andreas Jechow, Monika Kuffer, Alejandro Sánchez de Miguel, Alexandre Simoneau, Ken Walczak, and Christopher C. M. Kyba. Monitoring, trends and impacts of light pollution. *Nature Reviews Earth & Environment*, 5(6): 417–430, Jun 2024. ISSN 2662-138X. doi: 10.1038/s43017-024-00555-9. URL `https://doi.org/10.1038/s43017-024-00555-9`.

Travis Longcore and Catherine Rich. Ecological light pollution. *Frontiers in Ecology and the Environment*, 2:191–198, 05 2004. doi: 10.1890/1540-9295(2004)002[0191:ELP]2.0.CO;2.

Christian B. Luginbuhl, Paul A. Boley, and Donald R. Davis. The impact of light source spectral power distribution on sky glow. *Journal of Quantitative Spectroscopy and Radiative Transfer*, 139:21–26, 2014. ISSN 0022-4073. doi: https://doi.org/10.1016/j.jqsrt.2013.12.004. URL `https://www.sciencedirect.com/science/article/pii/S0022407313004792`. Light pollution: Theory, modeling, and measurements.

Vítor Manteigas, Marina Almeida-Silva, and Diana Mendes. Light pollution and energy efficiency: a case study of the village of vialonga, 05 2012.

Marcellino Melika, Anish Javvadi, Cian Chien, Caitlyn Ng, Stuti Hegde, Sanjith Sowrirajan, and Rushil Kukreja. The impact of light pollution on biodiversity: Disrupting nocturnal ecosystems, 01 2025.

Choul Yong Park. Night light pollution and ocular fatigue. *J Korean Med Sci*, 33(38): e257, September 2018.

Antonia M. Varela Perez. The increasing effects of light pollution on professional and amateur astronomy. *Science*, 380(6650):1136–1140, 2023. doi: 10.1126/science.adg0269. URL `https://www.science.org/doi/abs/10.1126/science.adg0269`.

Eero Pukkala, Matti Ojamo, Sirkka-Liisa Rudanko, Richard G. Stevens, and Pia K. Verkasalo. Does incidence of breast cancer and prostate cancer decrease with increasing degree of visual impairment. *Cancer Causes & Control*, 17(4):573–576, May 2006. ISSN 1573-7225. doi: 10.1007/s10552-005-9005-6. URL https://doi.org/10.1007/s10552-005-9005-6.

Thomas Raap, Rianne Pinxten, and Marcel Eens. Light pollution disrupts sleep in free-living animals. *Scientific Reports*, 09 2015. doi: 10.1038/srep13557.

Kathryn L G Russart and Randy J Nelson. Artificial light at night alters behavior in laboratory and wild animals. *J Exp Zool A Ecol Integr Physiol*, 329(8-9):401–408, May 2018.

Eva S. Schernhammer, Candyce H. Kroenke, Francine Laden, and Susan E. Hankinson. Night work and risk of breast cancer. *Epidemiology*, 17(1):108–111, 2006. ISSN 10443983. URL http://www.jstor.org/stable/20486169.

Ariel Simons, Xiaozhe Yin, and Travis Longcore. High correlation but high scale-dependent variance between satellite measured night lights and terrestrial exposure. *Environmental Research Communications*, 2, 02 2020. doi: 10.1088/2515-7620/ab7501.

Héctor Antonio Solano Lamphar. The emission function of ground-based light sources: State of the art and research challenges. *Journal of Quantitative Spectroscopy and Radiative Transfer*, 211:35–43, 2018. ISSN 0022-4073. doi: https://doi.org/10.1016/j.jqsrt.2018.02.034. URL https://www.sciencedirect.com/science/article/pii/S0022407317308750.

Alejandro Sánchez de Miguel, Jaime Zamorano, Martin Aubé, Jonathan Bennie, Jesús Gallego, Francisco Ocaña, Donald R. Pettit, William L. Stefanov, and Kevin J. Gaston. Colour remote sensing of the impact of artificial light at night (ii): Calibration of dslr-based images from the international space station. *Remote Sensing of Environment*, 264:112611, 2021. ISSN 0034-4257. doi: https://doi.org/10.1016/j.rse.2021.112611. URL https://www.sciencedirect.com/science/article/pii/S003442572100331X.

Manuela Tondelli, Tommaso Filippini, Giulia Vinceti, Najara Iacovino, Teresa Urbano, Sofia Costanzini, Francesca Despini, Claudia De Luca, Simona Tondelli, Marco Vinceti, Annalisa Chiari, and Giovanna Zamboni. Outdoor light at night and neuropsychiatric symptoms in dementia. *GeroScience*, Jul 2025. ISSN 2509-2723. doi: 10.1007/s11357-025-01745-z. URL https://doi.org/10.1007/s11357-025-01745-z.

Unihedron. Dark sky database, n.d.a. URL https://www.unihedron.com/projects/darksky/database/. last access: 13.10.2025, 17:10.

Unihedron. Dark sky project, n.d.b. URL https://www.unihedron.com/projects/darksky/. last access: 13.10.2025, 17:05.

Stefan Wallner. Usage of vertical fisheye-images to quantify urban light pollution on small scales and the impact of led conversion. *Journal of Imaging*, 5(11), 2019. ISSN 2313-433X. doi: 10.3390/jimaging5110086. URL `https://www.mdpi.com/2313-433X/5/11/86`.

Stefan Wallner and Miroslav Kocifaj. Aerosol impact on light pollution in cities and their environment. *Journal of Environmental Management*, 335:117534, 2023. ISSN 0301-4797. doi: https://doi.org/10.1016/j.jenvman.2023.117534. URL `https://www.sciencedirect.com/science/article/pii/S0301479723003225`.

Marcin Wesołowski. The increase in the surface brightness of the night sky and its importance in visual astronomical observations. *Scientific Reports*, 13(1):17091, Oct 2023. ISSN 2045-2322. doi: 10.1038/s41598-023-44423-w. URL `https://doi.org/10.1038/s41598-023-44423-w`.

Marcin Wesołowski. Impact of light pollution on the visibility of astronomical objects in medium-sized cities in central europe on the example of the city of rzeszów, poland. *Journal of Astrophysics and Astronomy*, 40, 06 2019. doi: 10.1007/s12036-019-9586-1.

Blair Witherington and Erik Martin. Understanding, assessing, and resolving light-pollution problems on sea turtle nesting beaches. *Fl. Mar. Res. Inst. Tech. Rep. TR-2*, 01 2003.

Wiktoria Wojciechowska, Omar Hahad, Andreas Daiber, and Marek Rajzer. Night light pollution and cardiovascular disease. *Polish Heart Journal (Kardiologia Polska)*, 83 (7-8):801 – 807, 2025. ISSN 1897-4279. doi: 10.33963/v.phj.106586. URL `https://journals.viamedica.pl/polish_heart_journal/article/view/106586`.

Le Yang, Quan Wang, He Zheng, Yiqing Wang, Zhigang Miao, Hao Li, and Yi Yang. Association between outdoor artificial light at night, circadian health, and LDL-C in intracranial artery atherosclerotic stenosis. *Clin Epigenetics*, 17(1):132, July 2025.

Jaime Zamorano, Cristóbal García, Carlos Eugenio Tapia Ayuga, Alejandro Sanchez de Miguel, Sergio Pascual, and Jesús Gallego. Stars4all night sky brightness photometer. *International Journal of Sustainable Lighting*, 18:49–54, 06 2017. doi: 10.26607/ijsl.v18i0.21.

Acronyms

ALAN Artificial Light At Night. 1–3, 5, 16, 18

AOD Aerosol Optical Depth. 6, 9, 13, 14

ASY Asymmetry Parameter. 9, 11, 14

CCDs Charge-Coupled Devices. 4

CCEF Comprehensive City Emission Function. 8–10

CCT Correlated Color Temperature. xi, 16, 17, 19

CEF City Emission Function. iii, v, 6–10, 23, 28, 46, 48, 53, 59, 61–63

CMOS Complementary Metal-Oxide-Semiconductor. 4

DarkSky Dark Sky International. 3

DMS Degree, Minute and Second. ix, 23, 24, 28, 50, 51

DOA Department Of Astrophysics, Univ. Vienna. ix, 28, 29, 45, 46

DSLR Digital Single-Lens Reflex. 15, 16, 62

EOS Earth Observing System. 15

EW East-West. ix, 25–28, 50

GEF Garstang Emission Function. 7–9, 11

HPS High Pressure Sodium. 5, 6, 8, 18, 19, 21

IAU International Astronomical Union. 4

ISS International Space Station. 15

LED Light Emitting Diode. 4, 6, 8, 15, 21

NOAA National Oceanic and Atmospheric Administration. 15

NS North-South. ix, 23, 25–28, 50

NSB Night Sky Brightness. iii, xii, 6, 14, 15, 18, 19, 23, 37, 41, 43, 46, 48, 52, 53, 59–62

RTE Radiative Transfer Equation. 9

SG-WAS Sky-Glow Wireless Autonomous Sensor. xi, 15, 16, 18, 20

SI International System of Units. 48

SQC Sky Quality Camera. xi, 16–18, 62

SQM Sky Quality Meter. iii, v, ix, 4, 15, 16, 18–23, 28, 29, 43–46, 48, 61, 62

SSA Single Scattering Albedo. 9, 11

Suomi NPP Suomi National Polar-orbiting Partnership. 14

TESS-W Telescope Encoder and Sky Sensor WIFI. iii, v, xi, 15, 18–20, 43, 61, 62

VIIRS DNB Day-Night Band Of Visible Infrared Imaging Radiometer Suite. 14, 15, 18, 19

A. Appendix

Table A.1.: Data collected from TESS photometers in Eisenstadt, with timestamps depicting when measurements were taken during the night of November 29th 2024.

29.11.2024							
941		943		944		1120	
2024-11-29 00:56:08	19.61	2024-11-29 00:54:03	19.33	2024-11-29 00:55:14	20.16	2024-11-29 00:55:13	19.61
2024-11-29 00:57:08	19.52	2024-11-29 00:55:04	19.33	2024-11-29 00:56:14	20.20	2024-11-29 00:56:13	19.58
2024-11-29 00:58:08	19.73	2024-11-29 00:56:04	19.36	2024-11-29 00:57:14	20.26	2024-11-29 00:57:14	19.55
2024-11-29 00:59:08	19.77	2024-11-29 00:57:04	19.35	2024-11-29 00:58:14	20.32	2024-11-29 00:58:14	19.51
2024-11-29 01:00:08	19.85	2024-11-29 00:58:04	19.38	2024-11-29 00:59:15	20.36	2024-11-29 00:59:14	19.50
2024-11-29 01:01:08	19.85	2024-11-29 00:59:04	19.40	2024-11-29 01:00:15	20.38	2024-11-29 01:00:14	19.55
2024-11-29 01:02:08	19.84	2024-11-29 01:00:04	19.43	2024-11-29 01:01:15	20.38	2024-11-29 01:01:14	19.66
2024-11-29 01:03:08	19.84	2024-11-29 01:01:04	19.43	2024-11-29 01:02:15	20.36	2024-11-29 01:02:14	19.78
2024-11-29 01:04:08	19.83	2024-11-29 01:02:05	19.43	2024-11-29 01:03:15	20.33	2024-11-29 01:03:14	19.85
2024-11-29 01:05:09	19.75	2024-11-29 01:03:05	19.43	2024-11-29 01:04:15	20.33	2024-11-29 01:04:15	19.88
2024-11-29 01:55:14	19.26	2024-11-29 01:54:11	19.05	2024-11-29 01:55:20	19.89	2024-11-29 01:55:24	18.79
2024-11-29 01:56:14	19.21	2024-11-29 01:55:12	18.91	2024-11-29 01:56:21	19.79	2024-11-29 01:56:24	18.89
2024-11-29 01:57:14	19.10	2024-11-29 01:56:12	18.86	2024-11-29 01:57:21	19.71	2024-11-29 01:57:24	18.87
2024-11-29 01:58:15	18.97	2024-11-29 01:57:12	18.87	2024-11-29 01:58:21	19.50	2024-11-29 01:58:24	18.87
2024-11-29 01:59:15	18.82	2024-11-29 01:58:12	18.77	2024-11-29 01:59:21	19.38	2024-11-29 01:59:24	18.85
2024-11-29 02:00:15	18.81	2024-11-29 01:59:12	18.70	2024-11-29 02:00:21	19.28	2024-11-29 02:00:24	18.76
2024-11-29 02:01:15	18.84	2024-11-29 02:00:12	18.62	2024-11-29 02:01:21	19.25	2024-11-29 02:01:25	18.70
2024-11-29 02:02:15	18.96	2024-11-29 02:01:13	18.56	2024-11-29 02:02:21	19.21	2024-11-29 02:02:25	18.66
2024-11-29 02:03:15	18.92	2024-11-29 02:02:13	18.55	2024-11-29 02:03:21	19.26	2024-11-29 02:03:25	18.59
2024-11-29 02:04:16	18.86	2024-11-29 02:03:13	18.57	2024-11-29 02:04:21	19.38	2024-11-29 02:04:25	18.49
2024-11-29 02:55:23	18.77	2024-11-29 02:55:21	18.70	2024-11-29 02:55:28	19.44	2024-11-29 02:55:32	19.14
2024-11-29 02:56:23	18.81	2024-11-29 02:56:21	18.72	2024-11-29 02:56:28	19.58	2024-11-29 02:56:33	19.16
2024-11-29 02:57:23	19.10	2024-11-29 02:57:21	18.87	2024-11-29 02:57:28	19.65	2024-11-29 02:57:33	19.21
2024-11-29 02:58:23	19.47	2024-11-29 02:58:21	18.97	2024-11-29 02:58:28	19.28	2024-11-29 02:58:33	18.98
2024-11-29 02:59:23	19.48	2024-11-29 02:59:21	18.87	2024-11-29 02:59:28	18.98	2024-11-29 02:59:33	19.10
2024-11-29 03:00:23	19.29	2024-11-29 03:00:21	18.77	2024-11-29 03:00:29	19.02	2024-11-29 03:00:34	19.19
2024-11-29 03:01:23	19.11	2024-11-29 03:01:22	18.67	2024-11-29 03:01:29	19.07	2024-11-29 03:01:34	19.07
2024-11-29 03:02:23	19.16	2024-11-29 03:02:22	18.60	2024-11-29 03:02:29	19.09	2024-11-29 03:02:34	18.93
2024-11-29 03:03:23	19.15	2024-11-29 03:03:22	18.67	2024-11-29 03:03:29	19.13	2024-11-29 03:03:34	18.83
2024-11-29 03:04:23	19.02	2024-11-29 03:04:22	18.82	2024-11-29 03:04:29	19.35	2024-11-29 03:04:34	18.73
2024-11-29 03:55:30	19.80	2024-11-29 03:55:29	19.55	2024-11-29 03:55:36	20.74	2024-11-29 03:55:43	20.04
2024-11-29 03:56:30	19.80	2024-11-29 03:56:29	19.58	2024-11-29 03:56:36	20.73	2024-11-29 03:56:43	20.16
2024-11-29 03:57:30	19.43	2024-11-29 03:57:29	19.59	2024-11-29 03:57:36	20.71	2024-11-29 03:57:43	20.24
2024-11-29 03:58:30	19.70	2024-11-29 03:58:29	19.58	2024-11-29 03:58:36	20.65	2024-11-29 03:58:44	20.28
2024-11-29 03:59:30	19.94	2024-11-29 03:59:29	19.52	2024-11-29 03:59:37	20.36	2024-11-29 03:59:44	20.29
2024-11-29 04:00:30	20.01	2024-11-29 04:00:29	19.54	2024-11-29 04:00:37	19.75	2024-11-29 04:00:44	20.26
2024-11-29 04:01:30	19.83	2024-11-29 04:01:29	19.45	2024-11-29 04:01:37	18.95	2024-11-29 04:01:44	20.22
2024-11-29 04:02:30	18.92	2024-11-29 04:02:29	19.13	2024-11-29 04:02:37	18.89	2024-11-29 04:02:45	20.15
2024-11-29 04:03:30	18.63	2024-11-29 04:03:29	18.80	2024-11-29 04:03:37	18.99	2024-11-29 04:03:45	20.07
2024-11-29 04:04:31	18.90	2024-11-29 04:04:30	18.39	2024-11-29 04:04:37	18.73	2024-11-29 04:04:45	19.71

Table A.2.: Data collected from TESS photometers in Eisenstadt, with timestamps depicting when measurements were taken during the night of November 30th 2024.

30.11.2024							
941		943		944		1120	
2024-11-30 00:55:16	19.18	2024-11-30 00:55:33	18.88	2024-11-30 00:54:51	20.51	2024-11-30 00:54:58	19.76
2024-11-30 00:56:16	19.21	2024-11-30 00:56:33	19.03	2024-11-30 00:55:51	20.64	2024-11-30 00:55:58	19.70
2024-11-30 00:57:17	19.27	2024-11-30 00:57:34	19.23	2024-11-30 00:56:51	20.71	2024-11-30 00:56:59	19.80
2024-11-30 00:58:17	19.39	2024-11-30 00:58:34	19.39	2024-11-30 00:57:51	20.74	2024-11-30 00:57:59	19.84
2024-11-30 00:59:17	19.58	2024-11-30 00:59:34	19.53	2024-11-30 00:58:51	20.76	2024-11-30 00:58:59	20.07
2024-11-30 01:00:17	19.78	2024-11-30 01:00:34	19.60	2024-11-30 00:59:51	20.77	2024-11-30 00:59:59	20.21
2024-11-30 01:01:17	19.90	2024-11-30 01:01:34	19.63	2024-11-30 01:00:51	20.77	2024-11-30 01:00:59	20.28
2024-11-30 01:02:17	19.98	2024-11-30 01:02:34	19.64	2024-11-30 01:01:51	20.77	2024-11-30 01:01:59	20.29
2024-11-30 01:03:17	20.04	2024-11-30 01:03:34	19.64	2024-11-30 01:02:51	20.78	2024-11-30 01:02:59	20.29
2024-11-30 01:04:17	20.15	2024-11-30 01:04:34	19.65	2024-11-30 01:03:51	20.78	2024-11-30 01:03:59	20.30
2024-11-30 01:54:40	20.47	2024-11-30 01:54:38	19.70	2024-11-30 01:55:14	20.86	2024-11-30 01:54:03	20.40
2024-11-30 01:55:40	20.48	2024-11-30 01:55:38	19.70	2024-11-30 01:56:15	20.87	2024-11-30 01:55:03	20.38
2024-11-30 01:56:40	20.48	2024-11-30 01:56:38	19.70	2024-11-30 01:57:15	20.87	2024-11-30 01:56:03	20.35
2024-11-30 01:57:40	20.48	2024-11-30 01:57:38	19.69	2024-11-30 01:58:15	20.87	2024-11-30 01:57:03	20.29
2024-11-30 01:58:40	20.46	2024-11-30 01:58:38	19.69	2024-11-30 01:59:15	20.86	2024-11-30 01:58:03	20.14
2024-11-30 01:59:41	20.45	2024-11-30 01:59:39	19.69	2024-11-30 02:00:15	20.86	2024-11-30 01:59:03	20.10
2024-11-30 02:00:41	20.45	2024-11-30 02:00:38	19.69	2024-11-30 02:01:15	20.87	2024-11-30 02:00:03	20.13
2024-11-30 02:01:41	20.46	2024-11-30 02:01:39	19.69	2024-11-30 02:02:15	20.86	2024-11-30 02:01:03	20.09
2024-11-30 02:02:41	20.45	2024-11-30 02:02:38	19.69	2024-11-30 02:03:15	20.86	2024-11-30 02:02:03	20.16
2024-11-30 02:03:41	20.45	2024-11-30 02:03:39	19.68	2024-11-30 02:04:15	20.86	2024-11-30 02:03:03	20.22
2024-11-30 02:56:04	20.47	2024-11-30 02:55:51	19.55	2024-11-30 02:55:19	20.37	2024-11-30 02:55:08	19.05
2024-11-30 02:57:04	20.39	2024-11-30 02:56:51	19.59	2024-11-30 02:56:19	20.41	2024-11-30 02:56:08	18.85
2024-11-30 02:58:04	20.39	2024-11-30 02:57:51	19.61	2024-11-30 02:57:19	20.44	2024-11-30 02:57:08	18.78
2024-11-30 02:59:04	20.36	2024-11-30 02:58:51	19.61	2024-11-30 02:58:19	20.50	2024-11-30 02:58:08	18.88
2024-11-30 03:00:04	20.33	2024-11-30 02:59:51	19.59	2024-11-30 02:59:20	20.60	2024-11-30 02:59:08	19.11
2024-11-30 03:01:04	20.41	2024-11-30 03:00:51	19.59	2024-11-30 03:00:20	20.69	2024-11-30 03:00:08	19.24
2024-11-30 03:02:04	20.48	2024-11-30 03:01:51	19.58	2024-11-30 03:01:20	20.71	2024-11-30 03:01:08	19.23
2024-11-30 03:03:04	20.47	2024-11-30 03:02:52	19.55	2024-11-30 03:02:20	20.70	2024-11-30 03:02:08	19.25
2024-11-30 03:04:04	20.47	2024-11-30 03:03:52	19.52	2024-11-30 03:03:20	20.70	2024-11-30 03:03:08	19.18
2024-11-30 03:05:04	20.45	2024-11-30 03:04:52	19.48	2024-11-30 03:04:20	20.64	2024-11-30 03:04:08	19.01
2024-11-30 03:54:09	20.32	2024-11-30 03:55:58	19.12	2024-11-30 03:54:25	19.75	2024-11-30 03:55:16	18.13
2024-11-30 03:55:09	20.29	2024-11-30 03:56:58	19.11	2024-11-30 03:55:25	19.75	2024-11-30 03:56:16	18.17
2024-11-30 03:56:09	20.23	2024-11-30 03:57:58	19.07	2024-11-30 03:56:25	19.83	2024-11-30 03:57:16	18.16
2024-11-30 03:57:09	20.15	2024-11-30 03:58:58	19.01	2024-11-30 03:57:25	20.00	2024-11-30 03:58:17	18.13
2024-11-30 03:58:09	20.19	2024-11-30 03:59:58	19.00	2024-11-30 03:58:25	20.06	2024-11-30 03:59:17	18.13
2024-11-30 03:59:09	20.20	2024-11-30 04:00:58	18.96	2024-11-30 03:59:25	20.09	2024-11-30 04:00:17	18.10
2024-11-30 04:00:09	20.23	2024-11-30 04:01:58	18.91	2024-11-30 04:00:25	20.08	2024-11-30 04:01:17	18.06
2024-11-30 04:01:09	20.26	2024-11-30 04:02:58	19.01	2024-11-30 04:01:26	20.08	2024-11-30 04:02:17	17.97
2024-11-30 04:02:09	20.26	2024-11-30 04:03:58	19.00	2024-11-30 04:02:26	20.17	2024-11-30 04:03:17	17.99
2024-11-30 04:03:09	20.26	2024-11-30 04:04:59	18.96	2024-11-30 04:03:26	20.18	2024-11-30 04:04:18	18.00

Table A.3.: Data collected from TESS photometers in Eisenstadt, with timestamps depicting when measurements were taken during the night of December 1st 2024.

01.12.2024							
941		943		944		1120	
2024-12-01 00:54:04	20.28	2024-12-01 00:55:22	19.53	2024-12-01 00:54:37	20.62	2024-12-01 00:55:49	19.95
2024-12-01 00:55:04	20.28	2024-12-01 00:56:22	19.52	2024-12-01 00:55:37	20.62	2024-12-01 00:56:49	19.96
2024-12-01 00:56:04	20.29	2024-12-01 00:57:22	19.52	2024-12-01 00:56:37	20.62	2024-12-01 00:57:49	19.96
2024-12-01 00:57:04	20.28	2024-12-01 00:58:22	19.53	2024-12-01 00:57:37	20.62	2024-12-01 00:58:49	19.96
2024-12-01 00:58:04	20.29	2024-12-01 00:59:22	19.52	2024-12-01 00:58:37	20.62	2024-12-01 00:59:49	19.96
2024-12-01 00:59:04	20.29	2024-12-01 01:00:22	19.53	2024-12-01 00:59:37	20.62	2024-12-01 01:00:49	19.97
2024-12-01 01:00:05	20.30	2024-12-01 01:01:22	19.53	2024-12-01 01:00:37	20.62	2024-12-01 01:01:49	19.97
2024-12-01 01:01:05	20.30	2024-12-01 01:02:22	19.54	2024-12-01 01:01:38	20.62	2024-12-01 01:02:50	19.96
2024-12-01 01:02:05	20.29	2024-12-01 01:03:23	19.54	2024-12-01 01:02:38	20.62	2024-12-01 01:03:50	19.96
2024-12-01 01:03:05	20.30	2024-12-01 01:04:23	19.54	2024-12-01 01:03:38	20.62	2024-12-01 01:04:50	19.95
2024-12-01 01:54:09	20.30	2024-12-01 01:55:29	19.52	2024-12-01 01:55:42	20.60	2024-12-01 01:55:53	19.95
2024-12-01 01:55:09	20.30	2024-12-01 01:56:36	19.51	2024-12-01 01:56:42	20.59	2024-12-01 01:56:54	19.95
2024-12-01 01:56:09	20.29	2024-12-01 01:57:36	19.52	2024-12-01 01:57:42	20.60	2024-12-01 01:57:54	19.95
2024-12-01 01:57:09	20.29	2024-12-01 01:58:36	19.52	2024-12-01 01:58:42	20.59	2024-12-01 01:58:54	19.95
2024-12-01 01:58:09	20.29	2024-12-01 01:59:36	19.53	2024-12-01 01:59:42	20.59	2024-12-01 01:59:54	19.95
2024-12-01 01:59:09	20.30	2024-12-01 02:00:36	19.52	2024-12-01 02:00:42	20.60	2024-12-01 02:00:54	19.95
2024-12-01 02:00:09	20.30	2024-12-01 02:01:36	19.52	2024-12-01 02:01:42	20.60	2024-12-01 02:01:54	19.95
2024-12-01 02:01:09	20.30	2024-12-01 02:02:36	19.51	2024-12-01 02:02:42	20.60	2024-12-01 02:02:54	19.95
2024-12-01 02:02:09	20.29	2024-12-01 02:03:36	19.50	2024-12-01 02:03:42	20.59	2024-12-01 02:03:54	19.95
2024-12-01 02:03:09	20.29	2024-12-01 02:04:36	19.49	2024-12-01 02:04:42	20.56	2024-12-01 02:04:54	19.95
2024-12-01 02:54:13	20.31	2024-12-01 02:55:43	19.53	2024-12-01 02:55:46	20.64	2024-12-01 02:54:58	19.97
2024-12-01 02:55:13	20.31	2024-12-01 02:56:43	19.53	2024-12-01 02:56:47	20.64	2024-12-01 02:55:58	19.97
2024-12-01 02:56:13	20.30	2024-12-01 02:57:43	19.52	2024-12-01 02:57:47	20.64	2024-12-01 02:56:58	19.97
2024-12-01 02:57:13	20.30	2024-12-01 02:58:43	19.53	2024-12-01 02:58:47	20.63	2024-12-01 02:57:58	19.95
2024-12-01 02:58:13	20.30	2024-12-01 02:59:43	19.52	2024-12-01 02:59:47	20.63	2024-12-01 02:58:58	19.96
2024-12-01 02:59:13	20.30	2024-12-01 03:00:43	19.52	2024-12-01 03:00:47	20.63	2024-12-01 02:59:58	19.95
2024-12-01 03:00:14	20.29	2024-12-01 03:01:44	19.53	2024-12-01 03:01:47	20.63	2024-12-01 03:00:59	19.95
2024-12-01 03:01:14	20.29	2024-12-01 03:02:44	19.53	2024-12-01 03:02:47	20.63	2024-12-01 03:01:59	19.96
2024-12-01 03:02:14	20.29	2024-12-01 03:03:44	19.51	2024-12-01 03:03:47	20.63	2024-12-01 03:02:59	19.96
2024-12-01 03:03:14	20.28	2024-12-01 03:04:44	19.50	2024-12-01 03:04:47	20.63	2024-12-01 03:03:59	19.96
2024-12-01 03:55:18	20.24	2024-12-01 03:55:49	19.48	2024-12-01 03:55:52	20.57	2024-12-01 03:54:03	19.92
2024-12-01 03:56:18	20.24	2024-12-01 03:56:50	19.46	2024-12-01 03:56:52	20.53	2024-12-01 03:55:03	19.92
2024-12-01 03:57:18	20.25	2024-12-01 03:57:50	19.47	2024-12-01 03:57:52	20.55	2024-12-01 03:56:03	19.93
2024-12-01 03:58:18	20.25	2024-12-01 03:58:50	19.46	2024-12-01 03:58:52	20.55	2024-12-01 03:57:03	19.93
2024-12-01 03:59:18	20.25	2024-12-01 03:59:50	19.48	2024-12-01 03:59:52	20.55	2024-12-01 03:58:03	19.94
2024-12-01 04:00:18	20.25	2024-12-01 04:00:50	19.47	2024-12-01 04:00:52	20.58	2024-12-01 03:59:03	19.93
2024-12-01 04:01:18	20.24	2024-12-01 04:01:50	19.46	2024-12-01 04:01:52	20.57	2024-12-01 04:00:03	19.93
2024-12-01 04:02:18	20.25	2024-12-01 04:02:50	19.46	2024-12-01 04:02:52	20.57	2024-12-01 04:01:03	19.91
2024-12-01 04:03:19	20.24	2024-12-01 04:03:50	19.46	2024-12-01 04:03:52	20.57	2024-12-01 04:02:03	19.89
2024-12-01 04:04:19	20.24	2024-12-01 04:04:50	19.47	2024-12-01 04:04:52	20.57	2024-12-01 04:03:03	19.88

Table A.4.: Data collected from TESS photometers in Eisenstadt, with timestamps depicting when measurements were taken during the night of December 2nd 2024.

02.12.2024							
941		943		944		1120	
2024-12-02 00:55:09	20.37	2024-12-02 00:54:00	19.62	2024-12-02 00:54:02	20.76	2024-12-02 00:54:24	20.36
2024-12-02 00:56:09	20.36	2024-12-02 00:55:00	19.61	2024-12-02 00:55:02	20.76	2024-12-02 00:55:24	20.36
2024-12-02 00:57:09	20.36	2024-12-02 00:56:00	19.61	2024-12-02 00:56:02	20.76	2024-12-02 00:56:24	20.36
2024-12-02 00:58:09	20.35	2024-12-02 00:57:00	19.61	2024-12-02 00:57:02	20.76	2024-12-02 00:57:25	20.36
2024-12-02 00:59:09	20.34	2024-12-02 00:58:00	19.60	2024-12-02 00:58:02	20.76	2024-12-02 00:58:25	20.36
2024-12-02 01:00:09	20.34	2024-12-02 00:59:00	19.59	2024-12-02 00:59:03	20.76	2024-12-02 00:59:25	20.36
2024-12-02 01:01:09	20.33	2024-12-02 01:00:00	19.59	2024-12-02 01:00:03	20.75	2024-12-02 01:00:25	20.36
2024-12-02 01:02:09	20.33	2024-12-02 01:01:01	19.59	2024-12-02 01:01:03	20.74	2024-12-02 01:01:25	20.35
2024-12-02 01:03:09	20.33	2024-12-02 01:02:01	19.58	2024-12-02 01:02:03	20.73	2024-12-02 01:02:25	20.36
2024-12-02 01:04:09	20.33	2024-12-02 01:03:01	19.57	2024-12-02 01:03:03	20.72	2024-12-02 01:03:25	20.36
2024-12-02 01:54:25	19.85	2024-12-02 01:54:06	19.40	2024-12-02 01:55:07	20.29	2024-12-02 01:54:29	19.90
2024-12-02 01:55:25	19.86	2024-12-02 01:55:06	19.40	2024-12-02 01:56:07	20.30	2024-12-02 01:55:29	19.90
2024-12-02 01:56:25	19.86	2024-12-02 01:56:06	19.40	2024-12-02 01:57:07	20.32	2024-12-02 01:56:29	19.91
2024-12-02 01:57:25	19.86	2024-12-02 01:57:06	19.39	2024-12-02 01:58:07	20.33	2024-12-02 01:57:29	19.92
2024-12-02 01:58:26	19.86	2024-12-02 01:58:07	19.40	2024-12-02 01:59:08	20.35	2024-12-02 01:58:29	19.93
2024-12-02 01:59:26	19.86	2024-12-02 01:59:07	19.38	2024-12-02 02:00:08	20.36	2024-12-02 01:59:29	19.93
2024-12-02 02:00:26	19.86	2024-12-02 02:00:07	19.39	2024-12-02 02:01:08	20.37	2024-12-02 02:00:29	19.94
2024-12-02 02:01:26	19.86	2024-12-02 02:01:07	19.40	2024-12-02 02:02:08	20.38	2024-12-02 02:01:30	19.95
2024-12-02 02:02:26	19.87	2024-12-02 02:02:07	19.41	2024-12-02 02:03:08	20.38	2024-12-02 02:02:30	19.94
2024-12-02 02:03:27	19.86	2024-12-02 02:03:07	19.42	2024-12-02 02:04:08	20.39	2024-12-02 02:03:30	19.96
2024-12-02 02:55:31	20.05	2024-12-02 02:55:13	19.49	2024-12-02 02:54:13	20.54	2024-12-02 02:55:34	20.35
2024-12-02 02:56:31	20.07	2024-12-02 02:56:13	19.50	2024-12-02 02:55:13	20.54	2024-12-02 02:56:34	20.35
2024-12-02 02:57:31	20.11	2024-12-02 02:57:13	19.51	2024-12-02 02:56:13	20.54	2024-12-02 02:57:34	20.36
2024-12-02 02:58:31	20.13	2024-12-02 02:58:13	19.51	2024-12-02 02:57:13	20.54	2024-12-02 02:58:34	20.37
2024-12-02 02:59:31	20.16	2024-12-02 02:59:14	19.52	2024-12-02 02:58:13	20.54	2024-12-02 02:59:34	20.37
2024-12-02 03:00:32	20.19	2024-12-02 03:00:14	19.52	2024-12-02 02:59:14	20.55	2024-12-02 03:00:34	20.38
2024-12-02 03:01:32	20.22	2024-12-02 03:01:14	19.54	2024-12-02 03:00:14	20.56	2024-12-02 03:01:34	20.39
2024-12-02 03:02:32	20.23	2024-12-02 03:02:14	19.54	2024-12-02 03:01:14	20.55	2024-12-02 03:02:34	20.39
2024-12-02 03:03:32	20.25	2024-12-02 03:03:14	19.55	2024-12-02 03:02:14	20.57	2024-12-02 03:03:35	20.39
2024-12-02 03:04:32	20.26	2024-12-02 03:04:14	19.55	2024-12-02 03:03:14	20.58	2024-12-02 03:04:35	20.40
2024-12-02 03:54:36	20.38	2024-12-02 03:54:19	19.62	2024-12-02 03:54:18	20.81	2024-12-02 03:54:38	20.40
2024-12-02 03:55:36	20.40	2024-12-02 03:55:19	19.58	2024-12-02 03:55:18	20.80	2024-12-02 03:55:38	20.38
2024-12-02 03:56:36	20.40	2024-12-02 03:56:19	19.60	2024-12-02 03:56:18	20.81	2024-12-02 03:56:38	20.38
2024-12-02 03:57:36	20.40	2024-12-02 03:57:19	19.61	2024-12-02 03:57:18	20.81	2024-12-02 03:57:38	20.39
2024-12-02 03:58:36	20.40	2024-12-02 03:58:19	19.61	2024-12-02 03:58:18	20.81	2024-12-02 03:58:39	20.39
2024-12-02 03:59:36	20.40	2024-12-02 03:59:19	19.62	2024-12-02 03:59:18	20.81	2024-12-02 03:59:39	20.38
2024-12-02 04:00:36	20.40	2024-12-02 04:00:19	19.62	2024-12-02 04:00:18	20.81	2024-12-02 04:00:39	20.39
2024-12-02 04:01:36	20.39	2024-12-02 04:01:19	19.62	2024-12-02 04:01:19	20.80	2024-12-02 04:01:39	20.34
2024-12-02 04:02:36	20.39	2024-12-02 04:02:19	19.62	2024-12-02 04:02:19	20.81	2024-12-02 04:02:39	20.31
2024-12-02 04:03:36	20.39	2024-12-02 04:03:19	19.62	2024-12-02 04:03:19	20.81	2024-12-02 04:03:39	20.33

Table A.5.: Data collected from TESS photometers in Eisenstadt, with timestamps depicting when measurements were taken during the night of April 2nd 2025.

02.04.2025							
941		943		944		1120	
2025-04-02 00:54:54	19.44	2025-04-02 00:54:06	18.73	2025-04-02 00:55:19	19.49	2025-04-02 00:55:06	18.93
2025-04-02 00:55:55	19.42	2025-04-02 00:55:06	18.70	2025-04-02 00:56:19	19.49	2025-04-02 00:56:06	18.87
2025-04-02 00:56:55	19.35	2025-04-02 00:56:06	18.64	2025-04-02 00:57:20	19.47	2025-04-02 00:57:07	18.87
2025-04-02 00:57:55	19.23	2025-04-02 00:57:06	18.57	2025-04-02 00:58:20	19.44	2025-04-02 00:58:07	18.93
2025-04-02 00:58:55	19.11	2025-04-02 00:58:07	18.53	2025-04-02 00:59:20	19.46	2025-04-02 00:59:07	18.96
2025-04-02 00:59:55	19.04	2025-04-02 00:59:07	18.51	2025-04-02 01:00:20	19.51	2025-04-02 01:00:07	19.00
2025-04-02 01:00:55	19.03	2025-04-02 01:00:07	18.53	2025-04-02 01:01:20	19.57	2025-04-02 01:01:07	19.05
2025-04-02 01:01:55	19.04	2025-04-02 01:01:07	18.59	2025-04-02 01:02:20	19.58	2025-04-02 01:02:07	19.07
2025-04-02 01:02:55	19.10	2025-04-02 01:02:08	18.69	2025-04-02 01:03:20	19.60	2025-04-02 01:03:08	19.11
2025-04-02 01:03:55	19.20	2025-04-02 01:03:08	18.77	2025-04-02 01:04:20	19.62	2025-04-02 01:04:08	19.21
2025-04-02 01:54:02	19.98	2025-04-02 01:55:18	19.27	2025-04-02 01:55:26	20.59	2025-04-02 01:55:23	19.66
2025-04-02 01:55:02	20.01	2025-04-02 01:56:18	19.27	2025-04-02 01:56:26	20.59	2025-04-02 01:56:23	19.68
2025-04-02 01:56:03	20.00	2025-04-02 01:57:18	19.28	2025-04-02 01:57:26	20.59	2025-04-02 01:57:23	19.75
2025-04-02 01:57:03	19.96	2025-04-02 01:58:18	19.28	2025-04-02 01:58:26	20.58	2025-04-02 01:58:23	19.85
2025-04-02 01:58:03	19.92	2025-04-02 01:59:18	19.27	2025-04-02 01:59:26	20.58	2025-04-02 01:59:23	19.92
2025-04-02 01:59:03	19.89	2025-04-02 02:00:18	19.26	2025-04-02 02:00:26	20.58	2025-04-02 02:00:24	19.97
2025-04-02 02:00:03	19.87	2025-04-02 02:01:19	19.25	2025-04-02 02:01:26	20.56	2025-04-02 02:01:24	19.99
2025-04-02 02:01:03	19.81	2025-04-02 02:02:19	19.23	2025-04-02 02:02:26	20.53	2025-04-02 02:02:24	19.98
2025-04-02 02:02:03	19.69	2025-04-02 02:03:19	19.18	2025-04-02 02:03:26	20.50	2025-04-02 02:03:24	19.98
2025-04-02 02:03:03	19.53	2025-04-02 02:04:19	19.14	2025-04-02 02:04:27	20.48	2025-04-02 02:04:24	19.99
2025-04-02 02:55:11	18.54	2025-04-02 02:55:30	19.01	2025-04-02 02:55:33	20.39	2025-04-02 02:55:33	19.89
2025-04-02 02:56:12	18.53	2025-04-02 02:56:30	18.83	2025-04-02 02:56:33	20.32	2025-04-02 02:56:33	19.90
2025-04-02 02:57:12	18.42	2025-04-02 02:57:30	18.62	2025-04-02 02:57:33	20.31	2025-04-02 02:57:33	19.58
2025-04-02 02:58:12	18.34	2025-04-02 02:58:30	18.40	2025-04-02 02:58:33	20.31	2025-04-02 02:58:33	19.03
2025-04-02 02:59:12	18.31	2025-04-02 02:59:30	18.20	2025-04-02 02:59:33	20.27	2025-04-02 02:59:34	18.87
2025-04-02 03:00:13	18.30	2025-04-02 03:00:30	18.09	2025-04-02 03:00:33	20.10	2025-04-02 03:00:34	18.92
2025-04-02 03:01:13	18.21	2025-04-02 03:01:31	18.06	2025-04-02 03:01:33	19.67	2025-04-02 03:01:34	18.79
2025-04-02 03:02:13	18.10	2025-04-02 03:02:31	18.00	2025-04-02 03:02:33	19.39	2025-04-02 03:02:34	18.65
2025-04-02 03:03:13	18.07	2025-04-02 03:03:31	17.83	2025-04-02 03:03:34	19.27	2025-04-02 03:03:34	18.56
2025-04-02 03:04:13	18.03	2025-04-02 03:04:31	17.72	2025-04-02 03:04:34	19.17	2025-04-02 03:04:34	18.45
2025-04-02 03:55:21	18.66	2025-04-02 03:55:44	18.91	2025-04-02 03:55:40	20.56	2025-04-02 03:55:42	19.25
2025-04-02 03:56:22	18.74	2025-04-02 03:56:45	18.87	2025-04-02 03:56:40	20.57	2025-04-02 03:56:42	19.26
2025-04-02 03:57:22	18.83	2025-04-02 03:57:45	18.68	2025-04-02 03:57:40	20.57	2025-04-02 03:57:43	19.35
2025-04-02 03:58:22	18.83	2025-04-02 03:58:45	18.49	2025-04-02 03:58:40	20.58	2025-04-02 03:58:43	19.38
2025-04-02 03:59:22	18.77	2025-04-02 03:59:45	18.41	2025-04-02 03:59:40	20.61	2025-04-02 03:59:43	19.30
2025-04-02 04:00:22	18.72	2025-04-02 04:00:45	18.43	2025-04-02 04:00:40	20.61	2025-04-02 04:00:43	19.24
2025-04-02 04:01:22	18.69	2025-04-02 04:01:45	18.46	2025-04-02 04:01:41	20.60	2025-04-02 04:01:43	19.26
2025-04-02 04:02:23	18.68	2025-04-02 04:02:45	18.47	2025-04-02 04:02:41	20.60	2025-04-02 04:02:43	19.30
2025-04-02 04:03:23	18.73	2025-04-02 04:03:45	18.55	2025-04-02 04:03:41	20.60	2025-04-02 04:03:43	19.34
2025-04-02 04:04:23	18.86	2025-04-02 04:04:45	18.72	2025-04-02 04:04:41	20.60	2025-04-02 04:04:43	19.26

Table A.6.: Data collected from TESS photometers in Eisenstadt, with timestamps depicting when measurements were taken during the night of April 3rd 2025.

03.04.2025							
941		943		944		1120	
2025-04-03 00:56:28	18.11	2025-04-03 00:55:48	18.03	2025-04-03 00:55:31	18.58	2025-04-03 00:55:18	18.04
2025-04-03 00:57:28	18.14	2025-04-03 00:56:49	18.03	2025-04-03 00:56:31	18.55	2025-04-03 00:56:18	18.04
2025-04-03 00:58:28	18.16	2025-04-03 00:57:49	17.96	2025-04-03 00:57:31	18.59	2025-04-03 00:57:18	18.08
2025-04-03 00:59:28	18.11	2025-04-03 00:58:49	17.98	2025-04-03 00:58:31	18.58	2025-04-03 00:58:19	18.14
2025-04-03 01:00:28	18.06	2025-04-03 00:59:49	18.02	2025-04-03 00:59:31	18.56	2025-04-03 00:59:19	18.12
2025-04-03 01:01:28	18.02	2025-04-03 01:00:50	18.01	2025-04-03 01:00:32	18.60	2025-04-03 01:00:19	18.07
2025-04-03 01:02:28	18.08	2025-04-03 01:01:50	17.98	2025-04-03 01:01:32	18.68	2025-04-03 01:01:19	18.07
2025-04-03 01:03:29	18.17	2025-04-03 01:02:50	17.96	2025-04-03 01:02:32	18.71	2025-04-03 01:02:19	18.08
2025-04-03 01:04:29	18.21	2025-04-03 01:03:50	18.01	2025-04-03 01:03:32	18.71	2025-04-03 01:03:20	18.16
2025-04-03 01:05:29	18.21	2025-04-03 01:04:50	18.06	2025-04-03 01:04:32	18.80	2025-04-03 01:04:20	18.24
2025-04-03 01:55:36	18.35	2025-04-03 01:55:04	18.27	2025-04-03 01:55:57	19.05	2025-04-03 01:55:28	18.50
2025-04-03 01:56:36	18.39	2025-04-03 01:56:04	18.41	2025-04-03 01:56:58	19.06	2025-04-03 01:56:28	18.49
2025-04-03 01:57:36	18.48	2025-04-03 01:57:04	18.50	2025-04-03 01:57:58	19.02	2025-04-03 01:57:28	18.51
2025-04-03 01:58:37	18.55	2025-04-03 01:58:04	18.54	2025-04-03 01:58:58	18.99	2025-04-03 01:58:29	18.51
2025-04-03 01:59:37	18.63	2025-04-03 01:59:04	18.54	2025-04-03 01:59:58	18.93	2025-04-03 01:59:29	18.52
2025-04-03 02:00:37	18.60	2025-04-03 02:00:05	18.50	2025-04-03 02:00:58	18.88	2025-04-03 02:00:29	18.60
2025-04-03 02:01:37	18.54	2025-04-03 02:01:05	18.48	2025-04-03 02:01:58	18.91	2025-04-03 02:01:29	18.68
2025-04-03 02:02:37	18.56	2025-04-03 02:02:05	18.43	2025-04-03 02:02:59	18.99	2025-04-03 02:02:29	18.64
2025-04-03 02:03:37	18.59	2025-04-03 02:03:05	18.44	2025-04-03 02:03:59	19.11	2025-04-03 02:03:29	18.58
2025-04-03 02:05:43	18.66	2025-04-03 02:04:05	18.44	2025-04-03 02:04:59	19.10	2025-04-03 02:04:29	18.49
2025-04-03 02:55:50	19.25	2025-04-03 02:55:12	18.71	2025-04-03 02:55:05	19.71	2025-04-03 02:55:36	19.09
2025-04-03 02:56:50	19.29	2025-04-03 02:56:12	18.68	2025-04-03 02:56:05	19.94	2025-04-03 02:56:37	19.13
2025-04-03 02:57:50	19.24	2025-04-03 02:57:12	18.68	2025-04-03 02:57:05	20.06	2025-04-03 02:57:37	19.04
2025-04-03 02:58:50	19.25	2025-04-03 02:58:12	18.64	2025-04-03 02:58:06	20.15	2025-04-03 02:58:37	19.01
2025-04-03 02:59:50	19.28	2025-04-03 02:59:12	18.70	2025-04-03 02:59:06	20.21	2025-04-03 02:59:37	19.04
2025-04-03 03:00:51	19.29	2025-04-03 03:00:12	18.78	2025-04-03 03:00:06	20.23	2025-04-03 03:00:37	19.08
2025-04-03 03:01:51	19.27	2025-04-03 03:01:13	18.85	2025-04-03 03:01:06	20.41	2025-04-03 03:01:37	19.16
2025-04-03 03:02:51	19.31	2025-04-03 03:02:13	18.92	2025-04-03 03:02:06	20.52	2025-04-03 03:02:37	19.21
2025-04-03 03:03:51	19.45	2025-04-03 03:03:13	18.96	2025-04-03 03:03:06	20.51	2025-04-03 03:03:38	19.26
2025-04-03 03:04:51	19.46	2025-04-03 03:04:13	19.08	2025-04-03 03:04:06	20.51	2025-04-03 03:04:38	19.33
2025-04-03 03:55:02	20.24	2025-04-03 03:55:25	19.60	2025-04-03 03:55:37	20.67	2025-04-03 03:55:48	20.29
2025-04-03 03:56:02	20.28	2025-04-03 03:56:25	19.60	2025-04-03 03:56:37	20.61	2025-04-03 03:56:48	20.31
2025-04-03 03:57:03	20.28	2025-04-03 03:57:25	19.59	2025-04-03 03:57:38	20.63	2025-04-03 03:57:48	20.32
2025-04-03 03:58:03	20.30	2025-04-03 03:58:26	19.60	2025-04-03 03:58:38	20.70	2025-04-03 03:58:48	20.33
2025-04-03 03:59:03	20.32	2025-04-03 03:59:26	19.60	2025-04-03 03:59:38	20.70	2025-04-03 03:59:49	20.33
2025-04-03 04:00:03	20.35	2025-04-03 04:00:27	19.60	2025-04-03 04:00:38	20.69	2025-04-03 04:00:49	20.32
2025-04-03 04:01:04	20.36	2025-04-03 04:01:27	19.59	2025-04-03 04:01:39	20.73	2025-04-03 04:01:49	20.32
2025-04-03 04:02:04	20.37	2025-04-03 04:02:27	19.61	2025-04-03 04:02:39	20.74	2025-04-03 04:02:49	20.28
2025-04-03 04:03:04	20.37	2025-04-03 04:03:27	19.61	2025-04-03 04:03:39	20.73	2025-04-03 04:03:50	20.27
2025-04-03 04:04:04	20.37	2025-04-03 04:04:27	19.61	2025-04-03 04:04:39	20.73	2025-04-03 04:04:50	20.27

Table A.7.: Averages of 10 data values in [mag/arcsec^2] from the 29th of November 2024.

	941 - west	943 - center	944 - east	1120 - south
1 a.m.	19.76	19.39	20.31	19.65
2 a.m.	18.98	18.75	19.47	18.75
3 a.m.	19.14	18.77	19.26	19.03
4 a.m.	19.50	19.31	19.85	20.14

Table A.8.: Averages of 10 data values in [mag/arcsec^2] from the 30th of November 2024.

	941 - west	943 - center	944 - east	1120 - south
1 a.m.	19.65	19.42	20.72	20.05
2 a.m.	20.46	19.69	20.86	20.23
3 a.m.	20.42	19.57	20.58	19.06
4 a.m.	20.24	19.02	20.00	18.08

Table A.9.: Averages of 10 data values in [mag/arcsec^2] from the 1st of December 2024.

	941 - west	943 - center	944 - east	1120 - south
1 a.m.	20.29	19.53	20.62	19.96
2 a.m.	20.30	19.51	20.59	19.95
3 a.m.	20.30	19.52	20.63	19.96
4 a.m.	20.25	19.47	20.56	19.92

Table A.10.: Averages of 10 data values in [mag/arcsec^2] from the 2nd of December 2024.

	941 - west	943 - center	944 - east	1120 - south
1 a.m.	20.34	19.60	20.75	20.36
2 a.m.	19.86	19.40	20.35	19.93
3 a.m.	20.17	19.52	20.55	20.38
4 a.m.	20.40	19.61	20.81	20.37

Table A.11.: Averages of 10 data values in [mag/arcsec^2] from the 2nd of April 2025.

	941 - west	943 - center	944 - east	1120 - south
1 a.m.	19.20	18.63	19.52	19.00
2 a.m.	19.87	19.24	20.56	19.88
3 a.m.	18.29	18.28	19.92	19.06
4 a.m.	18.75	18.60	20.59	19.29

Table A.12.: Averages of 10 data values in [mag/arcsec^2] from the 3rd of April 2025.

	941 - west	943 - center	944 - east	1120 - south
1 a.m.	18.13	18.00	18.64	18.10
2 a.m.	18.54	18.46	19.00	18.55
3 a.m.	19.31	18.80	20.23	19.14
4 a.m.	20.32	19.60	20.69	20.30